2009

Vibrational And Mechanical Properties Of 10 Mol % Sc2o3-1 Mol % Ceo2- Zro2 Electrolyte Ceramics For Solid Oxide Fuel Cells

Svetlana Lukich
University of Central Florida

VIBRATIONAL AND MECHANICAL PROPERTIES OF 10 MOL % Sc_2O_3-1 MOL % CeO_2- ZrO_2 ELECTROLYTE CERAMICS FOR SOLID OXIDE FUEL CELLS

by

SVETLANA LUKICH
B.S. University of Central Florida, 2007

A thesis submitted in partial fulfillment of the requirements
for the degree of Master of Science
in Department of Mechanical, Materials and Aerospace Engineering
in the College of Engineering and Computer science
at the University of Central Florida
Orlando, Florida

Fall Term
2009

ABSTRACT

Solid Oxide Fuel Cells (SOFCs) are emerging as a potential breakthrough energy conversion technology for clean and efficient production of electricity and heat from hydrogen and hydro-carbon fuels. $Sc_{0.1}Ce_{0.01}ZrO_2$ electrolytes for Solid Oxide Fuel Cells are very promising materials because their high ionic conductivity in the intermediate temperature range 700°C-800°C.

The vibration response of cubic and rhombohedral (β) 10 mol%Sc_2O_3 - 1 mol%CeO_2 - ZrO_2 ($Sc_{0.1}Ce_{0.01}ZrO_2$) both at room and high-temperatures is reported. The in-situ heating experiments and ex-situ indentation experiments were performed to characterize the vibrational behavior of these important materials. A temperature and stress-assisted phase transition from cubic to rhombohedral phase was detected during in-situ Raman spectroscopy experiments. While heating and indentation experiments performed separately did not cause the transition of the cubic phase into the rhombohedral structure under the performed experimental conditions and only broadened or strained peaks of the cubic phase could be detected, the heating of the indented (strained) surface leaded to the formation of the rhombohedral $Sc_{0.1}Ce_{0.01}ZrO_2$. Both temperature range and strained zone were estimated by in situ heating and 2D mapping, where a formation of rhombohedral or retention of cubic phase has been promoted.

The mechanical properties, such as Young's modulus, Vickers hardness, indentation fracture resistance, room and high temperature four point bending strength and SEVNB fracture toughness along with the stress – strain deformation behavior in compression, of 10 mol% Sc_2O_3

– 1 mol % CeO_2 - ZrO_2 ($ScCeZrO_2$) ceramics have been studied. The chosen composition of the $ScCeZrO_2$ has very high ionic conductivity and, therefore, is very promising oxygen ion conducting electrolyte for the intermediate temperature Solid Oxide Fuel Cells. Therefore, its mechanical behavior is of importance and is presented in this study.

To my parents, my brother and sister

To whom I am forever grateful

For their unconditional love and encouragement

ACKNOWLEGMENTS

I would like to thank my advisor Professor Dr. Nina Orlovskaya of University of Central Florida, USA, for her guidance and support, for her time and effort to help me learn and succeed. Performing research in electrolyte materials for Solid Oxide Fuel Cells has been a good experience for me allowing me to gain a significant knowledge and invaluable skills. Dr. Orlovskaya has provided an opportunity and appreciation for learning that I will always carry with me.

Thanks to Dr. Jayanta Kapat, Dr. Linan An, Dr. Xinyu Huang, and Dr. Marcel Ilie for serving as my committee members.

Special thanks to the staff of University of Central Florida, Department of Mechanical, Materials and Aerospace Engineering, Material Characterization Facility, AMPAC, Kirk Scammon, MCF Research Engineer, Mikhail Klimov, MCF Research Engineer, Karen Glidewell, Faculty Coordinator, to Dr. Ghatu Subhash, University of Florida, Department of Mechanical and Aerospace Engineering, to my friends and colleagues, Cassandra Carpenter, Prabhakar Mohan, and everyone who shared their expertise and opinions, and gave suggestions and advice. Those discussions and suggestions helped me to better understand behavior of material, so I would succeed with my work as a researcher and achieve enhanced results.

Above all, I am incredibly grateful to my family for all their support and their unconditional love.

This work was supported by the NSF DMR project number 0502765. The author would also like to thank Mr. R. Bächtold for his help in performing the mechanical tests at EMPA, Swiss Federal

Laboratories for Materials Testing and Research, Laboratory for High Performance Ceramics, Ueberlandstr. 129, 8600 Duebendorf, Switzerland.

TABLE OF CONTENTS

LIST OF FIGURES ix

LIST OF TABLES xii

LIST OF EQUATIONS xiii

CHAPTER 1: INTRODUCTION 1

1.1 Introduction to Fuel Cells 1
1.2 Essentials of Fuel Cells 2
1.3 Types of Fuel Cells 5
1.4 Basic Mechanism of SOFCs 8
1.5 SOFCs design 11
1.6 Electrolyte for Solid Oxide Fuel Cells 14
1.7 Zirconia (ZrO_2) and its dopents 16
1.8 Goals of Work 21

CHAPTER 2: LITERATURE REVIEW 23

2.1 Material overview 23
2.2 Previous study review of DKKK and Praxair powders (XRD, sintering and phase stability) 24
2.3 DKKK vs. Praxair 32

CHAPTER 3: METHODOLOGY 34

3.1 Introduction to vibrational properties of $Sc_{0.1}Ce_{0.01}ZrO_2$ ceramics 34
3.2 Introduction to mechanical properties of $Sc_{0.1}Ce_{0.01}ZrO_2$ ceramics 36
3.3 Experimental Procedure 38

CHAPTER 4: RESULTS AND DISCUSSIONS 48

4.1 Raman Spectroscopy Analysis and vibrational properties of $Sc_{0.1}Ce_{0.01}ZrO_2$ 48
4.2 Mechanical properties of $Sc_{0.1}Ce_{0.01}ZrO_2$ ceramics 70
4.2.1. Stability, lattice parameters, and densities of the cubic and rhombohedral $Sc_{0.1}Ce_{0.01}ZrO_2$ 70
4.2.2 Young's modulus of cubic and rhombohedral $Sc_{0.1}Ce_{0.01}ZrO_2$ 71
4.2.3. Hardness and indentation fracture resistance 72
4.2.4. Strength and fracture toughness 75

CHAPTER 5: CONCLUSION AND FUTURE WORK 82

5.1 Conclusion 82
5.2 Future work 85

APENDIX: SHORT BIOGRAPHY 86

LIST OF REFERENCES 87

LIST OF FIGURES

Figure 1: Typical fuel cell chart 2
Figure 2: Schematic of an individual fuel cell 4
Figure 3: Schematic of a solid oxide fuel cell (SOFC) element with anode, cathode and electrolyte 10
Figure 4: Typical solid oxide fuel cell planar design 12
Figure 5: Tubular solid oxide fuel cell model 13
Figure 6: Monolith SOFC design; cross section 13
Figure 7: Total conductivity vs. temperature for fluorite base structure materials with oxygen ion conductivity 15
Figure 8: ZrO2 cubic fluorite structure with oxide ions occupying all tetrahedral sites 17
Figure 9: Phase diagram for the ZrO2 – Y2O3 system 18
Figure 10: Conductivity vs. concentration for ZrO2 – based electrolytes 19
Figure 11: Phase diagram of Sc2O3 – ZrO2 system 20
Figure 12: SEM images of A) Praxair and B) DKKK powders 25
Figure 13: XRD patterns of A) Praxair and B) DKKK powders 27
Figure 14: Sintering behavior of DKKK and Praxair powders; A) Material Shrinkage vs. sintering temperature; B) Porosity level vs. sintering temperature 28
Figure 15: Grain size vs. sintering temperature of DKKK and Praxair powders 29
Figure 16: Microsrtucture of Praxair powders sintered at A) 1400^{o}C, B) 1500^{o}C, C) 1600^{o}C 29
Figure 17: Microsrtucture of DKKK powders sintered at A) 1300^{o}C, B) 1500^{o}C, C) 1600^{o}C 30
Figure 18: Multiphase investigation of DKKK powders at different temperatures 32
Figure 19: Flow chart of experimental procedure 39
Figure 20: Renishaw InVia Raman spectrometer 40
Figure 21: Sc0.1Ce0.01ZrO2 polished sample bars placed in DKKK sintering powder 42
Figure 22: High temperature furnace used in sintering of the Sc0.1Ce0.01ZrO2 bars 42
Figure 23: Vickers indenter impression 43
Figure.24: The spectral range of cubic and rhombohedral $Sc_{0.1}Ce_{0.01}ZrO_2$ electrolyte ceramics collected by 532 nm solid Si and 785 nm NIR lasers. 49
Figure 25: Vibrational spectra of cubic and rhombohedral (β) $Sc_{0.1}Ce_{0.01}ZrO_2$ ceramics; A, C – non-deformed polished surface, B, D – center of Vickers impression 51

Figure 26: High temperature spectra of cubic of Sc0.1Ce0.01ZrO2 ceramics heated up to 1000°C with 100°C step size and 10°C/min heating rate. A dwell time of 5 minutes was used at each temperature before spectrum's collection..... 56

Figure 27: A) Typical spectra of cubic and rhombohedral (β) $Sc_{0.1}Ce_{0.01}ZrO_2$, B) The deconvoluted peaks of cubic and rhombohedral (β) $Sc_{0.1}Ce_{0.01}ZrO_2$. 57

Figure 28: A, B) Confocal images of cubic and rhombohedral (β) $Sc_{0.1}Ce_{0.01}ZrO_2$, ceramics used to determine hardness and indentation fracture toughness 58

Figure 29: C, D) Confocal optical micrographs of impressions made by a Vickers indenter in C) cubic of $Sc_{0.1}Ce_{0.01}ZrO_2$ and D) rhombohedral (β) $Sc_{0.1}Ce_{0.01}ZrO_2$ ceramics used to determine hardness and indentation fracture toughness, as well as used for mapping experiments. 59

Figure 30: Spectra of cubic (A) and rhombohedral (B) Sc0.1Ce0.01ZrO2 during heating and cooling up to 400oC. 61

Figure 31: Position of the peaks of cubic (A) and rhombohedral (β) phases (B) vs. temperature upon heating experiments; ▲ - Polished surface, ◆ - Center of Vickers impression, □ - Stress field. 63

Figure 32: 2D maps of the peak positions for cubic phase of $Sc_{0.1}Ce_{0.01}ZrO_2$. 64

Figure 33: 2D maps of the peak positions for rhombohedral phase of $Sc_{0.1}Ce_{0.01}ZrO_2$. 65

Figure 34: 3D maps of Vickers impression and deformation zone of cubic (A) 66

Figure 35: A) Confocal micrograph of Vickers impression in cubic $Sc_{0.1}Ce_{0.01}ZrO_2$ phase after 400°C heating/cooling. The Vickers impression was placed before heating/cooling. B) 2D maps of 1434 – 1474 cm^{-1} peak position of the selected area with the Vickers impression and deformation zones corresponding to the micrograph from Fig. 32; C) Typical spectra corresponding to cubic, cubic + rhombohedral (β), and pure rhombohedral (β)phases from three different locations of the map presented in 33; D) 1D map of the 1430 – 1480 cm^{-1} peak position collected along x-axis at the intersection with 0 of *y*-axis along AB line..... 69

Figure 36: Young's modulus vs. temperature of (A) the cubic phase sintered from Praxair (▬■▬) and DKKK (▬◆▬) powders, and (B) the rhombohedral DKKK (▬●▬) $Sc_{0.1}Ce_{0.01}ZrO_2$ ceramics. 73

Figure 37: Hardness (▬◆▬) and indentation fracture resistance (▬●▬) of cubic (A) and rhombohedral (B) $Sc_{0.1}Ce_{0.01}ZrO_2$. 74

Figure 38: A pore as a fracture origin of DKKK $Sc_{0.1}Ce_{0.01}ZrO_2$ ceramics tested at RT and 800°C 75

Figure 39: The polished surface of Praxair Sc0.1Ce0.01ZrO2 ceramics sintered at 1600oC 76

Figure 40: Fracture surface of DKKK $Sc_{0.1}Ce_{0.01}ZrO_2$ ceramics after K_{Ic} measurement at RT (A) and 1000°C (B). 78

Figure 41: Fracture surface of Praxair $Sc_{0.1}Ce_{0.01}ZrO_2$ ceramics after K_{Ic} measurement at RT (A) and 1000°C (B). 80

Figure 42: 16 (A) Fracture origin; (B) fracture surface after RT test; and (C) fracture surface after 400oC test of the of rhombohedral $Sc_{0.1}Ce_{0.01}ZrO_2$ ceramics 81

LIST OF TABLES

Table 1: Major differences of the fuel cell types 7
Table 2: Properties of $ScCeZrO_2$ powders 24
Table 3: Grain size vs. sintering temperature for DKKK and Praxair powders 30
Table 4: Phase transition in dependence of sintering temperature for DKKK ScCeZrO2 ceramics 31

LIST OF EQUATIONS

Equation 1: Chemical reaction at cathode 4
Equation 2: Chemical reaction at anode 4
Equation 3: Overall chemical reaction..... 4
Equation 4: Vickers hardness..... 43
Equation 5: Fracture toughness..... 44

CHAPTER 1:
INTRODUCTION

This chapter gives basic information on fuel cells. In this introductory part the main focus has been put on intermediate temperature Solid Oxide Fuel Cells (SOFC). Existing design solutions and materials in use for SOFCs are discussed. Especially the importance of electrolytes for intermediate temperature solid oxide fuel cells and phase transformation which takes place due to change in temperature are mentioned in this chapter. The goal of this research work is given at the end of the chapter.

1.1 Introduction to Fuel Cells

Advanced ceramics have gained attention over the last few decades for their use in energy efficient systems such as Solid Oxide Fuel Cells (SOFCs). SOFCs are of great interest for the next generation energy exchange systems. For one thing SOFCs have superior energy efficiency when compared to existing energy systems, they require low maintenance, they are silent and environmentally safe. [1]. Materials designed to be used in these systems have been described with respect to their electrochemical and thermomechanical properties. The material properties of SOFCs usually enclose ionic conductivity, phase stability, electrical conductivity and a thermal expansion coefficient.

A typical fuel cell is an electrochemical conversion device developed in order to substitute combustion energy and battery systems. Such a device converts chemical energy in fuels directly into electrical energy avoiding the steps of producing mechanical work and heat, figure 1 [2].

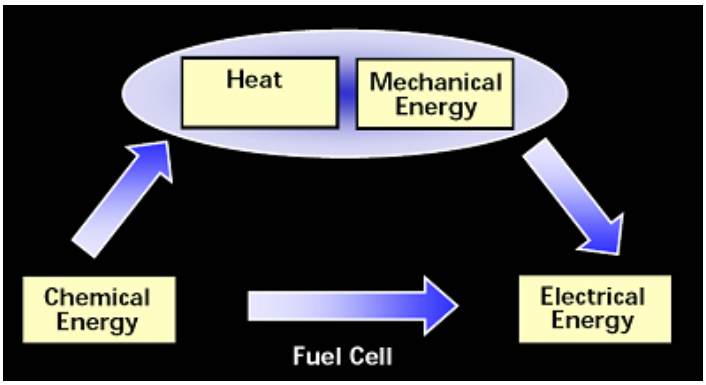

Figure 1: Typical fuel cell chart

For this reason, fuel cells are not thermodynamically limited. Besides this, fuel cells generate power with minimal toxic waste since there is no combustion present. However, the reactant and oxidant in fuel cells need to be continuously refilled to allow permanent process.

Even though fuel cells could work with a variety of fuels and oxidants, the most common use are hydrogen as a reactant, and ambient air as the oxidant.

The efficiency of the fuel cell is dependent on the kinetics and driving forces of electrochemical reactions. In such a system an electrolyte is very important. For one thing, decrease in thickness of the electrolyte has great advantages. To improve the internal resistance of the electrolyte its thickness needs to be reduced. This would bring the fuel cell to a position that can operate at a lower temperature [3].

1.2 Essentials of Fuel Cells

A fuel cell is a device that produces electricity converting the energy released from a chemical reaction directly into electric power. It consists of two electrodes surrounding an electrolyte. Such a system has an external fuel source, usually hydrogen gas and it will generate electricity as long as fuel is supplied. Hydrogen passes over one electrode and oxygen over the other generating electricity, heat and water.

In such a device a chemical reaction takes place at the border between an electron conductor (electrode) and an ionic conductor (electrolyte) engaging electrons. The fuel cell operates as a type of continuously refilled battery providing electrical energy. This energy is obtained from fuel delivered on a negatively charged electrode (anode) side and an oxidant on a positively charged electrode (cathode) side, which react with an electrolyte. At the contact surface (interface) between the anode and the electrolyte the electrons and protons of the reactant (H_2) get separated. The electrons are then forced to move forward trough the circuit, and are converted to electrical energy. On the other side of the fuel cell, oxygen enters from the air the cathode and joins with returning electrons from the electrical circuit and hydrogen ions (H^+) that have traveled through the electrolyte from the anode. In some fuel cell types the oxygen receives electrons and then oxygen ions (O^{2-}) join with hydrogen ions at the anode as they pass through the electrolyte. In each case, hydrogen and oxygen together form water, which is drained out of the fuel cell. In a fuel cell system the electrolyte material is very important. It must allow only the appropriate ions to pass between the anode and cathode. Otherwise, if free electrons or other elements could travel trough the electrolyte, the chemical reaction would be disturbed which would lead to failure of the fuel cell.

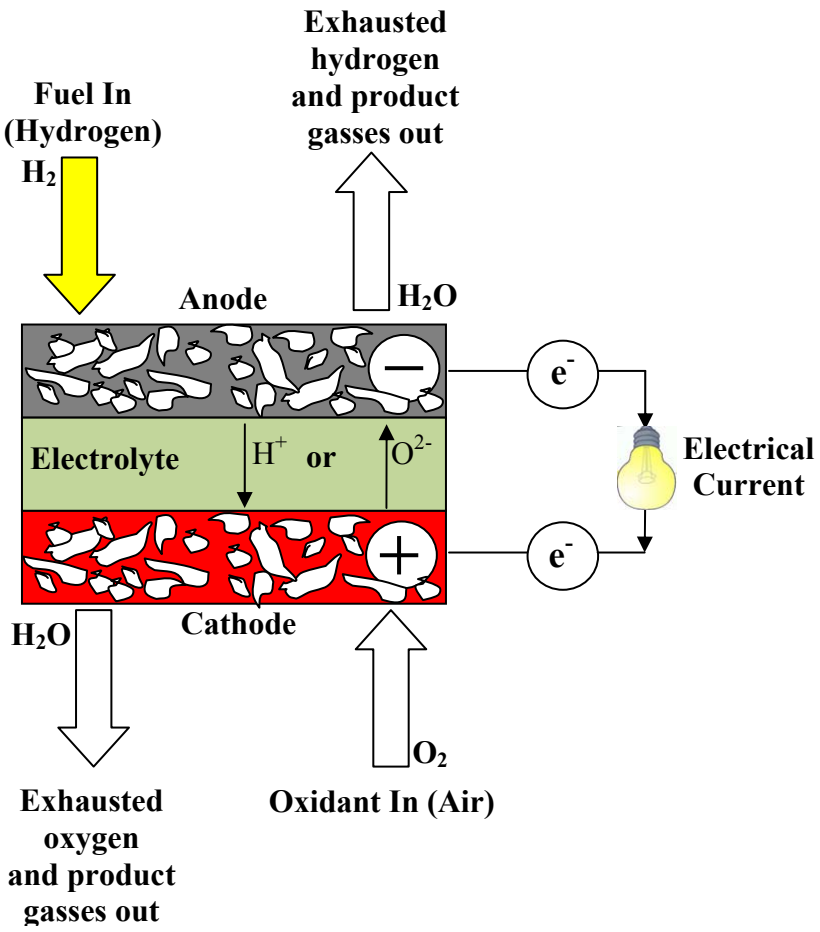

Figure 2: Schematic of an individual fuel cell

Typical chemical reactions of each of the fuel cell components are shown below [4]:

Equation 1: Chemical reaction at cathode

$$\tfrac{1}{2}\, O_2 + 2e^- \rightarrow O^{2-} \qquad (1)$$

Equation 2: Chemical reaction at anode

$$H_2 + O^{2-} \rightarrow H_2O + 2e^- \qquad (2)$$

Equation 3: Overall chemical reaction

$$\tfrac{1}{2}\, O_2 + H_2 \rightarrow H_2O \qquad (3)$$

1.3 Types of Fuel Cells

The fuel cells enclose either solid or liquid electrolytes sandwiched between an anode and a cathode. Fuel cells are classified by their electrolyte material. The operating temperature and the fuel used in the fuel cell system depend on characteristics of the electrolyte material. Fuels used in fuel cell systems include both gaseous fuels (natural gas, propane, hydrogen, and biogases), and liquid fuels such as ethanol and methanol. Today we recognize five major types of fuel cells, distinguished from one another by the source of their electrolyte [5]:

- Phosphoric acid fuel cell (PAFC)
- Polymer electrolyte membrane fuel cell (PEMFC)
- Alkaline fuel cell (AFC)
- Molten carbonate fuel cell (MCFC)
- Solid oxide fuel cell (SOFC).

All five fuel cell types are based upon the same electrochemical properties; they operate at different temperature, include different materials, and vary in their fuel tolerances and performance characteristics [5].

The operating temperature and life of a fuel cell characterize the physicochemical and thermodynamical properties of materials used in the fuel cell design (anode, cathode, electrolyte, interconnect). In low-temperature fuel cells, all fuel must be converted to hydrogen prior to entering the fuel cell. In high-temperature fuel cells, CO and CH_4 can be internally converted to hydrogen or directly oxidized electrochemically [6]. Table 1 lists some certain characteristics of each type of fuel cell [6].

In general, high-temperature fuel cells have higher efficiency and are less sensitive to fuel composition than low-temperature fuel cells.

Some advantages of Solid Oxide Fuel Cells with respect to other fuel cells are:

- Due to their high operating temperature and when pressurized SOFCs have potential to be used in combination with other systems, such as a gas turbine. This combination would provide around 60% efficiency. These SOFC-gas turbine systems are comparable in respect to price to other power generation systems due to their high efficiency, high availability, and low maintenance costs [7].
- SOFC electrolyte is solid and the cell can be made in variety of shapes, such as monolithic, planer, or tubular. Since the cells are made from common ceramic materials they don't experience any corrosion problems. For that reason the SOFCs are highly reliable generation systems with minimum maintenance.
- Materials used in SOFCs are modest in cost. They don't require expensive catalysts and they can operate on natural gas or methane.
- SOFCs operate at elevated temperatures. Also, they are flexible in choice of fuel and tolerant to CO.

Table 1: Major differences of the fuel cell types

	PEFC	AFC	PAFC	MCFC	SOFC
Electrolyte	Hydrated Polymeric Ion Exchange	Mobilized or Immobilized Potassium Hydroxide in Asbestos Matrix	Immobilized Liquid Phosphoric Acid in SiC	Immobilized Liquid Molten Carbon in $LiAlO_2$	Perovskites (Ceramics)
Electrodes	Carbon	Transition Metals	Carbon	Electrode Material	Electrode Material
Catalyst	Platinum	Platinum	Platinum	Electrode Material	Electrode Material
Interconnect	Carbon or Metal	Metal	Graphite	Stainless Steel or Nickel	Nickel, Ceramics, or Steel
Operating Temperature	$40^oC – 80^oC$	$65^oC – 220^oC$	205^oC	650^oC	600^oC-1000^oC
Charge Carrier	H^+	OH^-	H^+	$CO3^=$	$O^=$
External Reform for Hydrocarbon Fuels	Yes	Yes	Yes	No, for some fuels	No, for some fuels and cell designs
External Shift Conversion of CO to Hydrogen	Yes, plus purification to remove trace CO	Yes, plus purification to remove CO and CO_2	Yes	No	No
Prime Cell Components	Carbon-based	Carbon-based	Graphite-based	Stainless-based	Ceramics
Product Water Management	Evaporative	Evaporative	Evaporative	Gaseous Product	Gaseous Product
Product Heat Management	Process Gas + Liquid Cooling Medium	Process Gas + Electrolyte Circulation	Process Gas + Liquid Cooling Medium or Steam Generation	Internal Reforming + Process Gas	Internal Reforming + Process Gas

1.4 Basic Mechanism of SOFCs

Solid Oxide Fuel Cells (SOFCs) are energy conversion systems that produce electricity by electrochemical reaction from fuel with an oxidant [8]. SOFCs operate at high temperature and use ceramics as functional elements of the cell. Basic components of SOFC are:

- Anode (fuel electrode)
- Electrolyte
- Cathode (air electrode)
- Interconnect

Materials selected for cell components need to have appropriate electrical conductivity properties required for each cell component. All cell components need to have similar thermal expansion coefficients and chemical stability during cell operation.

Some requirements the fuel electrode (anode) in the solid oxide fuel cell systems need to meet are:

- Must have high electronic conductivity.
- Must reach thermodynamic stability of the chemical system during the operation of the fuel cell.
- Must be porous to allow transport of the fuel oxidation products away from the electrode/electrolyte interface where this reaction takes place.
- Must have minimum reactivity with the electrolyte and interconnect in case of stacking modeling [7].

Typical material of the anode is Nickel-Yttria stabilized zirconia [9]. The yttria stabilized zirconia (YSZ) is placed around the nickel particles which prevent sintering of nickel (nickel can sinter at the cell operative temperature and reduce the electrode porosity), brings the electrode thermal expansion coefficient closer to the thermal expansion coefficient of the electrolyte, and provides better bonding between anode and the electrolyte.

The cathode requirements are similar to those of anode. It has to be porous to tolerate oxygen molecules to reach the electrode/electrolyte interface. The most common material used for cathode is based on lanthanum manganite ($LaMnO_3$) which is perovskite oxide (ABO_3) [9].

Since a single solid oxide fuel cell produces approximately 1 volt, it needs to be connected to other cells in order to establish the desired voltage needed for an application forming a stack. The connector among the cells is known as the interconnect. An interconnect physically separates the cells and connects them electrically. Some requirements for the interconnect are [10]:

- Has to be fully dense to prevent mixing of fuel and oxidant gases.
- Has to allow supply of fuel to the anode and the oxidant to the cathode.
- Has to remove the reaction products to ensure electrochemical reaction.
- Has to work in the environment of an anode and the environment of a cathode.

The most commonly used material for the interconnect is lanthanum chromate ($LaCrO_3$) [10].

A schematic of SOFC is shown in Fig. 3 [11]. A porous anode and cathode in SOFCs are separated by a solid waterproof electrolyte, which during operation of the cell conduct oxygen ions from the cathode to the anode where they react with the fuel. An electric charge, which is provoked by the traveling of the ions, may be collected and induced away from the cell. In the SOFC the electrolyte conducts O^{2-} ions. The movement of O^{2-} ions is caused by the oxygen

chemical potential gradient between the anode and cathode [11]. Usually, at the cathode side where air is used, the partial pressure of oxygen is higher. At the anode, where oxygen ions are used to produce water, the partial pressure is low.

Solid oxide materials that demonstrate oxygen ion conductivity are mostly used as electrolytes for solid oxide fuel cells (SOFCs) [10]. The operating temperature of a SOFC is between 500°C and 1000°C since the conduction of the oxygen ions in a solid electrolyte is a thermal process.

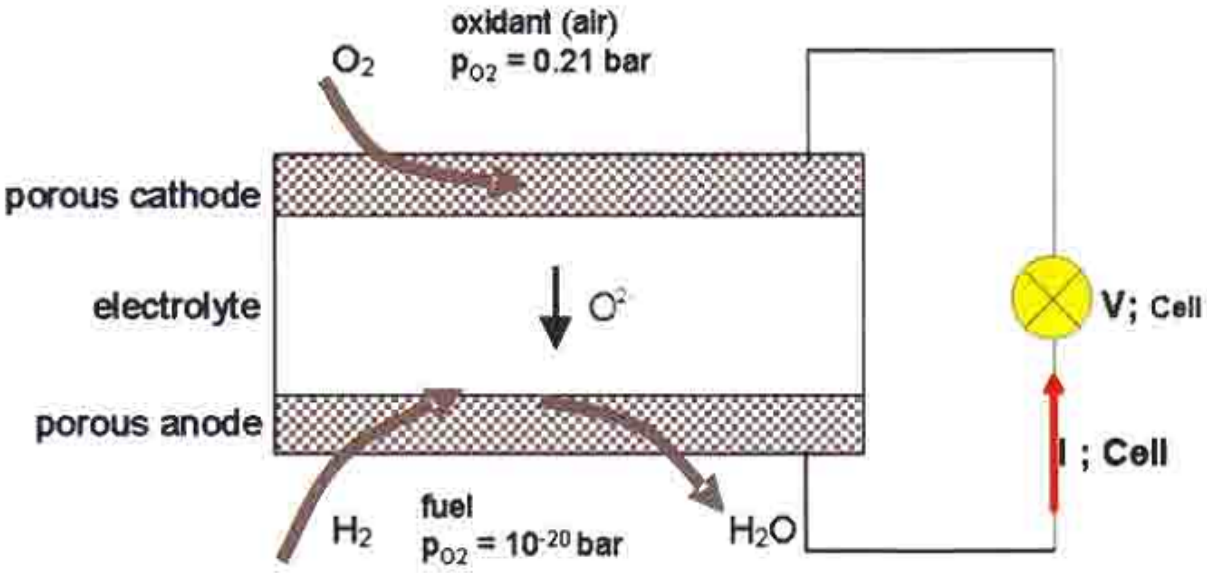

Figure 3: Schematic of a solid oxide fuel cell (SOFC) element with anode, cathode and electrolyte

Depending on the working temperature there are three groups of the SOFCs [2]:

- High temperature SOFCs; temperature range 900°C – 1000°C.
- Intermediate temperature SOFCs; temperature range 600°C-800°C.
- Low temperature SOFCs; temperature range 500°C-600°C.

In the case of high operating temperature SOFCs a long warm-up time is required. The reason for such a long preparation is to avoid damage due to differences in thermal expansion properties

of materials used in the design of the fuel cell. Furthermore, no current production takes place in SOFCs until a critical temperature is reached in the electrolyte [13].

Intermediate temperature SOFCs, by reduction in operating temperature, would allow quick startup and application of inexpensive metallic components for cell interconnects. Involvement of metallic components in the cells design can result in lower cost of the manufacturing method for SOFC systems.

1.5 SOFCs design

Sold oxide fuel cells have variety of designs comparing to other fuel cells. The planar, tubular and monolithic are different configurations of such systems. The most common SOFC stack is the planar design. In this design configuration, individual cell units are connected with interconnects in order to reach desired voltage. In a planar arrangement system, the interconnector becomes a separator plate which needs to provide an electrical series connection between neighboring cells, and needs to provide a gas barrier that separates the fuel and oxidant of neighboring cells [6]. Planar design is electrically simple, Fig. 4.

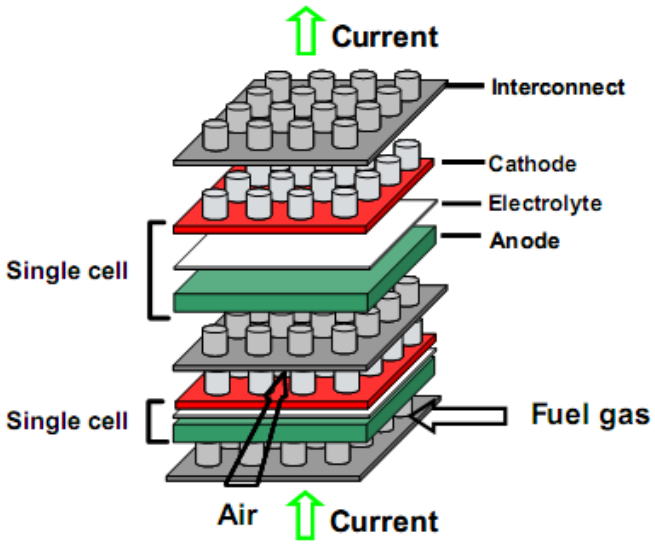

Figure 4: Typical solid oxide fuel cell planar design

This design uses simple cell interconnectors and is assembled without difficulty, but it allows gas to leak at high temperature. To solve this problem, high temperature gas seals may be used. However, they are expensive and this would lead to increase in price of the system [14].

Another common design for SOFCs is the tubular design. One of the advantages of this design configuration when compared to the planar design is that the tubular design eliminates the need for a gas seal. However, these designs suffer an increase in Ohmic loss since the electrons travel along a much longer pathway than other cells [6]. To minimize the length of electron travel path, a series of connected cells are developed, and the cell range can be connected either in series or parallel. The tubular design of the solid oxide fuel cell is presented in Fig. 5 [15].

The monolithic design is less developed. A schematic of this design is given in Fig. 6 [16]. The advantage of monolithic design is high power density which is result of the high active area and the short ionic pathways through the electrodes, electrolyte and interconnects [13]. The disadvantage of this design for SOFCs is a very complex manufacturing process.

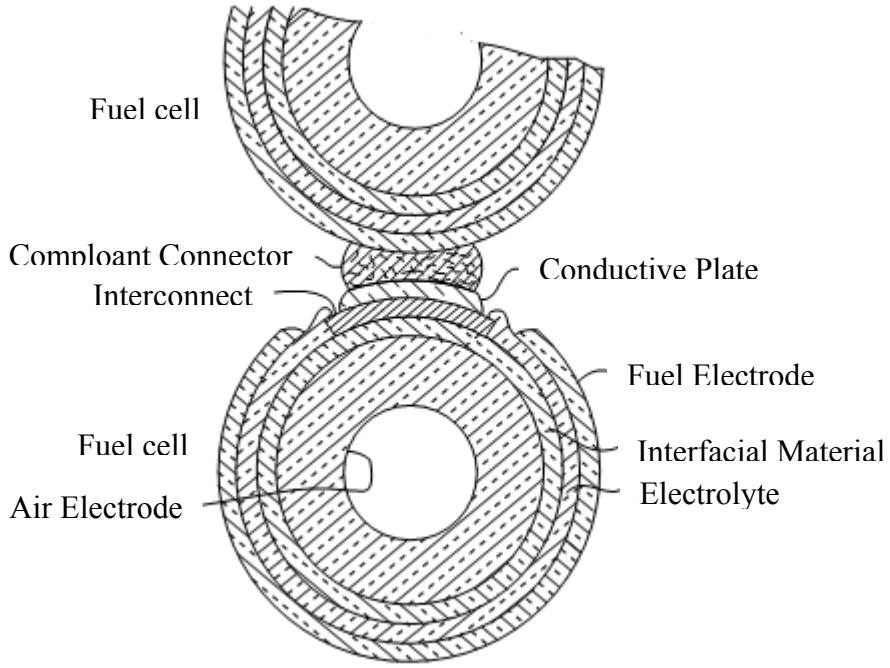

Figure 5: Tubular solid oxide fuel cell model

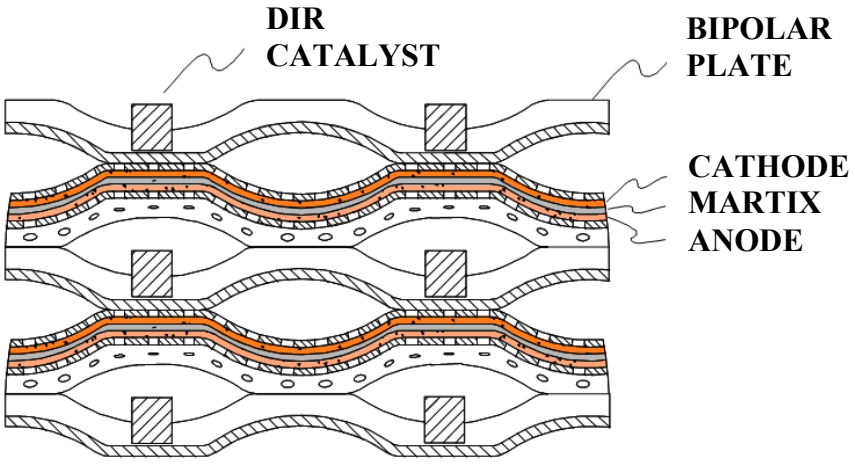

Figure 6: Monolith SOFC design; cross section

1.6 Electrolyte for Solid Oxide Fuel Cells

Electrolyte materials for high temperature SOFCs need to exhibit high oxygen ion conductivity. As stated above that the electrolyte is the most important part of a fuel cell system. Table 1 show each type of fuel cell is dependent on the electrolyte. Today we recognize three major electrolyte material groups: ceramic, polymer and aqueous. Furthermore, with respect to the material group where it belongs, some general material requirements of fuel cell electrolytes are listed below:

- Electrolyte must be fully dense.
- High ionic conductivity is essential, but electronic conductivity needs to be very low or non-existed.
- Must be chemically stable to resist oxidation operating at high temperatures.
- Must have phase stability to allow for operation at high temperatures over time.
- Reasonable mechanical and thermal shock resistance, high mechanical strength and fracture resistance in the case of solid electrolytes.
- Simplicity of available production technologies and low cost are important for fabrication of the electrolyte material.

Fluorite based structure such as zirconia (ZrO_2) and ceria (CeO_2) correctly substituted with cations of yttrium (Y^{+3}) and ytterbium (Yb^{+3}) are the most characterized oxygen ion conductors [17]. Some fluorite based structure systems with oxygen ion conductivity are presented in Fig. 7 [18].

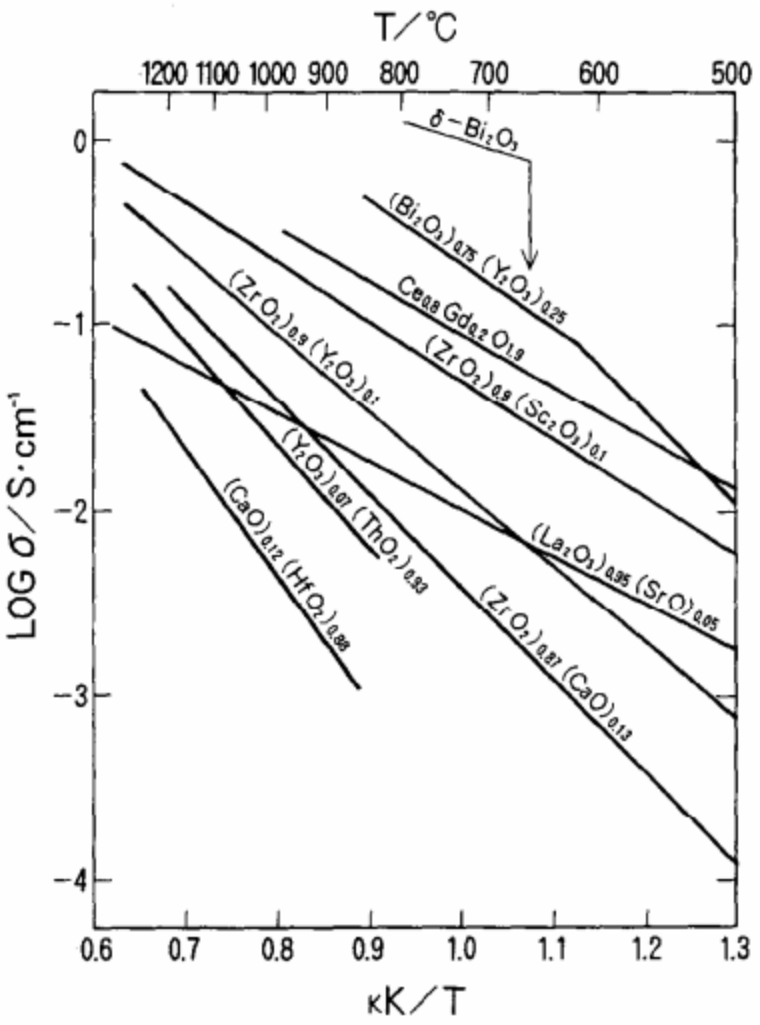

Figure 7: Total conductivity vs. temperature for fluorite base structure materials with oxygen ion conductivity

Over time many electrolyte materials have been developed for Solid Oxide Fuel Cells and most common among those is 8 mole % Y_2O_3 (yttria trioxide) stabilized ZrO_2 (zirconia oxide), also known as yttria stabilized zirconia (YSZ) [19]. This material is known by its high mechanical, chemical, and thermal stability. Yttria stabilized zirconia has been mostly used in high temperature (~1000^{o}C) Soli Oxide Fuel Cell systems [20]. This electrolyte material

has the ionic conductivity of 0.1 S cm^{-1} at 1000^{o}C but at a temperature of 800^{o}C the ionic conductivity decreases to 0.03 S cm^{-1}. This drop in conductivity is problematic for applications of yttria stabilized zirconia (YSZ) electrolyte [21]. For this reason the researchers focus more on development of electrolyte materials which are characterized by high conductivity at temperatures lower them 800^{o}C.

1.7 Zirconia (ZrO_2) and its dopents

Zirconia (ZrO_2) may appear in three different crystal structures, cubic, tetragonal, and monoclinic, depending on the temperature. At room temperature, pure ZrO_2 is monoclinic and transforms from tetragonal to cubic at elevated temperatures. Due to increase in volume, which is caused by the phase transformation from cubic to tetragonal to monoclinic phase, very large stresses are provoked, and this may yield fracturing of ZrO_2 upon cooling from high temperature.

The disordered cubic and tetragonal phases are built on tetravalent ions of zirconium (Zr^{4+}) in face centered cubic packing with oxide ions located at the tetrahedral sites. Each zirconium ion is surrounded with eight oxygen atoms and each oxygen at tetragonal site is coordinate by four zirconia. Typical schematic of the fluorite structure is shown in Fig. 8 [22].

Appropriate substation of Zr^{+} with certain dopants stabilizes the cubic structure of zirconia (ZrO_2) from room temperature to its melting point [23]. In Fig 9 is presented the phase diagram of the $ZrO_2 - Y_2O_3$ system. From the phase diagram, the cubic phase of the system exists in a wide range of temperatures and composition [23].

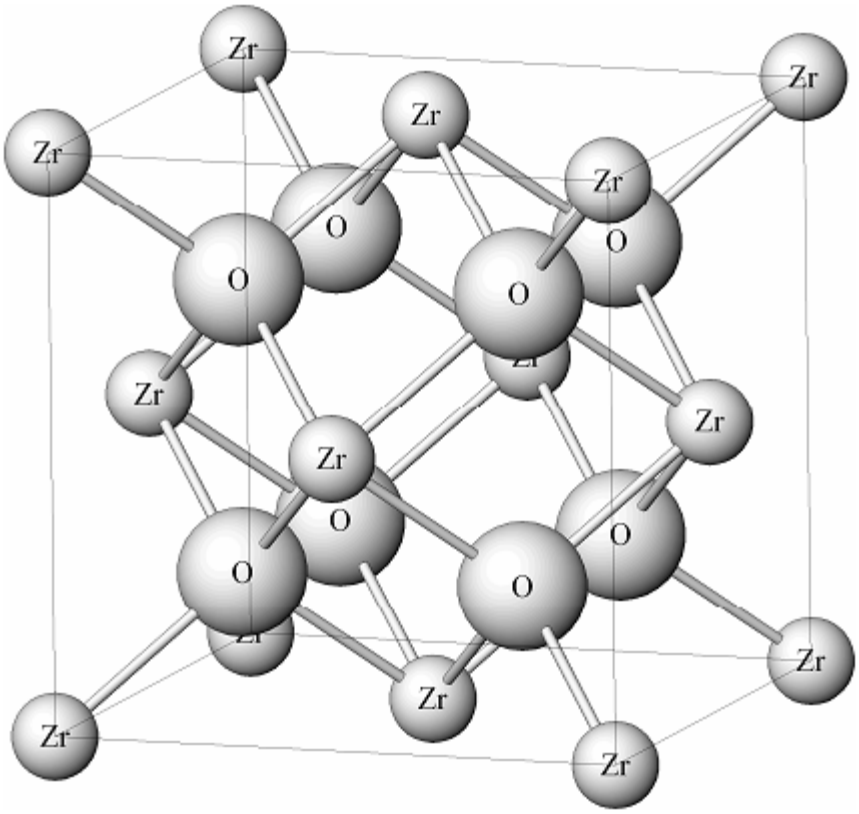

Figure 8: ZrO2 cubic fluorite structure with oxide ions occupying all tetrahedral sites

In order to attain high oxide conduction, part of Zr^{4+} must be replaced with some other lower valence state cations, mostly Y^{3+}, Sc^{3+}, Ca^{2+} [24]. This doping, depending on the temperature and the concentration of the dopant, allows stabilization of the cubic or the tetragonal phase. Concentrations of a dopant, as well as the concentration of vacancies are very important for the ionic conductivity. In case of yttria stabilized zirconia the maximum of ionic conductivity has been found for 8 mol % of Y_2O_3 – ZrO_2 and conductivity decreases beyond this pint. Fig. 10 shows relation between conductivity and concentration for some ZrO_2 base electrolyte materials [25]. Increase in temperature may produce an increase in conductivity since the mobility of the defects improves in high temperature environment.

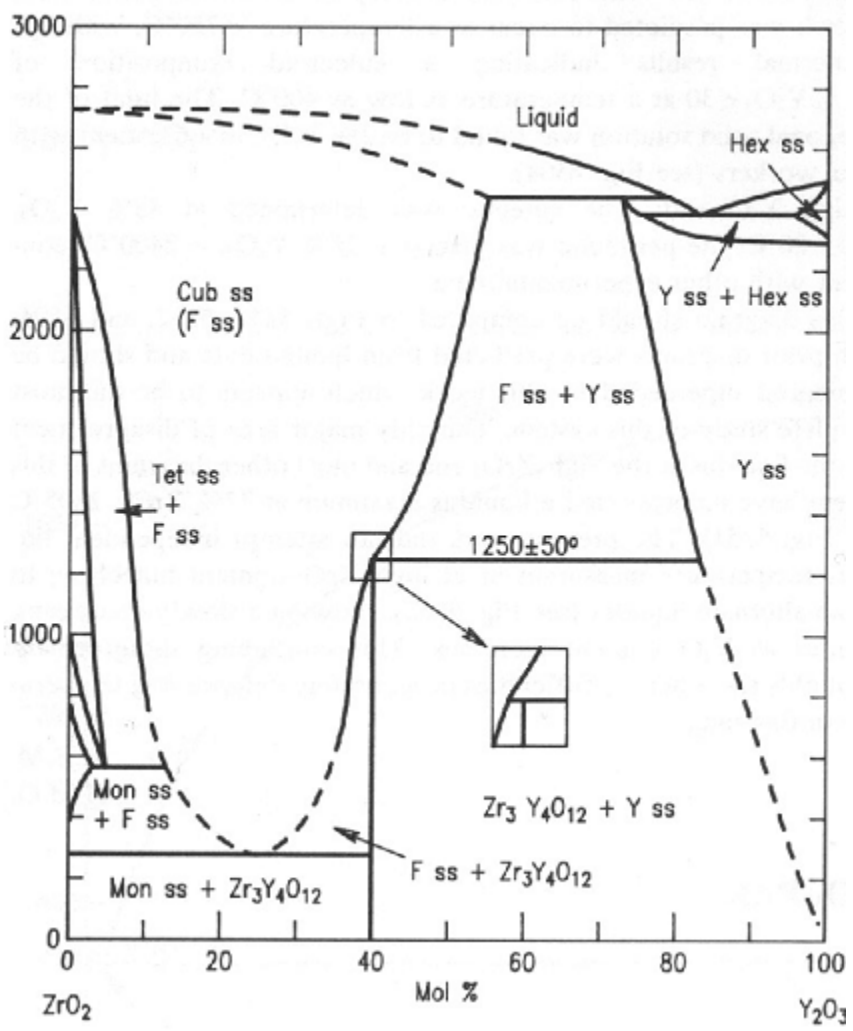

Figure 9: Phase diagram for the ZrO2 – Y2O3 system

Some studies of zirconia based fluorite structures doped with CeO_2, Y_2O_3, Sc_2O_3 in order to reduce the cost, stabilize the cubic phase of zirconia and improve ionic conductivity at lowered temperatures are reported in [26,27]. After a number of investigations in ZrO_2 based electrolytes for intermediate temperature fuel cells, it has been concluded that Sc_2O_3-doped ZrO_2 ceramics have the highest conductivity at the concentration of 10 mol % Sc_2O_3 dopant, compared to other zirconia based electrolytes [28]. Concentration of Sc_2O_3 has been investigated in the range between 7and 13 mol % Sc_2O_3. In this range Sc_2O_3 has very high ionic conductivity with a

maximum at 10 mol % of dopant. Ionic conductivity increases with increase of the dopant concentration until it reaches the value around 7 mol %, then conductivity gradually reaches the maximum at 10 mol % of dopant, where it slightly decreases with continuation in increase of the concentration [29].

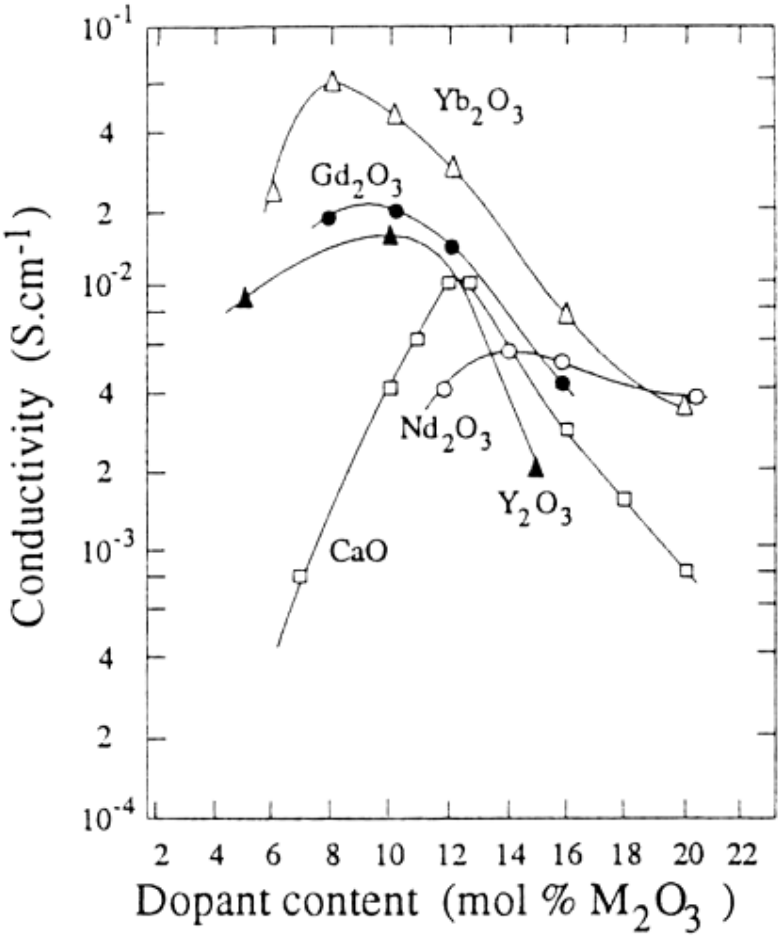

Figure 10: Conductivity vs. concentration for ZrO2 – based electrolytes

However, Sc_2O_3 reveal some vacancies over time which causes aging of material and the phase transformation. In the range from 17 to 13 mol % scandia show two different arrangements. For concentration of Sc_2O_3 less than 10 mol % scandia doped zirconia shows a cubic phase. A change in crystal structure takes place when the concentration of Sc_2O_3 is greater than 10 mol %

($11Sc_2O_{3)}$ and it appears as rhombohedral phase. The rhombohedral phase is stable only at temperatures less than 450°C, and it transforms into a cubic phase at elevated temperature. At temperatures over 750°C only cubic phase is present [30,18]. Phase diagram Sc_2O_3 stabilize ZrO_2 is presented in Fig. 11 [32].

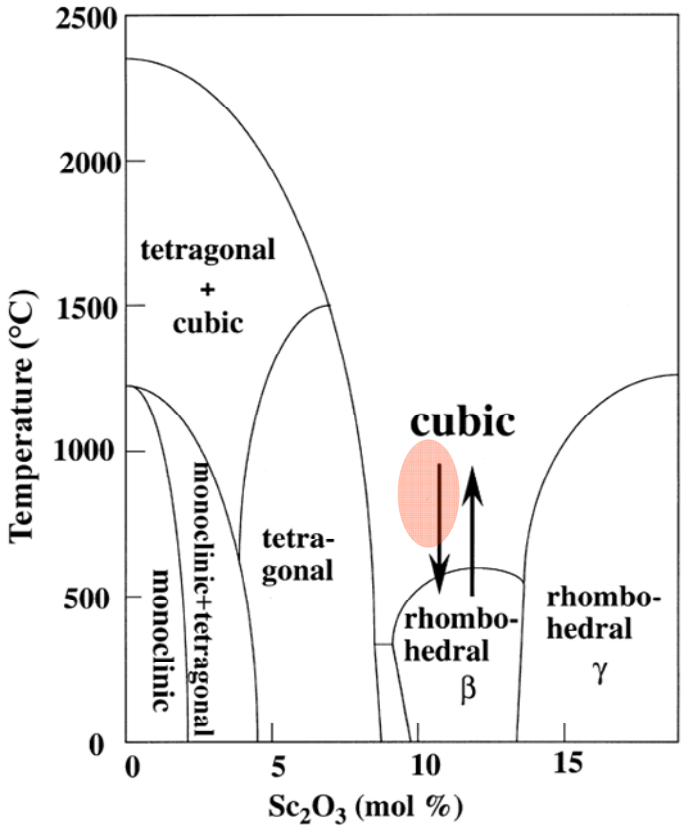

Figure 11: Phase diagram of Sc2O3 – ZrO2 system

It has been reported that Sc_2O_3-doped ZrO_2 system has four major phases, monoclinic, tetragonal, rhombohedral β, and rhombohedral γ. As it can be seen out of the phase diagram in Fig. 11 transition between cubic and rhombohedral phase takes place at temperature of 650°C for scandia stabilized zirconia system [32]. This phase transformation could cause change in volume what would result with damage in the electrolyte.

The cubic phase is not stable at temperatures below 650^{o}C and this causes a decrease in ionic conductivity upon cooling process. In addition, due to development of the tetragonal phase in the cubic structure at temperatures from 700^{o}C to 1000^{o}C some aging effects have been registered in scandia stabilized zirconia electrolyte [33].

In order to make Sc_2O_3 doped ZrO_2 possible electrolyte material for SOFCs the high temperature cubic phase needs to be stabilized at low temperatures, which is a desirable condition for intermediate temperature Solid Oxide Fuel Cells. One way to have cubic phase stabilized at lower temperatures is embracement of some additional dopants with $Sc_2O_3 - ZrO_2$ system, such as CeO_2 [34], Sm_2O_3 [35], Al_2O_3 [32] and Yb_2O_3 [36]. In Ref. [37], when ZrO_2 was doped with Sc_2O_3 and CeO_2 has successfully stabilized high temperature cubic phase to that of room temperature, and this electrolyte material can be used for intermediate temperature SOFCs.

1.8 Goals of Work

The purpose of the electrolyte is to achieve optimum efficiency. Mechanical, chemical, and electrical properties of a successful electrolyte are necessary. After indentifying a material with acceptable electrochemical and thermal properties, the mechanical properties of the electrolytes must be characterized in order to ensure durability and good performance. The objective of this research is characterization of the vibrational and mechanical properties of the electrolyte material for intermediate temperature SCFCs.

This study is based on classification and analysis of phase stability, sintering behavior, vibretional response, mechanical and microstructure properties of one out of two commercially available 10 mol% Sc_2O_3 – 1 mol % CeO_2 – ZrO_2 ceramic powders. One powder was fabricated by Praxair Surface Technology, USA and other by Daiichi Kigenso Kagaku Kogyo (DKKK), Japan. The electrolyte material made from the powder manufactured in Japan by DKKK is the subject matter in this research. Some fundamental differences between DKKK and Praxair materials are stated in Chapter 2 explaining why the DKKK material has been chosen over Praxair for further learning. Mechanical properties such as hardness (H_v), fracture resistance (K_{Ic}), and thermal properties are very important for development and design of electrolyte for intermediate temperature SOFCs.

Besides this, the grain size of each of the manufactured sample powder which were produced at the temperature range 1100-1600^oC and sintered at different sintering temperatures is very important in determination of phase stability (ionic conductivity) of the material.

In addition, the goal of this research is to study the spectra of cubic and rhombohedral phases, as well as, to detect temperature and stress induced deformation and phase transitions in zirconia using Raman spectroscopy.

CHAPTER 2:
LITERATURE REVIEW

This chapter focuses on the materials investigated in previous study, and the materials involved in this research work. ScCe-stabilized zirconia powder, which is produced by two companies, Daiichi Kigenso Kagaku Kogyo (DKKK, Japan) and Praxair (USA), is overviewed for its different sintering behaviors, microstructure and phase transformation. Also, advantages of DKKK materials over Praxair explain why DKKK is chosen for further study.

2.1 Material overview

In this research work two powders with composition $Sc_{0.1}Ce_{0.01}ZrO_2$ have been characterized in respect to their mechanical, thermal and vibrational properties. One powder is manufactured by Daiichi Kigenso Kagaku Kogyo (DKKK), Japan and other by Praxair, USA. The manufacturing process of each powder was different. DKKK powders have been fabricated by a wet co-precipitation technique. The co-precipitation technique controls very efficiently the chemical composition and morphology of the prepared powders [38]. This technique is one of the most successful wet-chemical techniques for synthesizing ceramic powders with narrow particle size distribution [39,40]. Praxair powders are manufactured by spray pyrolysis method. The spray pyrolysys technique is an option to attain complex oxides at relatively low temperature, and it is based on controlled formation of an aerosol followed by thermal treatment and powder collection [41]. During the process of spray pyrolysys morphology can be changed, the homogeneity, particle size distribution, and the phase composition [42,43].

In previous research the morphological characteristics, distribution of the particles and their size have been investigated for both powders.

Even though the normal composition of the DKKK and the Praxair powders are the same, the exact chemical compositions are 9.51 mol % Sc_2O_3 + 1.49 mol % HfO_2 + 1.21 mol % CeO_2 + 87.07 mol % ZrO_2 and 9.02 mol % Sc_2O_3 + 1.51 mol % HfO_2 + 1.91 mol % CeO_2 + 0.18 mol % TiO_2 + 88.1 mol % ZrO_2 for DKKK and Praxair powders respectively. This was discovered after inductivity coupled plasma mass spectroscopy measurements (ICP MS) and reported in [21] together with measured values of the specific surface area (SSA), grain size distribution and theoretical density (ρ_{th}), all presented in Table 2 [21]. The impurities are present in both powder representatives. Praxair powders have higher impurity level than DKKK, but the elements of interest, Sc, Ce, Zr are present in close amount.

Table 2: Properties of $ScCeZrO_2$ powders

			Grain size, μm		
Powder manufacturer	Specific Surface Area SSA, m^2 / g	Theoretical density ρ_{th}, g / cm^3	d_{10}	d_{50}	d_{95}
DKKK	10.4	5.827	0.42	0.6	1
Praxair	4.34	5.845	0.6	1	2.5

2.2 Previous study review of DKKK and Praxair powders (XRD, sintering and phase stability)

Through the study of the properties and morphology of the DKKK and Praxair powders it has been concluded both differ considerably. Scanning Electron Microscopy (SEM) analysis revealed the particle size of both powders, and Praxair particles are almost double the size of DKKK, Fig. 12 [21].

DKKK powders have uniform nanograins in size of 60-100nm, while Praxair powders consist of 30 μm in length and 3-4 μm in thickness pre-sintered agglomerates of smaller 100-200nm particles. This difference in the particle size of the DKKK and Praxair powders led to further dissimilarity in sintering behavior causing the shrinkage of the Praxair powders.

X-Ray Diffraction exposed that the DKKK and Praxair powders of 10 ,mol % Sc – 1 mol % Ce – ZrO_2 is a mixture of a cubic and rhombohedral phase, what is opposite to ref. [37]. Out of DKKK and Praxair XRD patterns taken at room temperature, 500^{o}C and 600^{o}C rhombohedral phase is evident, Fig. 13 [21]. It is shown that the DKKK materials have 79% of cubic and 29% of rhombohedral phase, and 88% of cubic and 12% of rhombohedral phase is present in Praxair powders [21].

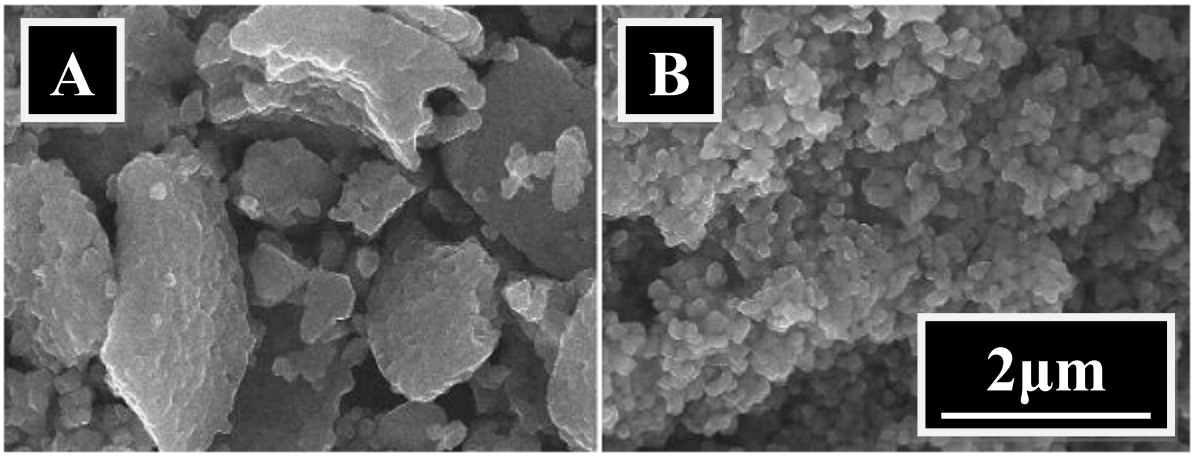

Figure 12: SEM images of A) Praxair and B) DKKK powders

As DKKK and Praxair powders are heated from room temperature up to 500^{o}C rhombohedral phase is identified. As temperature went by 500^{o}C phase transition from rhombohedral to cubic

takes place and upon further heating over 500^{o}C no rhombohedral phase is present in powders. However, during cooling process back to room temperature the rhombohrdral phase reappears and establishes in the same amount. Under this observed circumstance has been concluded that the transition of rhombohedral phase to cubic of 10 mol% Sc-1 mol % Ce-ZrO_2 ceramics is reversible process in respect to temperature.

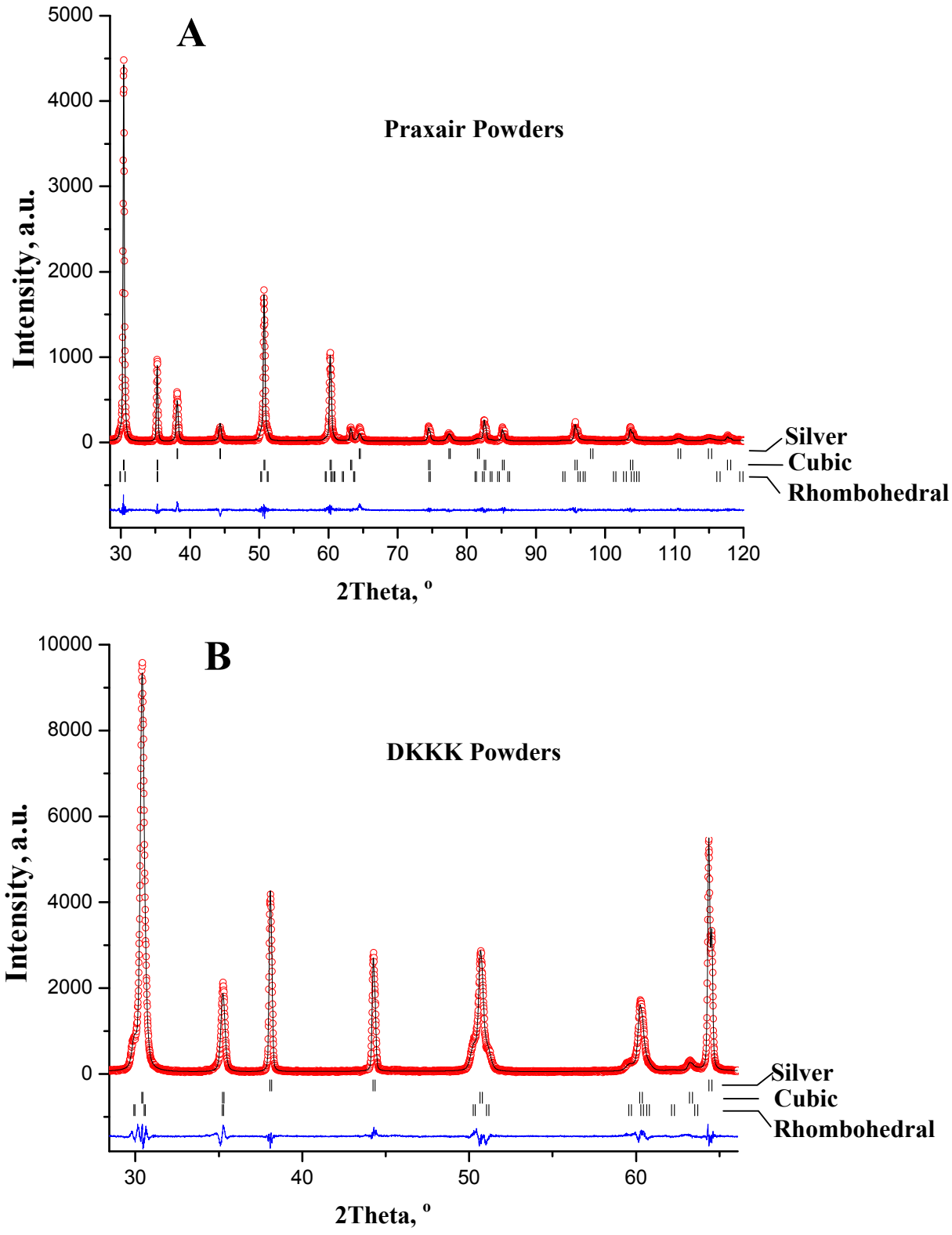

Figure 13: XRD patterns of A) Praxair and B) DKKK powders

Sintering behavior of the DKKK and Praxair powders differ since these two materials have different impurity levels, morphology of the powders and the chemical composition. Earlier studies have recognized during the process of sintering, the DKKK powder is more active and requires around 200°C lower temperature to create ceramic material of the same porosity level as material produced by sintering Praxair powder, Fig. 14 [21]

It is possible to achieve very dense zirconia based materials by sintering at temperature in the range from 1300°C to 1600°C. Sintering over long period of time at the temperature close to the end of the range 1300°C-1600°C will result in large grained materials. [44,45]. Large grains have negative impact on mechanical and electrical properties of material, so they are undesirable.

Theoretical densities of the powders, 5.827 g/cm^3 and 5.845 g/cm^3 for DKKK and Praxair respectively, Table 2, which are established by the true chemical composition of the materials and XRD, are used in calculation of the amount of porosity of the $ScCeZrO_2$ powders.

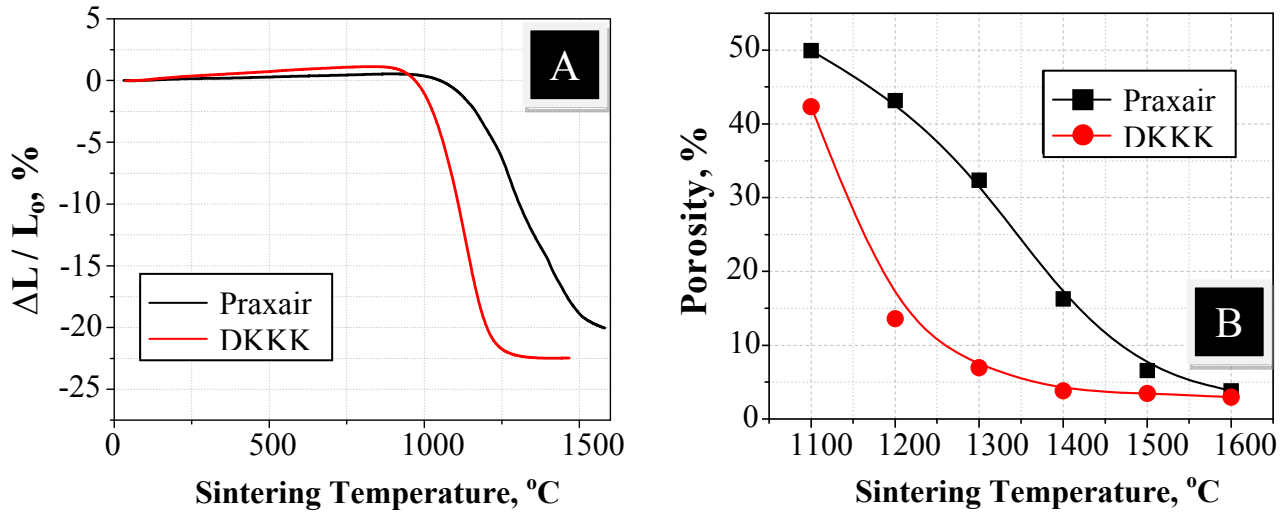

Figure 14: Sintering behavior of DKKK and Praxair powders; A) Material Shrinkage vs. sintering temperature; B) Porosity level vs. sintering temperature

During sintering from 1000°C to 1400°C the density of the $Sc_{0.1}Ce_{0.01}ZrO_2$ produced by DKKK increases quickly and becomes constant at higher sintering temperature.

In Fig. 15 [21] are shown the measurements of the grain size as received DKKK and Praxair powders as a function of sintering temperature. The grain size increase with increase in temperature, and DKKK $ScCeZrO_2$ materials have the grain size stabilized at 1500°C while Praxair materials are not fully sintered at the same temperature.

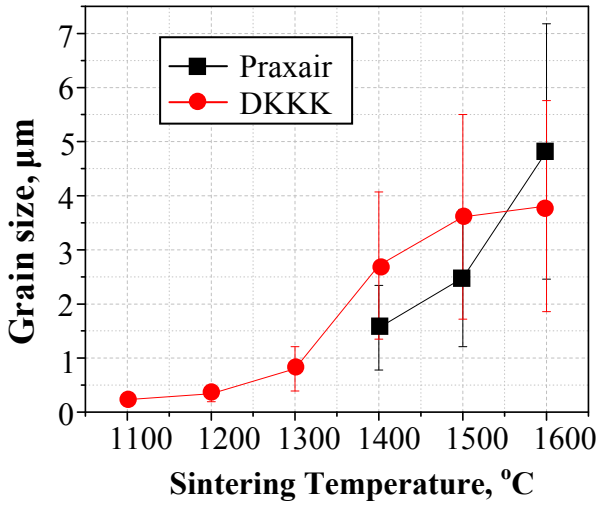

Figure 15: Grain size vs. sintering temperature of DKKK and Praxair powders

Fig. 16 and 17 show microstructure of the Praxair and DKKK powders as sintered at different sintering temperatures [21].

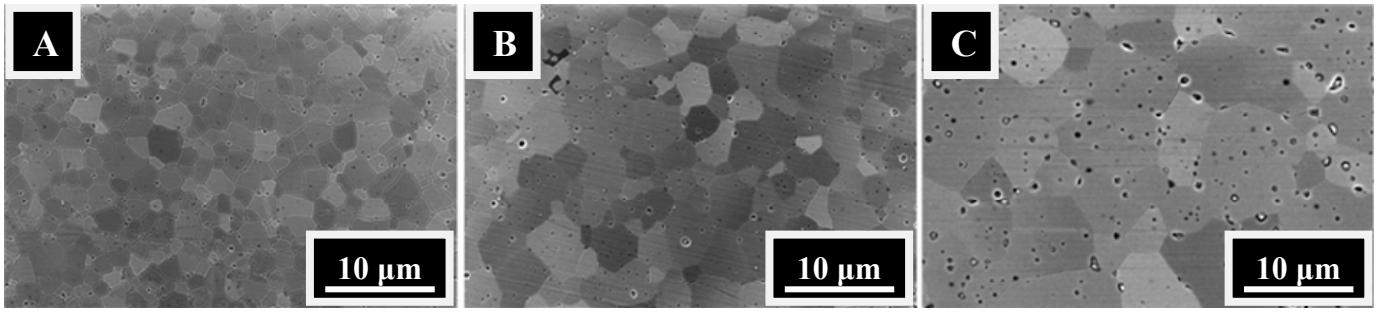

Figure 16: Microsrtucture of Praxair powders sintered at A) 1400°C, B) 1500°C, C) 1600°C

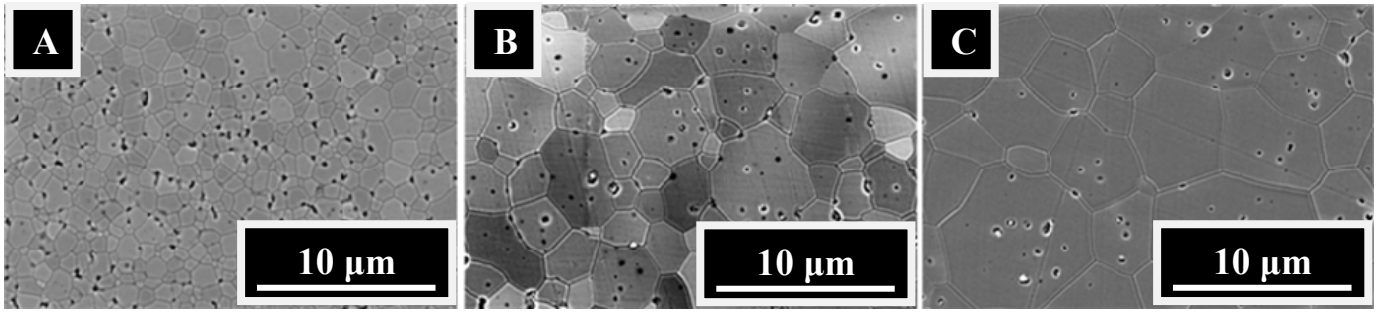

Figure 17: Microsrtucture of DKKK powders sintered at A) 1300°C, B) 1500°C, C) 1600°C

Grain size and the cavity of the powders in a function of the sintered temperature are given in Table 3 [21].

Table 3: Grain size vs. sintering temperature for DKKK and Praxair powders

Powder manufacturer	Sintering temperature, °C	Grain size, µm	Cavity, %
DKKK	1300	0.80	2.60
	1400	2.71	1.00
	1600	3.81	0.94
Praxair	1400	1.56	0.55
	1500	2.48	0.68
	1600	4.82	1.14

Phase stability of the DKKK and Praxair $ScCeZrO_2$ materials is in relation with their sintered temperature. Former study showed, out of several XRD analyses that both DKKK and Praxair powders exist in a mixture of cubic and rhombohedral phase at room temperature when sintered at temperature from 1100°C to 1300°C, and when sintered at temperature from 1400°C to 1600°C only cubic phase is present at room temperature. This study confirmed that the phase transformation of the cubic to rhombohedral upon heating and the rhombohedral to cubic phase upon cooling, for DKKK materials was obtained in the temperature range from 300°C to 500°C.

Yet, the Praxair materials have pure cubic phase in the range from RT to 900°C. All phase transformation relative to the sintering temperature of the DKKK ceramic materials are presented in Table 4 [21].

Table 4: Phase transition in dependence of sintering temperature for DKKK ScCeZrO2 ceramics

Powder source	Sintering temp.	Phase transition step 1	Phase transition step 1 temp.	Phase transition step 2	Phase transition step 2 temp.	Phase transition step 3	Phase transition step 3 temp.	Phase transition step 4	Phase transition step 4 temp.
DKKK	1100°C & 1200°C	β→c	RT-500°C	100% c	above 500°C				
	1300°C	c→β	RT-300°C	50% c & 50% β	400°C	β→c	500°C	100% c	above 500°C
	1400°C	80% β & 20% c	RT-400°C	β→c	500°C				
	1500°C & 1600°C	c→β	350°C	100% β	370°C	β→c	430°C	100% c	above 470°C

Fractions of the cubic and rhombohedral phase for materials manufactured by DKKK at different temperatures are shown in Fig. 18.

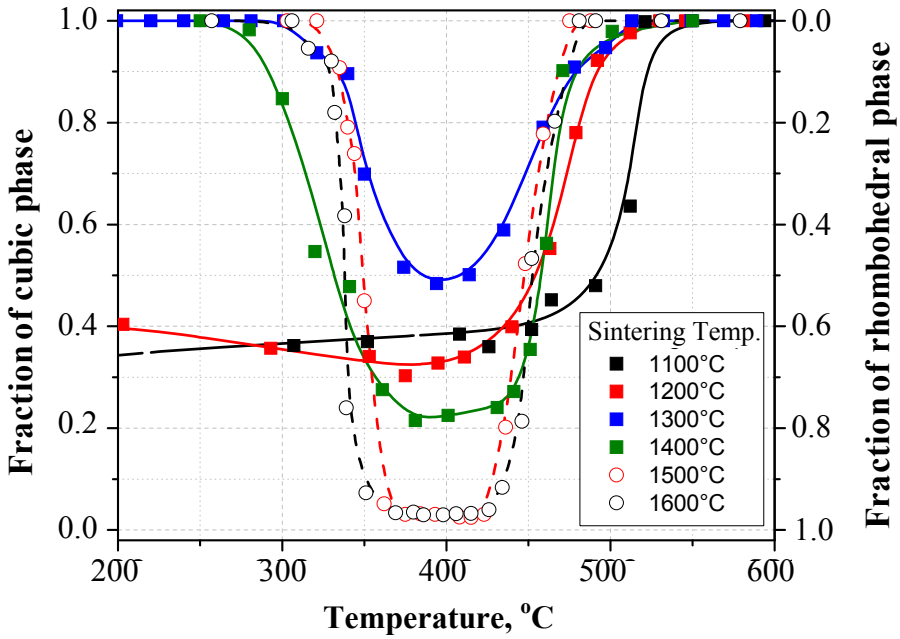

Figure 18: Multiphase investigation of DKKK powders at different temperatures

2.3 DKKK vs. Praxair

Major differences between the $Sc_{0.1}Ce_{0.01}ZrO_2$ powders fabricated by DKKK, Japan and Praxair, USA are listed below.

- DKKK as opposed to Praxair powders have smaller grain size and it is more uniform to allow this material to create fully dense ceramic electrolytes for Solid Oxide Fuel Cells.
- DKKK achieves better sinterability than Praxair. This material requires almost 200°C less temperature to produce lower porosity ceramics.
- DKKK materials have partially phase transformation from cubic to rhombohedral in the range 300°C-500°C. Praxair has fully stable cubic phase over temperature from RT to 900°C.

- DKKK materials have higher ionic conductivity which is very important to the design and production of electrolyte materials.
- Mechanical properties, such as hardness, fracture resistance, Young's modulus, strength are higher for DKKK ceramics then those produced from Praxair materials.

CHAPTER 3:
METHODOLOGY

The micro-Raman spectroscopy is used in the research on the vibrational behavior of cubic and rhombohedral $Sc_{0.1}Ce_{0.01}ZrO_2$. This is a powerful tool which can be successfully used to characterize the zirconia structures and their stress states. The whole available spectral range of cubic and β-$Sc_{0.1}Ce_{0.01}ZrO_2$ has been collected using Si-532nm and NIR-785nm lasers. The mechanical properties, such as hardness, indentation fracture resistance, Young's modulus, and strength, of $Sc_{0.1}Ce_{0.01}ZrO_2$ have been measured.

3.1 Introduction to vibrational properties of $Sc_{0.1}Ce_{0.01}ZrO_2$ ceramics

Sc_2O_3 doped ZrO_2 ($ScZrO_2$) ceramics have recently attracted a significant interest as a novel promising electrolyte material for lower temperature SOFCs due to its excellent ionic conductivity [46,47,48]. There have been numerous reports on the high ionic conductivity of $ScZrO_2$ ceramics [28,34] which was reported to be nearly twice as high as other ZrO_2 based electrolytes [49]. Most of the studies of $ScZrO_2$ ceramics were performed on the materials with 8-12 mol% doping level of Sc_2O_3, where a cubic phase is a main single phase at 700-800^oC operating temperatures. The drawback of $ScZrO_2$ has been also reported as an ordering of vacancies over time, called the aging phenomenon, accompanied by a phase transition to a lower symmetry rhombohedral phase, resulting in decreased conductivity [49]. The highly conductive cubic phase is not stable below 650^oC causing the abrupt decrease in ionic conductivity during cooling in the $ScZrO_2$ [50,35]. It is known that in 11 mol% Sc_2O_3 – 89 mol% ZrO_2, a cubic to rhombohedral phase transition occurs when the temperature decrease below 600^oC [51,52]. It was reported [37,53] that when ZrO_2 is stabilized with a small amount of CeO_2 along with Sc_2O_3,

it no longer exhibits an unfavorable phase transition, making this material a very promising option for intermediate temperature electrolytes.

In ref. [37], the commercially available 10 mol% Sc_2O_3 – 1mol% CeO_2 – ZrO_2 further referred as $Sc_{0.1}Ce_{0.01}ZrO_2$, manufactured by Daiichi Kigenso Kagaku Kogyo (DKKK, Japan) has been reported to have a stable cubic phase, superior electrical properties and excellent high temperature long term operating characteristics of single cells using $Sc_{0.1}Ce_{0.01}ZrO_2$ as an electrolyte material. Contrary, the reversible very slow cubic to rhombohedral and rhombohedral to cubic phase transitions at 300-500^oC has been reported upon heating of $Sc_{0.1}Ce_{0.01}ZrO_2$ ceramics using X-ray diffraction [21], which were probably overlooked in other studies due to extremely slow kinetics of cubic to rhombohedral phase transition upon heating. Thus, it was recently shown that the high temperature cubic $Sc_{0.1}Ce_{0.01}ZrO_2$ is a metastable phase at room temperature and could be easily transformed to the thermodynamically stable rhombohedral phase upon annealing at 350-400^oC after at least 12 hours of annealing. However, it is not expected that these transitions could have a significant effect on $Sc_{0.1}Ce_{0.01}ZrO_2$ electrolyte performance since they occur at lower temperatures and could simply be bypassed during heating up or cooling down cycles of the cells. It was reported that the kinetics of the phase transition is a strong function of the grain size of the $Sc_{0.1}Ce_{0.01}ZrO_2$ ceramics [21], and it was also found that the coefficient of thermal expansion of cubic $Sc_{0.1}Ce_{0.01}ZrO_2$ is very close to the Y_2O_3 stabilized ZrO_2 (YSZ) which is a good indicator that $Sc_{0.1}Ce_{0.01}ZrO_2$ ceramics are a perfect candidate for substitution of YSZ electrolyte SOFCs.

It has been recognized that while XRD patterns are determined by the arrangements of the cations (Zr, Sc, Ce) in the fluorite lattice, laser-excited Raman spectra are sensitive to the change of the polarizability of cation-oxygen vibrations and can easily give important information about the crystal structure of $Sc_{0.1}Ce_{0.01}ZrO_2$. The different ZrO_2 structures (monoclinic, tetragonal, rhombohedral, and cubic) all have characteristic signatures in their spectra, which enable them to be easily distinguished. Besides, the strain/stress in the material can be detected from the shift of the certain peaks. The $Sc_{0.1}Ce_{0.01}ZrO_2$ ceramics under study have been previously characterized by XRD [21], but the goal of this research is to study the spectra of cubic and rhombohedral phases as well as to detect temperature and stress induced deformation and phase transitions in zirconia using Raman spectroscopy.

3.2 Introduction to mechanical properties of $Sc_{0.1}Ce_{0.01}ZrO_2$ ceramics

Materials for use in efficient energy systems such as solid oxide fuel cells (SOFCs) and oxygen separation membranes have been characterized extensively with respect to their electrochemical and thermal properties, which are vital in determining how successful the materials could be for a given application. However, when the material has been identified with a superior set of electrochemical and thermal properties its mechanical properties must be characterized to ensure that the new material would be able to withstand the existing loading conditions during operation, and this report will address the mechanical behavior of promising $Sc_{0.1}Ce_{0.01}ZrO_2$ electrolyte.

To the best of our knowledge there were no reports on mechanical performance of $Sc_{0.1}Ce_{0.01}ZrO_2$ ceramics and this research aims on filling the gap. There are, however, many similar materials that have been tested to determine their mechanical behavior. Hirano [54] reports that increasing scandia doping from 3 to 7 mol% in tetragonal zirconia leads to dramatic decrease in both strength and fracture toughness of the material. For composition with 3 mol% Sc_2O_3 doping strength and fracture toughness were reported to be 640 MPa and 3.8 MPa $m^{1/2}$, respectively, but for 7 mol% Sc_2O_3 doping the properties decreased to 335 MPa for strength and 2.7 MPa $m^{1/2}$ for fracture toughness. Another paper [55] reports the similar trend for YSZ ceramics, where fracture toughness values of 4.6, 1.3 and 1.8 MPa $m^{1/2}$ were measured for 3, 8 and 11 mol% of Y_2O_3 doping, respectively. The decrease in strength and fracture toughness as a function of doping level is a result of decrease in the amount of tetragonal metastable phases. This phase allows the material to gain the strength by tetragonal-to-monoclinic phase transformation due to the induced stress. It is also obvious, that the lower crystal symmetry of ZrO_2 phases, such as rhombohedral or tetragonal, have a significant number of defects, such as twins, antiphase domains, dislocations or staking faults that contribute to toughening by interacting with a moving crack or stress fields, thus absorbing extra energy and providing the material with a higher crack resistance. At the same time, the cubic ZrO_2 phase does not possess any twins, staking faults, or other significant defects except for the high oxygen vacancies concentration and, therefore, its mechanical properties are expected to be lower than that of the materials with tetragonal or rhombohedral structures.

In addition, the mechanical properties, such as hardness, fracture toughness, and strength at room and high temperatures along with RT compressive stress-strain deformation behavior are reported in this study for cubic and rhombohedral $Sc_{0.1}Ce_{0.01}ZrO_2$ ceramics produced using DKKK powders.

For comparison, another $Sc_{0.1}Ce_{0.01}ZrO_2$ material, sintered from powders produced by Praxair, has also been characterized.

3.3 Experimental Procedure

The 10mol% Sc_2O_2 – 1mol% CeO_2 – ZrO_2 ($Sc_{0.1}Ce_{0.01}ZrO_2$) powder produced by Daiichi Kigenso Kagaku Kogyo (DKKK, Japan) has been sintered at 1500^{o}C for 2 hours with a 10^{o}C/min heating/cooling rate in air to almost full density. The detailed processing of the $Sc_{0.1}Ce_{0.01}ZrO_2$ as well as it selected properties, such as strength, hardness, fracture toughness, Young's modulus, as well as preliminary Raman data are presented in details elsewhere [21, 56,57,58]. The XRD confirms that the material consists of the cubic phase upon cooling after sintering at 375^{o}C for 12 hours [21]. The cubic $Sc_{0.1}Ce_{0.01}ZrO_2$ samples were grinded and polished in order to obtain the mirror surface and then they were thermally etched at 1300^{o}C for 1 hour to reveal the grain boundaries. A portion of the thermally etched cubic $Sc_{0.1}Ce_{0.01}ZrO_2$ samples were annealed at 375^{o}C for 12 hours in air in order to convert them to the rhombohedral phase, which is stable in 25 - 400^{o}C temperature range [21]. Both cubic and rhombohedral $Sc_{0.1}Ce_{0.01}ZrO_2$ phases were indented using Vickers hardness tester (LECO M-400) with a load of 9.8N. The hardness and fracture toughness of the ceramics have been calculated using the length of the impression diagonals and cracks originating from the corners of the impressions,

respectively. Optical micrographs were taken using an Olympus confocal microscope (LEXT OLS3000-IR). This experimental procedure is described by a flow chart shown in Fig. 19.

Renishaw InVia Raman microscope (Fig. 20) was used to study the vibrational spectra of $Sc_{0.1}Ce_{0.01}ZrO_2$ ceramics. Raman spectroscopy is a technique that investigates lattice vibrations. Since the vibrational frequencies are sensitive to perturbation, external and internal, this technique is mostly used to study the composition, phase, crystal orientation and sometimes, doping of materials [59]. Raman spectroscopy measures intensity vs. frequency or wavenumber.

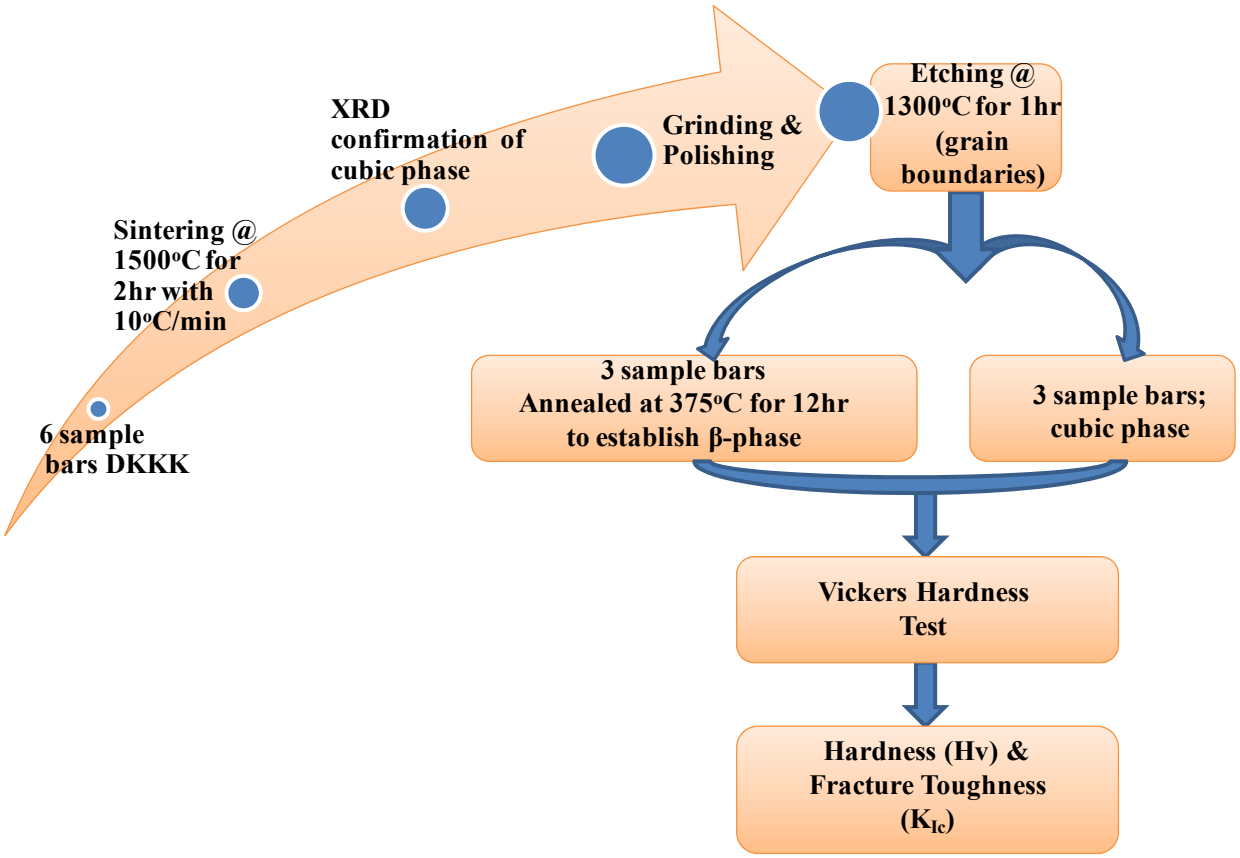

Figure 19: Flow chart of experimental procedure

In a Raman spectra collection, the light of a laser is focused on the sample. The spectrum of collected scattered lights is analyzed by a spectrometer and a charge-coupled device (CCD) detector.

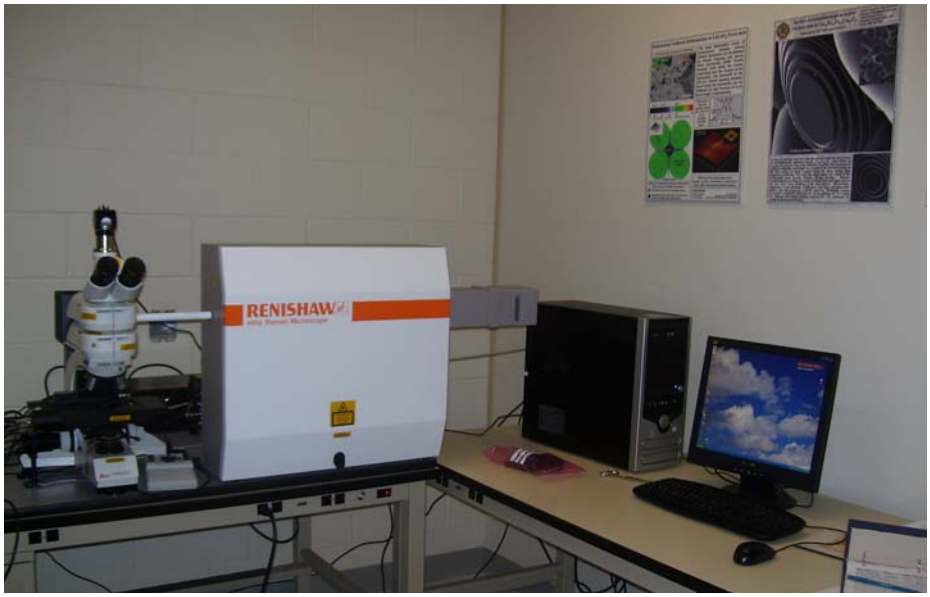

Figure 20: Renishaw InVia Raman spectrometer

The Raman microscope system comprises a laser (532 nm line of solid Si or near infrared 785nm) to excite the sample, a single spectrograph fitted with holographic notch filters, and an optical microscope (a Leica microscope with a motorized XYZ stage) rigidly mounted and optically coupled to the spectrograph. Before collecting spectra of $Sc_{0.1}Ce_{0.01}ZrO_2$ the spectrometer was calibrated with a Si standard using a Si band position at 520.3 cm^{-1}. The average collection time for a single spectrum was 20 s. High temperature Raman spectroscopy was performed using a TMS 600 and TMS 1500 heating stage (Linkam Scientific Instruments Ltd, UK) by heating/cooling of the samples to/from 400^{o}C and 1000^{o}C, respectively. For the high temperature experiment the incident and scattered beams were focused with a long working

distance 50x objective, which maintained a laser spot as small as 2-3 μm. A 10^{o}C/min heating/cooling rate was used for high temperature experiments**.** Different locations on the sample surface, the non-deformed polished surface, the stress field and inside the Vickers impressions, were used for collection of the Raman spectra at room temperature. For room temperature and area mapping experiments the short working distance 100x objective was used. To produce two dimensional (2D) maps, Renishaw Wire 2.0 software was used. This software works with a mixed Lorentzian and Gaussian peak fitting function. The system's peak fitting results were plotted to create a position map with a spectral resolution better than 0.2 cm^{-1}. The total time of spectrum collection was decreased to 3s per point in the case of 2D mapping and the total acquisition time to collect all spectra for one map never exceeded 24 hours.

For the indentation study, the uniaxially pressed pellets of the DKKK and Praxair powders were sintered at 1100-1600^{o}C for 2 hours with heating/cooling rate of 10^{o}C/min in air (Fig. 21 & 22). Sintered pellets were first ground using SiC paper and further polished down to 0.1 μm diamond grit size. Hardness tests were performed using a Vickers hardness tester TOKON-2100B in accordance with E 384-84 ASTM standard. Hardness and indentation fracture resistance of samples sintered at 1100-1600^{o}C were measured using 9.8N load, but samples sintered at 1500^{o}C for 2 hours (DKKK) and 1600^{o}C for 2 hours (Praxair) were subjected to loads of 0.25N, 0.5N, 0.98N, 2.94N, 4.9N, 9.8 N, 29.4N, 49.0N and 98.0N for a period of 15 seconds.

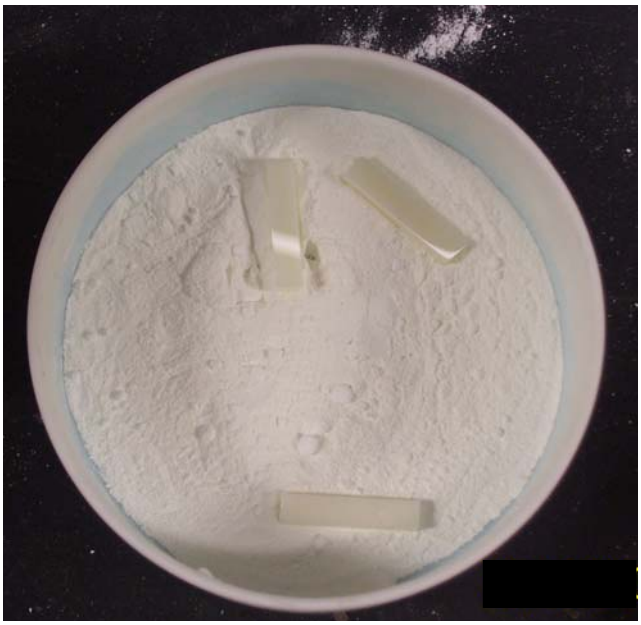

Figure 21: Sc0.1Ce0.01ZrO2 polished sample bars placed in DKKK sintering powder

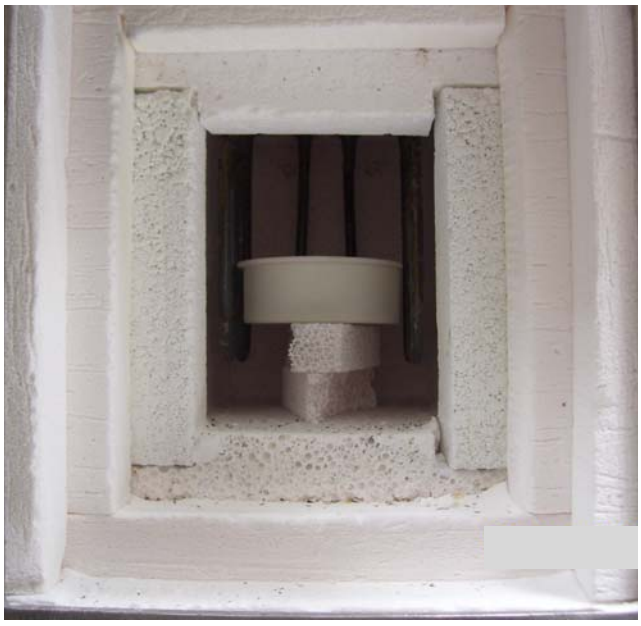

Figure 22: High temperature furnace used in sintering of the Sc0.1Ce0.01ZrO2 bars

The purpose of the Vickers indentation test is to measure resistance of material to penetration. Also, the indentation-induced cracking is related to fracture toughness. Vickers is a suitable test method because of four possible cracks that may develop from the corner of diamond shape indenter.

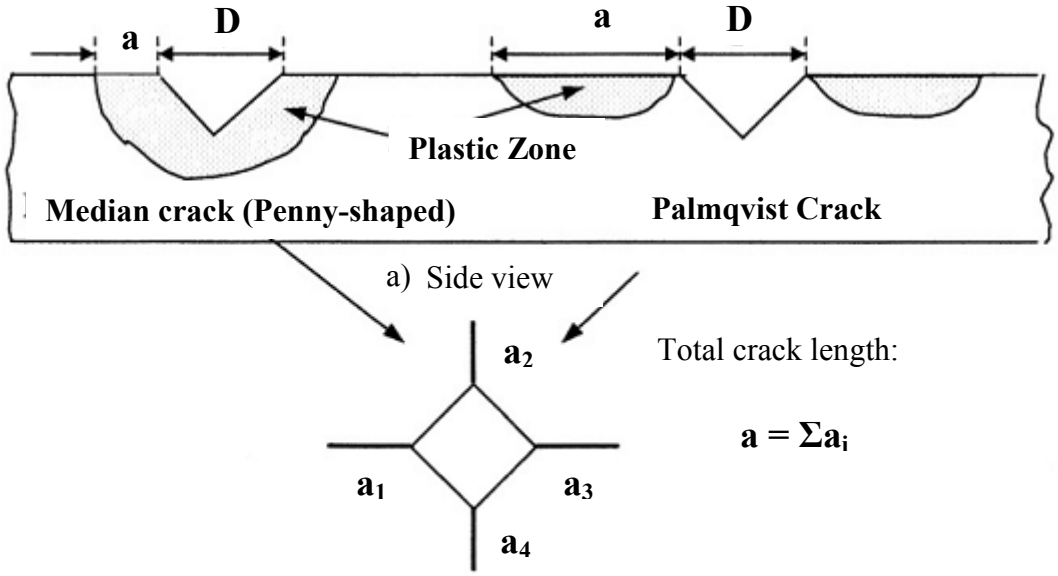

b) Top view showing four cracks

Figure 23: Vickers indenter impression

In Fig. 23 is presented a schematic indentation-induced cracking system [60].

The Vickers hardness H_v was calculated according to the following formula [61]:

Equation 4: Vickers hardness

$$H_v = 0.018187\ P/d^2 (GPa),\ \text{where:} \quad (4)$$

P (N) - the load in N

d (m) - the arithmetic mean of the two diagonals.

The indentation fracture resistance K_R was calculated from the resulting Vickers impression by using the following formula [62]:

Equation 5: Fracture toughness

$$K_R = 0.022\ (E/H_v)^{1/2} \times P/c^{3/2}\ (MPa\ m^{1/2}),\ \text{where} \quad (5)$$

P (N) - the applied load

E (GPa) - the Young's modulus

H_v *(GPa)* - the Vickers hardness,

c (m) - the radial crack length measured from the center of the Vickers impression

0.022 is empirically determined "calibration" constant in ambient air [63].

The Young's modulus values used to calculate K_R were obtained from natural frequency measurements at room temperature [64].

5 x 6 x 45 mm bars were sintered for the measurements of Young's modulus, strength and fracture toughness of $Sc_{0.1}Ce_{0.01}ZrO_2$. First commercially received powders were uniaxially pressed in a steel die at 20 MPa. The samples were subsequently cold isostatically pressed (CIPed) at a pressure of 200 MPa. The bars after uniaxial and cold isostatic pressing were sintered at 1500°C for DKKK and 1600°C for Praxair ceramics. The dwell time during sintering was two hours and 10°C heating/cooling rate was used. The samples were sintered in air. The machining of the chamfered samples to the final 3 x 4 x 45 mm dimension was performed in accordance with the EN 843-1 standard. This test is performed by EMPA, Swiss Federal Laboratories for Materials Testing and Research, Laboratory for High Performance Ceramics, Ueberlandstr. 129, 8600 Duebendorf, Switzerland.

Young's modulus of the material was measured using the natural frequency method using Gindosonic's mk5 machine (Belgium) in accordance with EN 843-2 standard. The sample with a known density was placed over the microphone lining up with the supporting cylinders. The sample was then struck with a small hammer and the mk5 machine recorded the resulting frequency. The test set and procedure for the Young's modulus measurements at elevated temperatures were modified. Firstly, the specimens were hung up and fixed with very fine platinum wires in a small oven. Then a thin ceramic pipe was lined up with the sample and connected outside the oven to the microphone. A 2nd ceramic pipe was placed above the sample with one end outside the oven. Secondly, the sample was heated up with a rate of 15 °C / min in air and after reaching a specific temperature the sample was equilibrated for about 10 min. Finally, the natural frequency of the sample was activated by once hitting it with a small ceramic ball using the 2nd pipe as drop guide. For the measurements during cool down the natural cool down rate of the small oven was used.

Flexural strength was measured with the four-point test method in accordance with EN 843-1 standard. Measurements were performed at 25, 400, 600, 800 and 1000^{o}C. Ten samples were used at each temperature for each composition. Before measurements, the samples were dwelled for 30 minutes at a given temperature in order for them to come to the thermal equilibrium. They were then preloaded by applying a 10 MPa stress and allowed to rest for an additional two minutes. The crosshead speed was set to 1.5 mm/min for all samples.

Fracture toughness was measured using Single Edge V Notch Beam (SEVNB) technique in accordance with CEN/TS 14425-5 standard [65]. A single notch was made on the 3 mm side of the 3 x 4 x 45 mm bar as near to the center as possible with a depth between twenty and forty percent of the total depth of the bar, since it was shown that within this range the depth of the notch has no influence on the K_{Ic} values [65]. A notch making machine was used to ensure the greatest amount of consistency between notches. The machine drove a razor blade to oscillate back and forth across the specimen. The tip of the blade was coated with a diamond paste that varied from a particle size of 10 μm for the course notch to 1 μm for sharpening the notch. The tip radius was monitored so that no specimen had a tip radius large than 5 μm in accordance with CEN/TS 14425-5 standard. Fracture toughness tests were performed at 25, 200, 400, 600, 800 and 1000^{o}C. Three specimens were used at each temperature for each composition. Samples were given minimum of 30 minutes to come to thermal equilibrium. They were then preloaded by applying a 10 N force and allowed to rest for additional two minutes. The crosshead speed was set to 0.1 mm/min for all samples.

Compression tests were performed in a servo-hydraulic test machine (Instron 8500) with a 20 kN load cell. The $Sc_{0.1}Ce_{0.01}ZrO_2$ samples for compression experiments were machined into cylinders 6 mm in diameter and 12 mm in height. The compression load was applied along the sample's maximum dimension and the strain was measured using three strain gauges placed on the lateral faces of the specimen, along the loading direction. The samples were loaded to 700 MPa followed by complete unloading at constant loading/unloading rate of 3 $MPas^{-1}$. The strain was calculated as an average value given by their different strain gauges signals.

Young's modulus test, flexural strength, high temperature fracture toughness test, and compression tests are performed by EMPA, Swiss Federal Laboratories for Materials Testing and Research, Laboratory for High Performance Ceramics, Switzerland.

Scanning Electron Microscopy (ZEISS-SEM) was used for analysis of fracture surfaces of the $Sc_{0.1}Ce_{0.01}ZrO_2$ bars after mechanical tests

CHAPTER 4:
RESULTS AND DISCUSSIONS

All findings collected during the experiments are reported in this chapter. The vibrational properties of $Sc_{0.1}Ce_{0.01}ZrO_2$ are analyzed by Raman spectroscopy and the spectral range of cubic and rhombohedral $Sc_{0.1}Ce_{0.01}ZrO_2$ electrolyte ceramics are collected by 532 nm solid Si and 785 nm NIR lasers. Also, hardness and indentation fracture toughness are reported for both cubic and rhombohedral phase.

In addition, the mechanical properties of $Sc_{0.1}Ce_{0.01}ZrO_2$ electrolytes for intermediate temperature SOFCs are discussed.

4.1 Raman Spectroscopy Analysis and vibrational properties of $Sc_{0.1}Ce_{0.01}ZrO_2$

The whole spectral range of cubic and rhombohedral $Sc_{0.1}Ce_{0.01}ZrO_2$ phases collected using both 532 nm and 785 nm lasers are presented in Fig. 24.

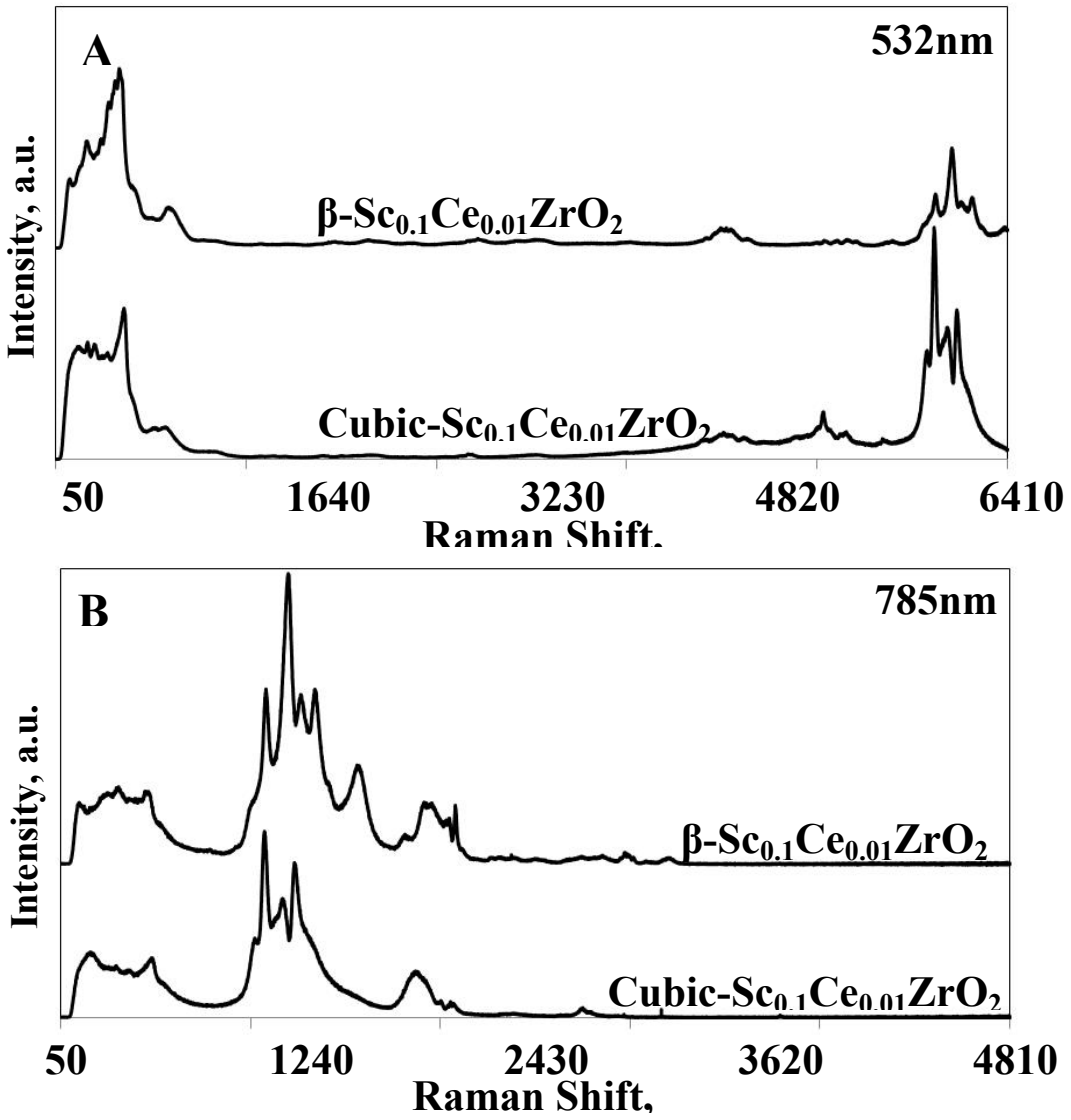

Figure.24: The spectral range of cubic and rhombohedral $Sc_{0.1}Ce_{0.01}ZrO_2$ electrolyte ceramics collected by 532 nm solid Si and 785 nm NIR lasers.

The assignment of the cubic and rhomboherdal phases were made based on the XRD analysis presented elsewhere [21]. While the spectra collected using 532 nm Si laser shows the most prominent features at ranges 100 – 1000 cm^{-1} and 7200 – 8000 cm^{-1} both for cubic and rhombohedral structures, the spectra collected using NIR 785nm laser shows the strongest bands in the 1000 – 2000cm^{-1} range. Thus, it is useful to study the vibrational response of the

$Sc_{0.1}Ce_{0.01}ZrO_2$ using at least two lasers, as the structural information from the analysis of Raman spectra measured with only one laser could be incorrectly interpreted. A number of peaks showing up both in cubic and rhombohedral $Sc_{0.1}Ce_{0.01}ZrO_2$ in 1000-2000 cm^{-1} range using 785nm excitation, are completely missing when 532 nm laser is used, Fig. 24. The bands with a Stokes shift higher than 800 cm^{-1} from the laser excitation line have been previously observed in zirconia based oxides [66,67,68], and bands have been assigned to electronic transitions in impurity ions [69] or to phonon–mediated de–excitation of excited states of the impurity–doped ZrO_2 lattice [70]. While the exact nature of the bands is not obvious, they could be tentatively assigned to the appearance of the luminescence bands related to Ln^{3+} (Ln - Pr^{3+}, Nd^{3+}, Mo^{3+}, Er^{3+}) or other impurities ions [71], and photoluminescence measurements need to be performed to establish the origin of each 1000 cm^{-1} and higher bands.

The spectra of cubic and rhombohedral $Sc_{0.1}Ce_{0.01}ZrO_2$ phases in 100 – 1000 cm^{-1} range taken by 532 nm and 785 nm lasers are presented in Fig. 25. The similar spectrum of cubic $Sc_{0.1}Ce_{0.01}ZrO_2$ cubic electrolyte was published in [72].

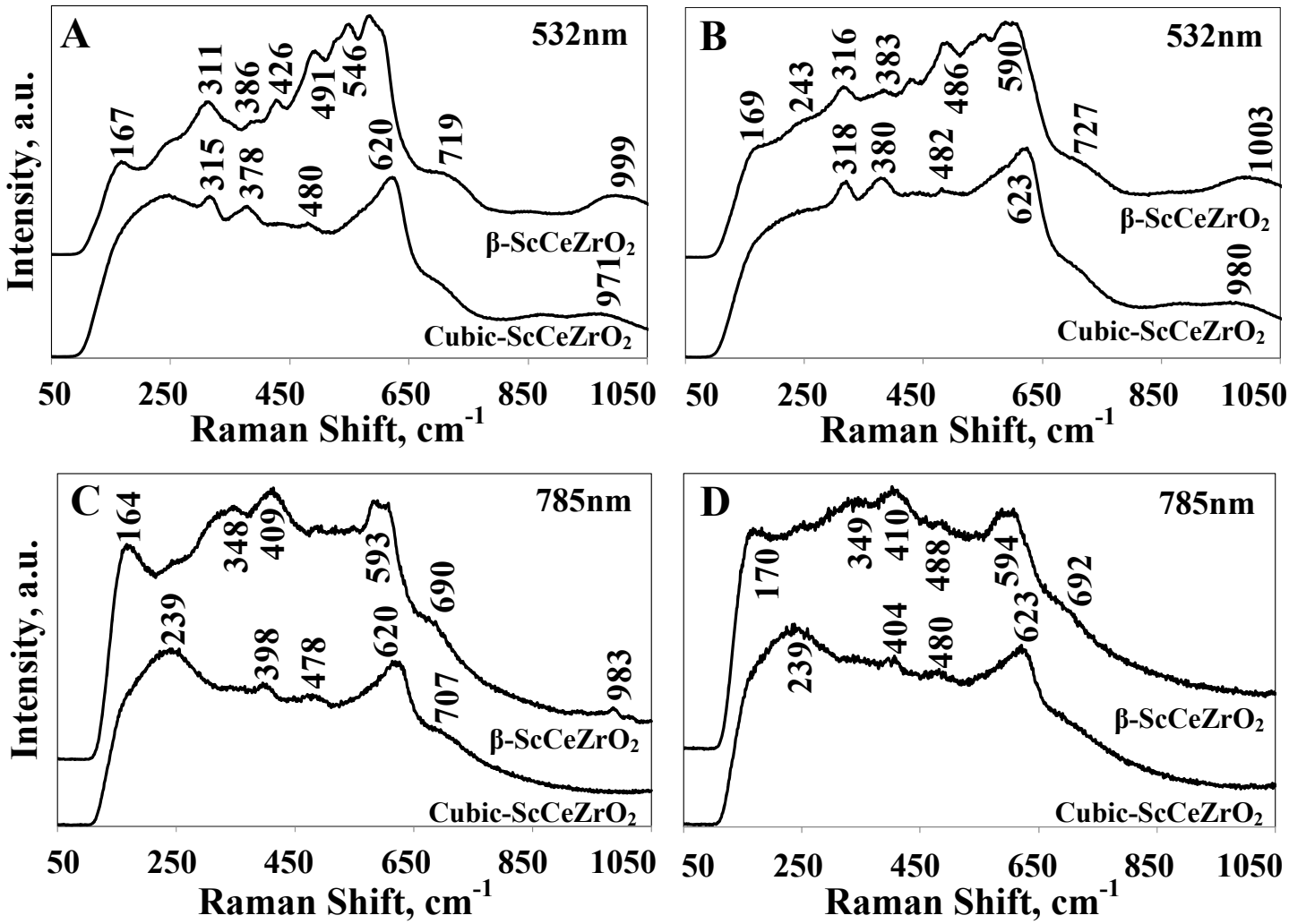

Figure 25: Vibrational spectra of cubic and rhombohedral (β) $Sc_{0.1}Ce_{0.01}ZrO_2$ ceramics; A, C – non-deformed polished surface, B, D – center of Vickers impression

The spectrum of pure cubic fluorite phase should consist of a single F_{2g} mode between 400 – 500 cm^{-1}, and it was reported that Raman spectrum of pure submicron cubic zirconia consists of a weak broad line assigned to a single allowed Raman mode F_{2g} symmetry [24]. The out-of-phase motion of the 2 oxygen atoms is assigned to this mode, therefore the frequency should be independent of the cation mass, and should vary inversely proportional to the square root of the cell volumes. It was reported that in fluorite structures, CeO_2, ThO_2, UO_2 the mode has been

observed near the 460 – 470 cm^{-1} region [25,26]. However, the spectrum of cubic $Sc_{0.1}Ce_{0.01}ZrO_2$ contains a number of bands, and some of the bands at 800 cm^{-1} and below were assigned to Raman active lattice phonons [27,28]. They are located at 239, 478, 480, and 623 cm^{-1} (Fig. 25). At the same time the two bands at 315 and 378 cm^{-1} detected by 532 nm laser were not revealed when spectrum was taken by 785 nm laser, and a band at 398 cm^{-1} was detected by 785 nm laser, but it did not show up in the 532 nm spectrum. Therefore, it is fair to notice that the 315, 378, and 398 cm^{-1} bands do not belong to fluorite lattice vibrations, but might appear due to presence of impurities. The appearance of the peaks, which are not allowed in the cubic fluorite structure, can be also attributed to the disorder of ionic defects in the oxygen sublattice. Substitution of Zr^{4+} by Sc^{3+} results in the formation of high quantities of oxygen vacancies, and such high defect concentration can lead to a violation of the selection rules and allows the appearance of additional modes that are forbidden for the cubic fluorite structure [77].

The possibility of lowering the cubic symmetry on the local scale, which cannot be detected by X–ray diffraction, cannot be excluded, since the oxygen immediately surrounding a vacancy collapse creating structural short range disorder on the oxygen sublattice. It was reported that appearance of the extra peaks, which are not allowed in the cubic fluorite structure,
could indicate a presence of lower symmetry t`-phases, which is difficult to distinguish from cubic structure by X-ray diffraction [53,78].

In order to study the effect of stress on vibrational properties of cubic and rhombohedral $Sc_{0.1}Ce_{0.01}ZrO_2$, the polished surface was indented using Vickers diamond indenter. For

comparison, the spectra taken both from the non-deformed surface and from the center of the Vickers impressions of cubic and rhombohedral -$Sc_{0.1}Ce_{0.01}ZrO_2$ are shown, Fig. 27. While, the position shift and change of the intensities and Full Width at Half Maximum (FWHM) of certain bands can be detected, the structures of cubic and rhombohedral phases remain the same after the deformation by the sharp Vickers indenter. The broadening and decrease of the intensities of the bands after indentation are indicative for increased crystalline disorder, e.g. introduction of internal strain and dislocations along with other defects. However, no stress induced phase transformation with detectable localized changes of structure which change selection rules and cause splitting of vibrational modes can be reported upon indentation.

The differences between the cubic and rhombohedral $Sc_{0.1}Ce_{0.01}ZrO_2$ are clearly visible in Fig. 25, especially when spectra are taken using 532 nm Si laser. As it was already reported in [52] the Raman spectrum of rhombohedral phase is rather complex, presented by a characteristic broad continuum with many small peaks rising above background.

The bands of cubic $Sc_{0.1}Ce_{0.01}ZrO_2$ display anharmonic effects as temperature is raised, with broadening and merging of the peaks [79]. The asymmetry of the 623 cm^{-1} band in Fig. 26, on the left low frequency side of the cubic $Sc_{0.1}Ce_{0.01}ZrO_2$ is typical for disordered systems, as it was indicated by Kosacki [77]. The heating of the cubic $Sc_{0.1}Ce_{0.01}ZrO_2$ up to 1000^{o}C did not remove the asymmetry (Fig. 26), however the intensities of the bands decreased and a significant broadening of the peaks due to anharmonicity, the onset of oxygen diffusion and the increasing dynamic structural disorder of the oxygen sublattice has been observed upon temperature

increase. The weak band at 480cm^{-1}, which could indicate the lowering of the cubic symmetry to tetragonal (t') phase at room temperature [78], completely disappeared upon heating above 500^{o}C. The asymmetric 623 cm^{-1} band is shifted to the lower wavenumbers, as temperature was increased; however bands 315 cm^{-1} and 378 cm^{-1} are shifted to the higher wavenumbers. The position of the first band was located at 315 cm^{-1} at room temperature, but it was shifted to 342 cm^{-1} at 400^{o}C. Due to the broadening, a 315 and 378 cm^{-1} bands coalesced into one broad band starting from 800^{o}C, which was impossible to deconvolute into two peaks. Such shift to the higher wavenumber, upon heating is also indicative that the bands are not due to vibrations of the ions in the fluorite lattice. At the same time, two broad bands in 800-1050 cm^{-1} region completely disappeared at 400-500^{o}C upon heating, but later reappeared when the sample was cooled after heating experiments.

Since the vibrational frequencies of both cubic and rhombohrdral $Sc_{0.1}Ce_{0.01}ZrO_2$ are very complex below 800 cm^{-1} (Fig. 25) they are not suitable for the mapping experiments, which can help to detect the phase transitions or identify the distribution of residual stresses. Therefore, the 1000 – 2000 cm^{-1} range of the spectrum has been chosen for the collection of 2D maps using NIR 785 nm laser. While the origin of the bands is not presently known, however photoluminescence measurements are underway and they will help to identify both the nature of the bands and the nature of the impurities which caused the vibrations. Thought the bands in the 1000 – 2000 cm^{-1} range do not represent the vibrational response of ions in zirconia lattice, they still can be easily used to identify both the presence of the cubic and rhombohedral phases and help detect residual stress existing in the material due to temperature or pressure effects. The

approach is similar to the one used in alumina to detect stresses using well known R-line peak positions which appeared because of the transitions between the ground state of the Cr^{3+} impurity ion and its first excited state, when the material is excited with an citation source such as a laser [80,81].

Fig. 27A represents the typical spectra of cubic and rhombohedral phases. Spectra taken both from the polished surface and from the center of the Vickers impression do not show a significant difference. The deconvoluted peaks of cubic and rhombohedral $Sc_{0.1}Ce_{0.01}ZrO_2$ are shown in Fig. 27B.

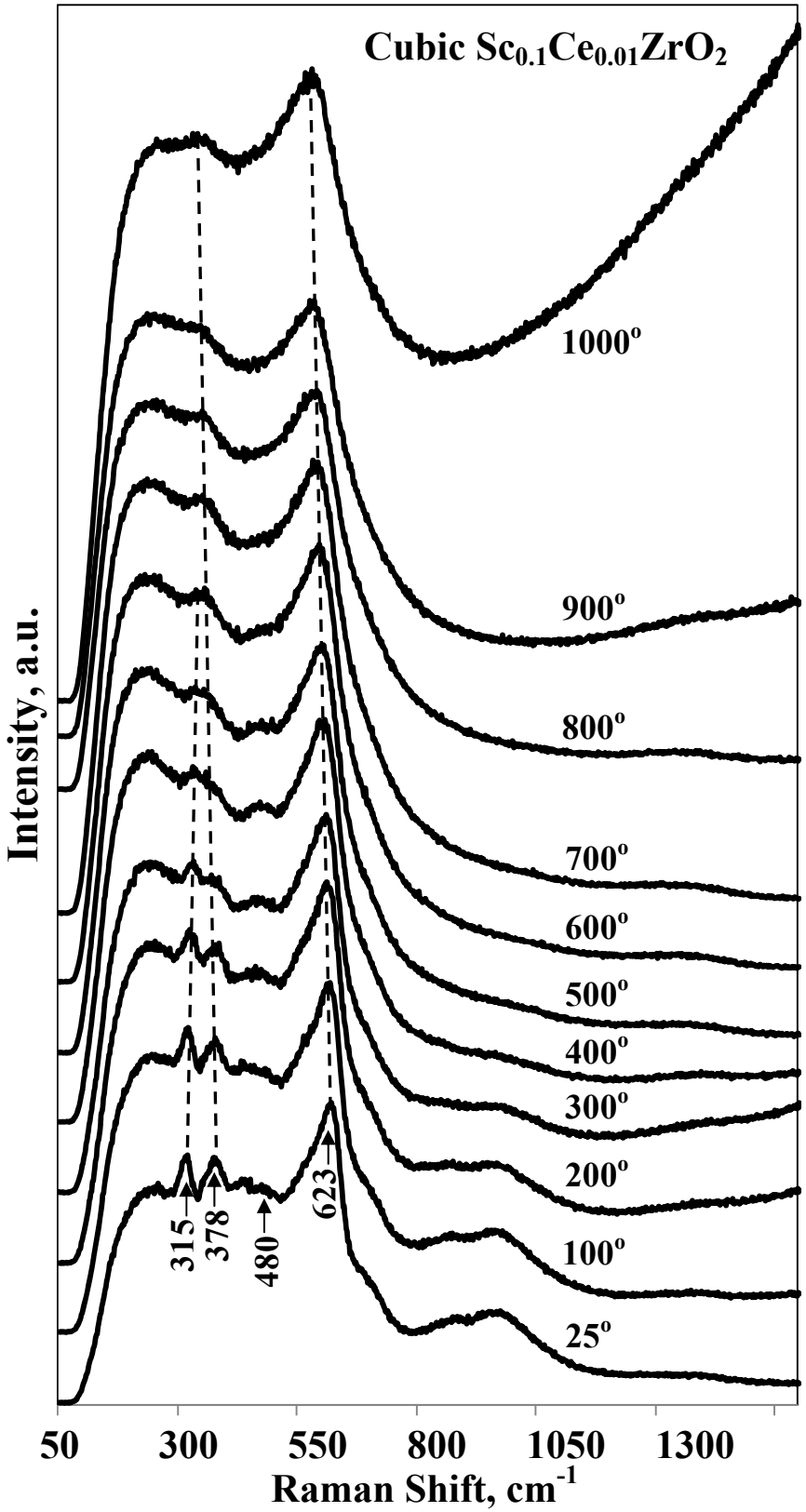

Figure 26: High temperature spectra of cubic of Sc0.1Ce0.01ZrO2 ceramics heated up to 1000°C with 100°C step size and 10°C/min heating rate. A dwell time of 5 minutes was used at each temperature before spectrum's collection

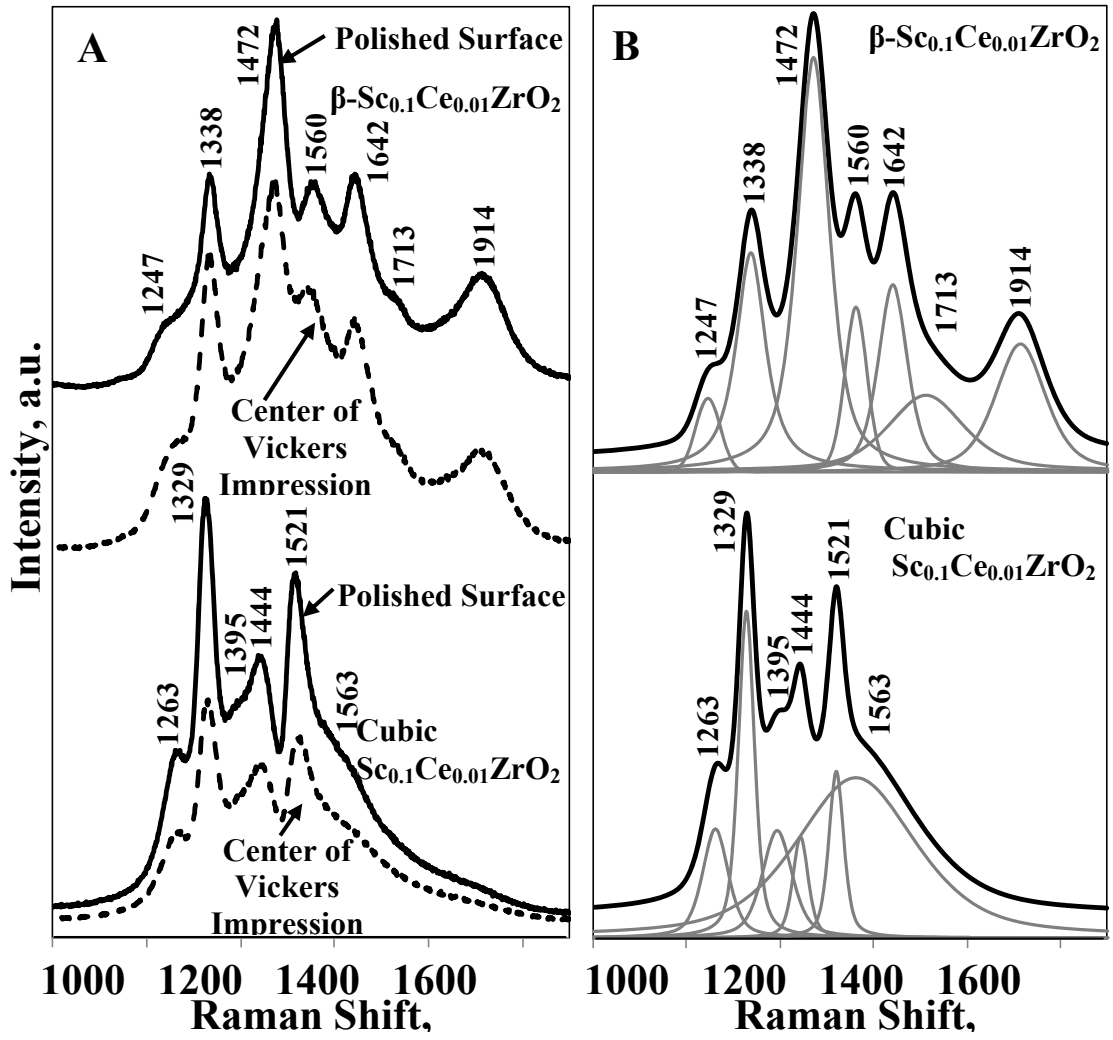

Figure 27: A) Typical spectra of cubic and rhombohedral (β) $Sc_{0.1}Ce_{0.01}ZrO_2$, B) The deconvoluted peaks of cubic and rhombohedral (β) $Sc_{0.1}Ce_{0.01}ZrO_2$.

Confocal optical micrographs of the cubic and rhombohedral $Sc_{0.1}Ce_{0.01}ZrO_2$ are shown in Fig. 28(A, B). While the cubic $Sc_{0.1}Ce_{0.01}ZrO_2$ has a smooth and flat surface, where grain boundaries are clearly visible, the rhombohedral $Sc_{0.1}Ce_{0.01}ZrO_2$ has formed surface termination steps [13]. The formation of the rhombohedral structure has occurred during annealing of the cubic $Sc_{0.1}Ce_{0.01}ZrO_2$ at 375°C for 12 hours which lead to a full transformation from cubic to

rhombohedral phase. The confocal optical micrographs of the Vickers impressions obtained by indenting cubic and rhombohedral $Sc_{0.1}Ce_{0.01}ZrO_2$ are shown in Fig. 29(D, C) total of 20 impressions were made for each sample at a 9.8N load. The impressions were used for the measurements of hardness and indentation fracture toughness. Thus, $H_v = 14.02 \pm 0.3$ GPa and $K_{Ic} = 2.03 \pm 0.7$ MPa·$m^{1/2}$ are reported for cubic $Sc_{0.1}Ce_{0.01}ZrO_2$ and $H_v = 13.78 \pm 0.4$ GPa and $K_{Ic} = 1.68 \pm 0.2$ MPa·$m^{1/2}$ are reported for rhombohedral $Sc_{0.1}Ce_{0.01}ZrO_2$.

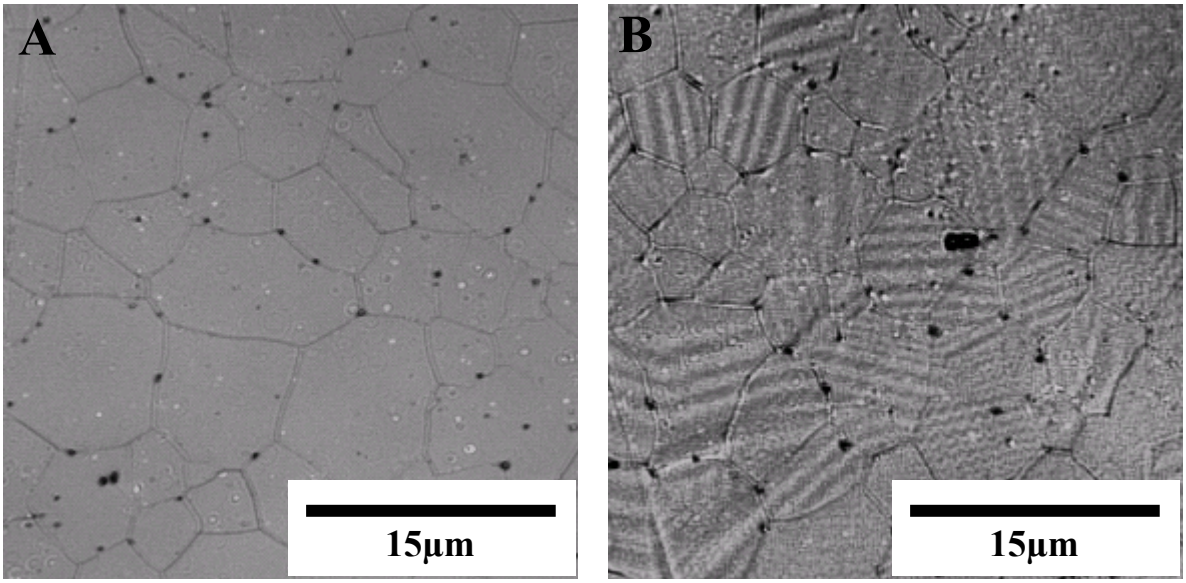

Figure 28: A, B) Confocal images of cubic and rhombohedral (β) $Sc_{0.1}Ce_{0.01}ZrO_2$, ceramics used to determine hardness and indentation fracture toughness

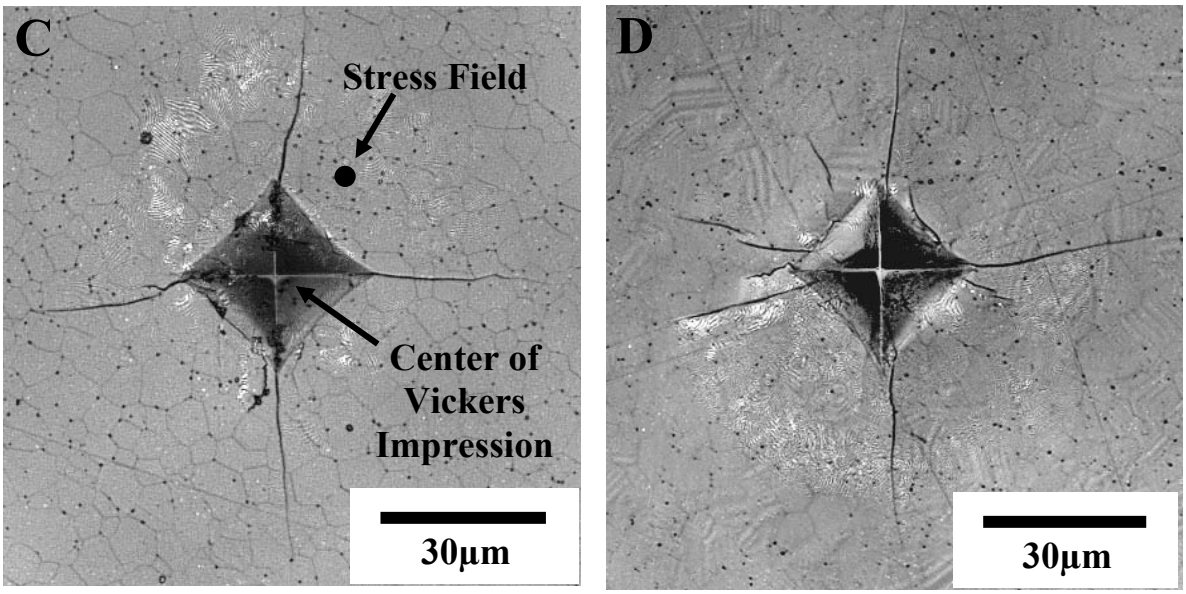

Figure 29: C, D) Confocal optical micrographs of impressions made by a Vickers indenter in C) cubic of $Sc_{0.1}Ce_{0.01}ZrO_2$ and D) rhombohedral (β) $Sc_{0.1}Ce_{0.01}ZrO_2$ ceramics used to determine hardness and indentation fracture toughness, as well as used for mapping experiments.

In order to determine the stability of the cubic and rhombohedral phases in 25 - 400°C temperature range the heating/cooling experiments were performed where spectra in the region of 1240 – 1740 cm^{-1} were collected from three different locations on the sample's surface during heating and cooling. Three different samples of cubic $Sc_{0.1}Ce_{0.01}ZrO_2$ and three different samples of rhombohedral $Sc_{0.1}Ce_{0.01}ZrO_2$ were indented using a Vickers indenter at 9.8 N. For each indented sample, a separate location has been chosen: a) a non-deformed polished surface far away from the impression; b) a center of the Vickers impression; c) a location close to the Vickers impression where a stress should develop due to a deformation introduced by indentation. The last two locations, a center of the Vickers impression and a stress field point, are shown in Fig. 29C.

The spectra collected from three different locations in cubic and rhombohedral phases during heating and cooling up to 400°C are presented in Fig. 30. It was detected that while cubic phase is retained as cubic on the polished non-deformed surface for the performed heating experiment, it would transform to a rhombohedral structure upon cooling in the center of the Vickers impression, where the mixture of cubic and rhombohedral phases could be detected at room temperature after cooling (Fig. 30A). However, at the stress field (approximate location is shown with a black dot in Fig. 29C.) a full transformation from the cubic to rhombohedral phase would occur, thus only the spectrum of rhombohedral phase can be found and no cubic phase can be detected after cooling. At the same time, it was found that the rhombohedral phase is stable in the whole 25 - 400^{o}C temperature range at all three locations both upon heating and cooling conditions (Fig. 30B).

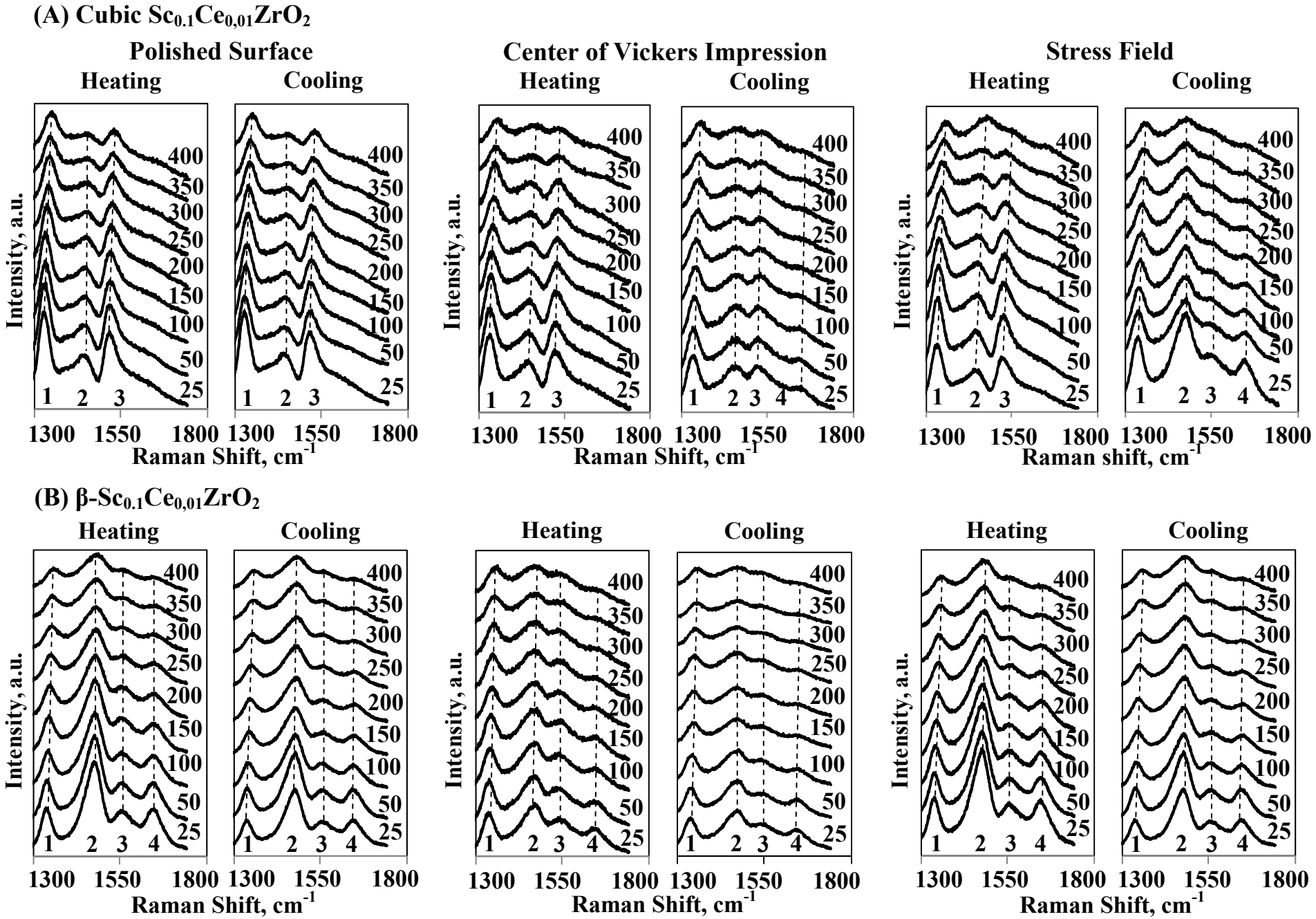

Figure 30: Spectra of cubic (A) and rhombohedral (B) Sc0.1Ce0.01ZrO2 during heating and cooling up to 400oC.

The position of the peaks of cubic and rhombohedral phases was analyzed as a function of the locations and temperature (Fig. 31). While the positions of 1329 cm^{-1} peak, of the cubic phase collected from the center of the Vickers impression and the stress field, with the same tendency observed for 1521 cm^{-1}, were shifted to the higher wavenumbers relative to the peak positions collected from the polished, non-deformed surface (Fig. 31A), the opposite tendency was detected to occur for some of the peaks of the rhombohedral phase (Fig. 31B). Thus, 1472 cm^{-1} peaks of the rhombohedral phase were shifted to the lower wavenumbers by ~10–15 cm^{-1} relative to their positions at the polished and stress field surfaces, while 1338 cm^{-1} peak of rhombohedral phase hardly showed any shift in position. This difference can be clearly seen when 2D maps of the peak positions were created with Vickers impression made in cubic and rhombohedral phases (Fig. 32 & 33). The 2D peak position maps of 1329, 1444, and 1521 cm^{-1} peaks of the cubic $Sc_{0.1}Ce_{0.01}ZrO_2$ along with the representative spectra taken from the location of interest are shown in Fig. 32. The Raman micrographs of the Vickers impression, created by mapping positions of the 1329 and 1521 cm^{-1} peaks give an indication of where the impression is located and what is the shift of the peaks depending on the location. However, the 1444 cm^{-1} peak shows a homogeneous distribution of the peak position in the region of interest, therefore it is not stress/strain sensitive. The position of the 1329 and 1521 cm^{-1} peaks of the cubic phase shifted to the higher wavenumbers in the center of the Vickers impression, as indicated in Fig. 32. At the same time the 2D peaks position maps created using 1338, 1472, 1560, and 1642 cm^{-1} peaks of the rhombohedral $Sc_{0.1}Ce_{0.01}ZrO_2$ showed that the shift to the lower wavenumbers occurred in the center of the Vickers impression for all four peaks (Fig. 33).

3D map of the peak position created with Vickers impression made in cubic and rhomboherdal phases is other way to observe the difference in the shift in position of the peaks (Fig. 34).

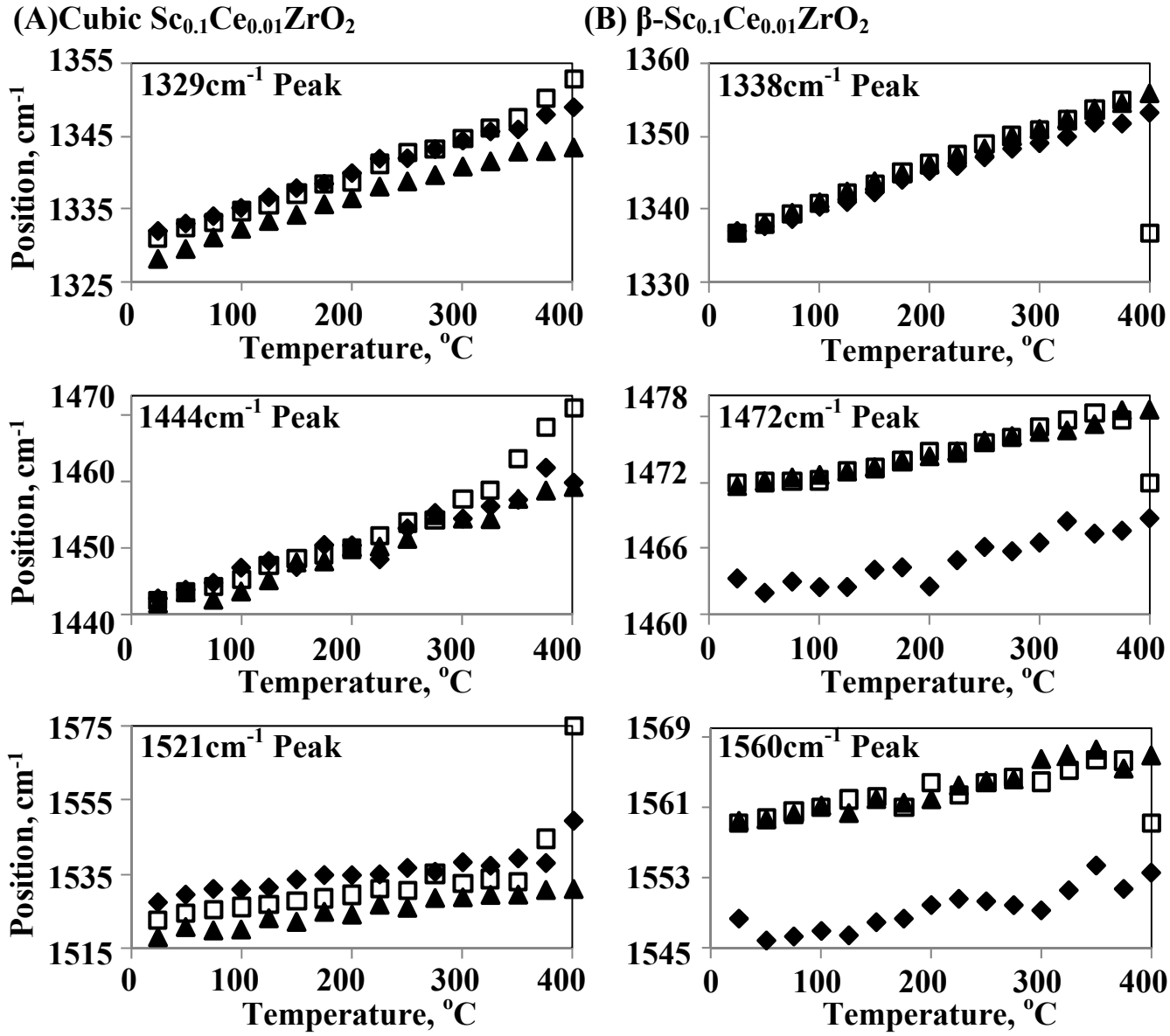

Figure 31: Position of the peaks of cubic (A) and rhombohedral (β) phases (B) vs. temperature upon heating experiments; ▲ - Polished surface,
◆ - Center of Vickers impression,
□ - Stress field.

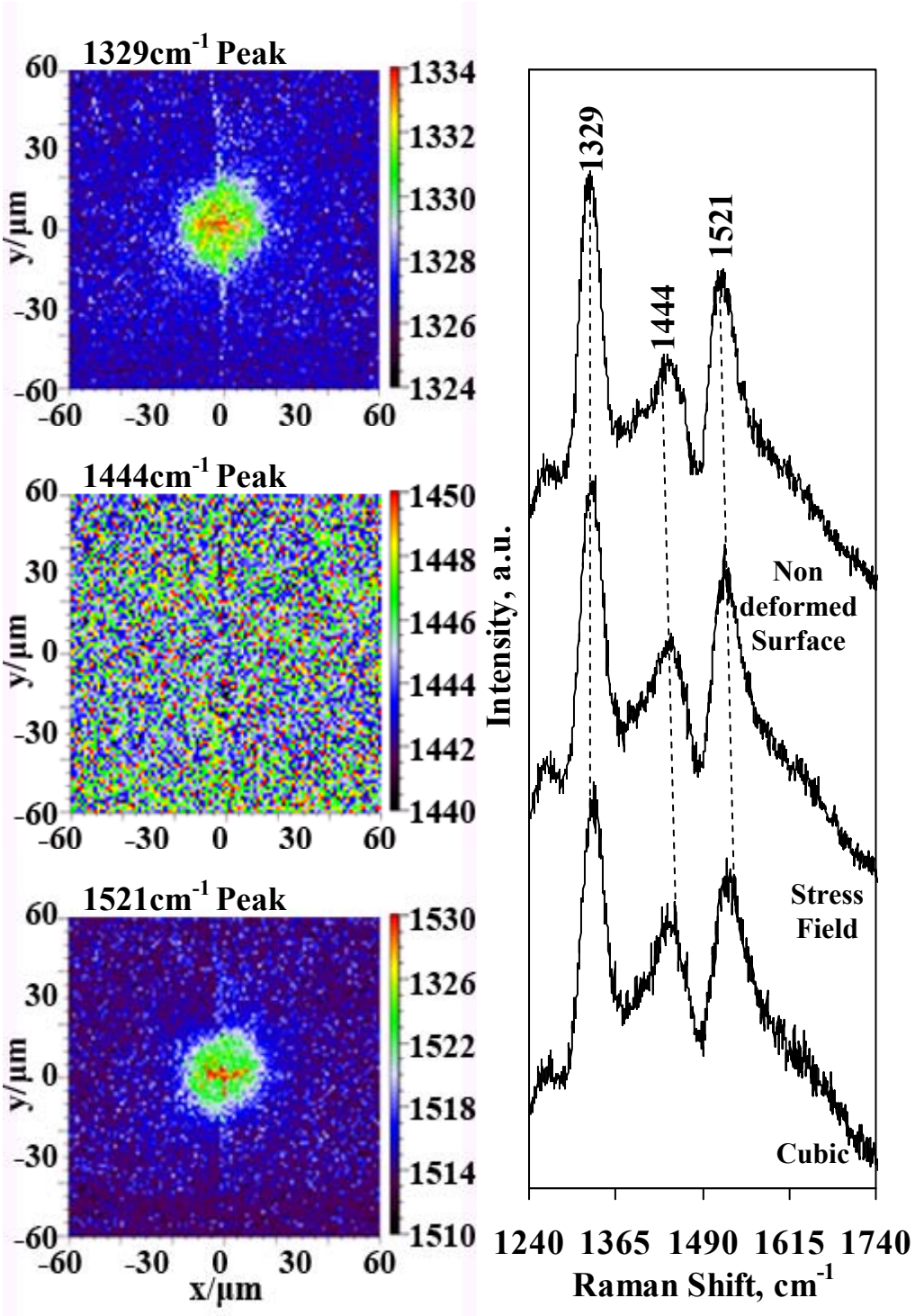

Figure 32: 2D maps of the peak positions for cubic phase of $Sc_{0.1}Ce_{0.01}ZrO_{2.}$

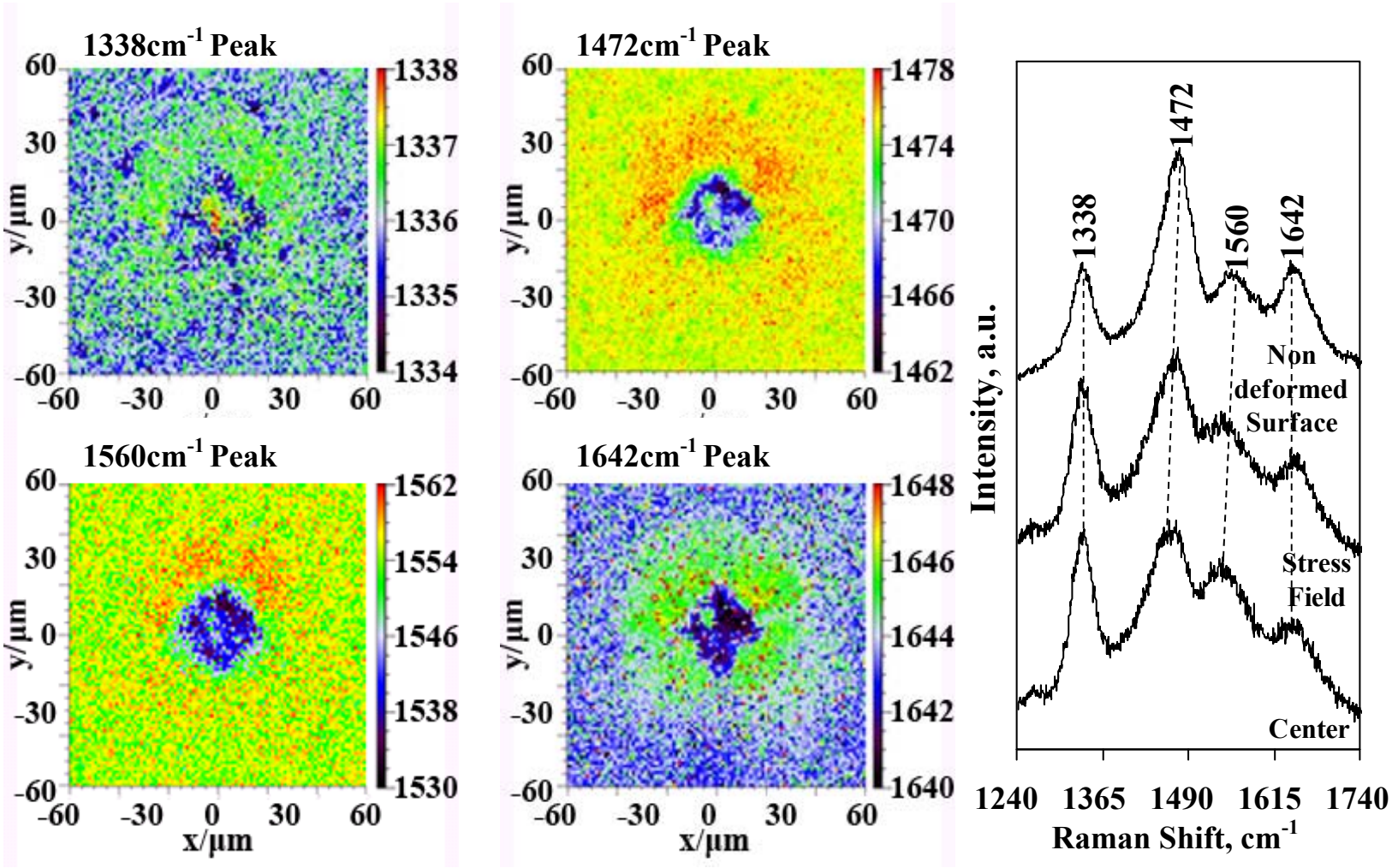

Figure 33: 2D maps of the peak positions for rhombohedral phase of $Sc_{0.1}Ce_{0.01}ZrO_2$.

3D maps are collected using ~1521cm^{-1} cubic and ~1472cm^{-1} rhombohedral peak positions as a function of the specimen' surface. The high residual compressive stresses created inside the impression upon indentation caused the shift of the ~1521cm^{-1} peak to the higher wavenumbers in the cubic phase with the maximum ~15cm^{-1} shift observed in the center of the Vickers impression (Fig. 34A). On the opposite, the ~1472cm^{-1} peak position was shifted to the lower wavenumber upon indentation in the β-phase. The maximum of ~10cm^{-1} shift was observed with a change from ~1472cm^{-1} for the non-deformed surface to ~1462cm^{-1} for the center of the impression (fig. 34B).

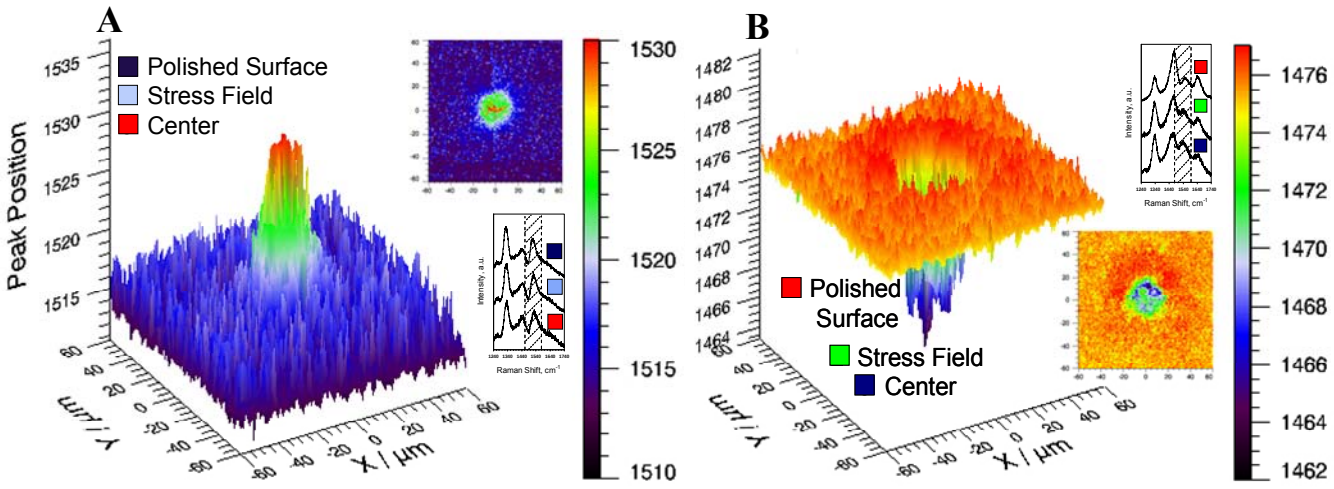

Figure 34: 3D maps of Vickers impression and deformation zone of cubic (A) and rhombohedral (B) phase

The reason of the shifts to the lower wavenumbers can lie in a different response to the compressive stress of the rhombohedral phase, but it could also be explained by a different response of the particular vibrations under consideration. To explain the differences, the unaxial

stress/strain calibration experiment, for both cubic and rhombohedral phases, are required that will be performed in the future.

After heating/cooling experiments of the cubic phase in 20-400°C temperature range (Fig. 30) it became clear that not only temperature, but also existing stress affects the phase composition of $Sc_{0.1}Ce_{0.01}ZrO_2$. Fig. 35A shows the confocal optical micrograph of the impression after heating/cooling to 400^{o}C experiment of the indented cubic $Sc_{0.1}Ce_{0.01}ZrO_2$. The deformation zones formed around impression are clearly visible. This impression was used for mapping (Fig. 4.9B) which shows formation of the rhombohedral phase in the stressed fields around the impression after heating/cooling. The impression map was created using the area of 180x180 μm of the impression, presented in Fig. 4.9A. The typical spectra, corresponding to cubic, rhombohedral and a mixture of two phases, collected from the different locations on the maps are given in Fig. 4.9B. As one can see from the map (Fig. 4.9C), the cubic phase was mostly retained both further away outside of the deformation zone at the polished surface and inside of the Vickers impression after heating/cooling, however the cubic to rhombohedral phase transformation has occurred inside of the stress field. The 1D line map of the ~1460 cm^{-1} peak position along the *x* axis from A to B shown in Fig. 4.9D. It shows that the peak position of the cubic phase inside the Vickers impression has shifted to the higher wave numbers relative to the non-deformed cubic phase which is located outside of the impression. The separate zones, containing either almost pure cubic or rhombohedral phase or a mixture of cubic and rhombohedral phases, are highlighted with relevant dashed lines.

A cubic phase was found outside the Vickers impression and deformation zone surrounding impression, a rhombohedral phase was mostly found within a deformation zone, and a mixture of cubic and rhombohedral phases was found within the impression, but also in the narrow interval at the outside area of the deformation zone (Fig. 4.9D).

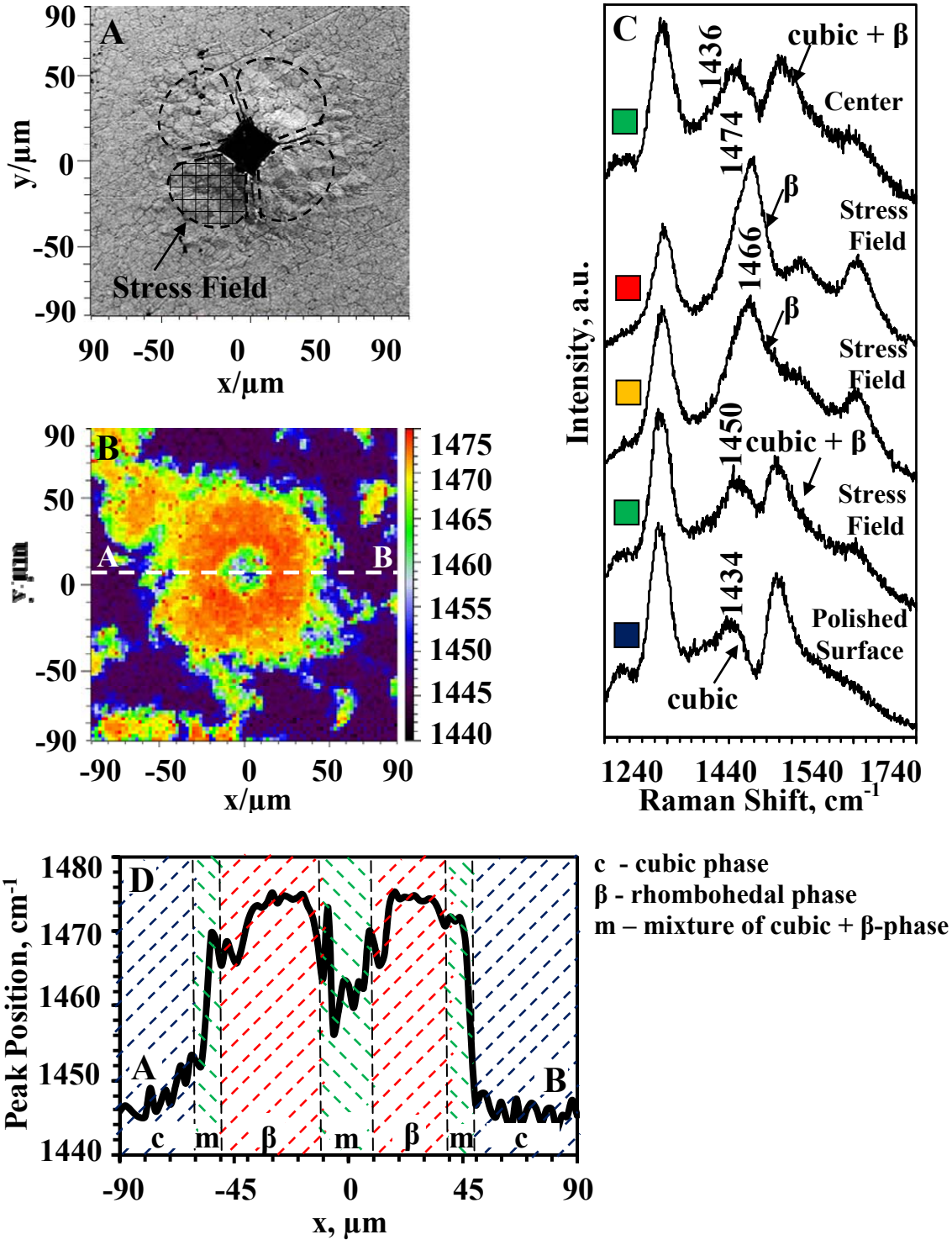

Figure 35: A) Confocal micrograph of Vickers impression in cubic $Sc_{0.1}Ce_{0.01}ZrO_2$ phase after 400°C heating/cooling. The Vickers impression was placed before heating/cooling.
B) 2D maps of 1434 – 1474 cm^{-1} peak position of the selected area with the Vickers impression and deformation zones corresponding to the micrograph from Fig. 32;
C) Typical spectra corresponding to cubic, cubic + rhombohedral (β), and pure rhombohedral (β)phases from three different locations of the map presented in 33;
D) 1D map of the 1430 – 1480 cm^{-1} peak position collected along x-axis at the intersection with 0 of *y*-axis along AB line

4.2 Mechanical properties of $Sc_{0.1}Ce_{0.01}ZrO_2$ ceramics

4.2.1. Stability, lattice parameters, and densities of the cubic and rhombohedral $Sc_{0.1}Ce_{0.01}ZrO_2$

The cubic phase is a metastable phase in $Sc_{0.1}Ce_{0.01}ZrO_2$ at room temperature [21] owing its existence to the relatively fast cooling of the ceramic from the sintering temperature. It should be noted that at 700 – 800°C, which are SOFC operating temperatures, the cubic phase is stable and will not transform to any other phase degrading SOFC performance. However for the applications at lower temperatures, especially in around 400°C region, the cubic phase will eventually transform to the thermodynamically more stable rhombohedral phase [82,51]. The measured lattice parameter *a* is almost identical for DKKK and Praxair materials and is equal to 5.09119(7) Å and 5.09203(7) Å, respectively [83]. Using these lattice parameters, the theoretical density of DKKK and Praxair ceramics equals to 5.827 g/cm^3 and 5.845 g/cm^3, respectively. In order to fully convert cubic $Sc_{0.1}Ce_{0.01}ZrO_2$ to the rhombohedral phase, as sintered cubic $Sc_{0.1}Ce_{0.01}ZrO_2$ ceramics were annealed at 400°C for 12 hours. After the heat treatment, only rhombohedral phase has been detected at room temperature with about 3% of *c* phase and a very small amount of $8ZrO_2{\cdot}2Sc_2O_3$ are still present [84]. The calculated lattice parameter of β-phase are *a*=3.56596(3) Å and *c*=9.00992(1) Å, space group $R\bar{3}$ (#148). Theoretical density of β-phase calculated from lattice parameters is 5.721 g/cm^3 and is slightly lower than that of the cubic phase.

4.2.2 Young's modulus of cubic and rhombohedral $Sc_{0.1}Ce_{0.01}ZrO_2$

The room temperature Young's modulus, measured by the ultrasonic technique was found to be equal to 217.67 ± 0.61 GPa and 188.23 ± 2.81 GPa for cubic DKKK ceramics sintered at 1500°C and Praxair ceramics sintered at 1600°C, respectively. Young's modulus of cubic yttria stabilized ZrO_2 was reported to be 220 GPa [83], which lines up almost identically with E values of DKKK $Sc_{0.1}Ce_{0.01}ZrO_2$. The lower Young's modulus of Praxair ceramics can be explained by higher porosity of this ceramic. The Young's modulus of annealed rhombohedral $Sc_{0.1}Ce_{0.01}ZrO_2$ was measured to be 211.07 ± 3.28 GPa at RT. This measurement was provided by EMPA, Swiss Federal Laboratories for Materials Testing and Research, Laboratory for High Performance Ceramics, Ueberlandstr. 129, 8600 Duebendorf, Switzerland. The measured Young's modulus values were used for calculation of the indentation fracture resistance of the DKKK and Praxair ceramics.

Out of the experiment completed by EMPA it has been concluded the Young's modulus of cubic Sc_2O_3-$Ce0_2$-ZrO_2 DKKK ceramics exhibit insignificant softening as temperature increase from room temperature to 200°C (Fig. 10A). Sc_2O_3-CeO_2-ZrO_2 exhibit a significant mechanical damping in the 300°C – 450°C temperature range with a simultaneous decrease in Young's modulus values [85]. Because of the high damping the measurements of Young's modulus at 300°C and 400°C were not possible to perform by the impulse excitation technique. A significant softening of the cubic phase has occurred at 500°C and Young's modulus values decreases to 102.07 ± 0.47 GPa at this temperature. As temperature increased further, Young's modulus of $ScCeZrO_2$ increased from 102.07 ± 0.47 GPa at 500°C to 171.01 ± 0.79 GPa at 1000°C. Similar

trend was observed for the elastic behavior cubic $ScCeZrO_2$ produced using Praxair powders (Fig. 36A). A non significant softening from 211.07 ± 3.28 GPa at room temperature to 186.95 ± 0.82 GPa at 400^{o}C had been observed for the rhombohedral $ScCeZrO_2$ (Fig. 36B). Since the rhombohedral phase is stable up to 400^{o}C, and upon further increase in temperature will transform to the cubic phase [83], the measurements performed at 500^{o}C shows the property of the cubic $ScCeZrO_2$. The Young's modulus of the rhombohedral phase at 500^{o}C has a value of 99 GPa which is almost twice as low as the Young's modulus of rhombohedral phase at 400^o, but corresponded well for the elastic modulus of the cubic phase at 500^{o}C (Fig. 36A).

4.2.3. Hardness and indentation fracture resistance

The hardness and fracture resistance of cubic and rhombohedral $Sc_{0.1}Ce_{0.01}ZrO_2$ DKKK ceramics as a function of indentation load is presented in Fig. 37. While the rhombohedral $Sc_{0.1}Ce_{0.01}ZrO_2$ exhibit indentation size effect, where the hardness values decreases from 16.13 ± 0.76 GPa at 0.25 N load to 14.39 ± 0.25 GPa at a load of 50 N (Fig. 37B), the cubic phase does not show the increase of the hardness at small loads (Fig. 37A). Indentation fracture resistance increases as the load increases. It should be noted, that at small loads, such as 0.25N, 0.50N, 1.00N the cracks were originated not from all corners of impression, but about 25% of all corners resulted in crack formation.

The typical defect, which served as a fracture origin of the DKKK ceramics tested at RT is shown in Fig. 38.

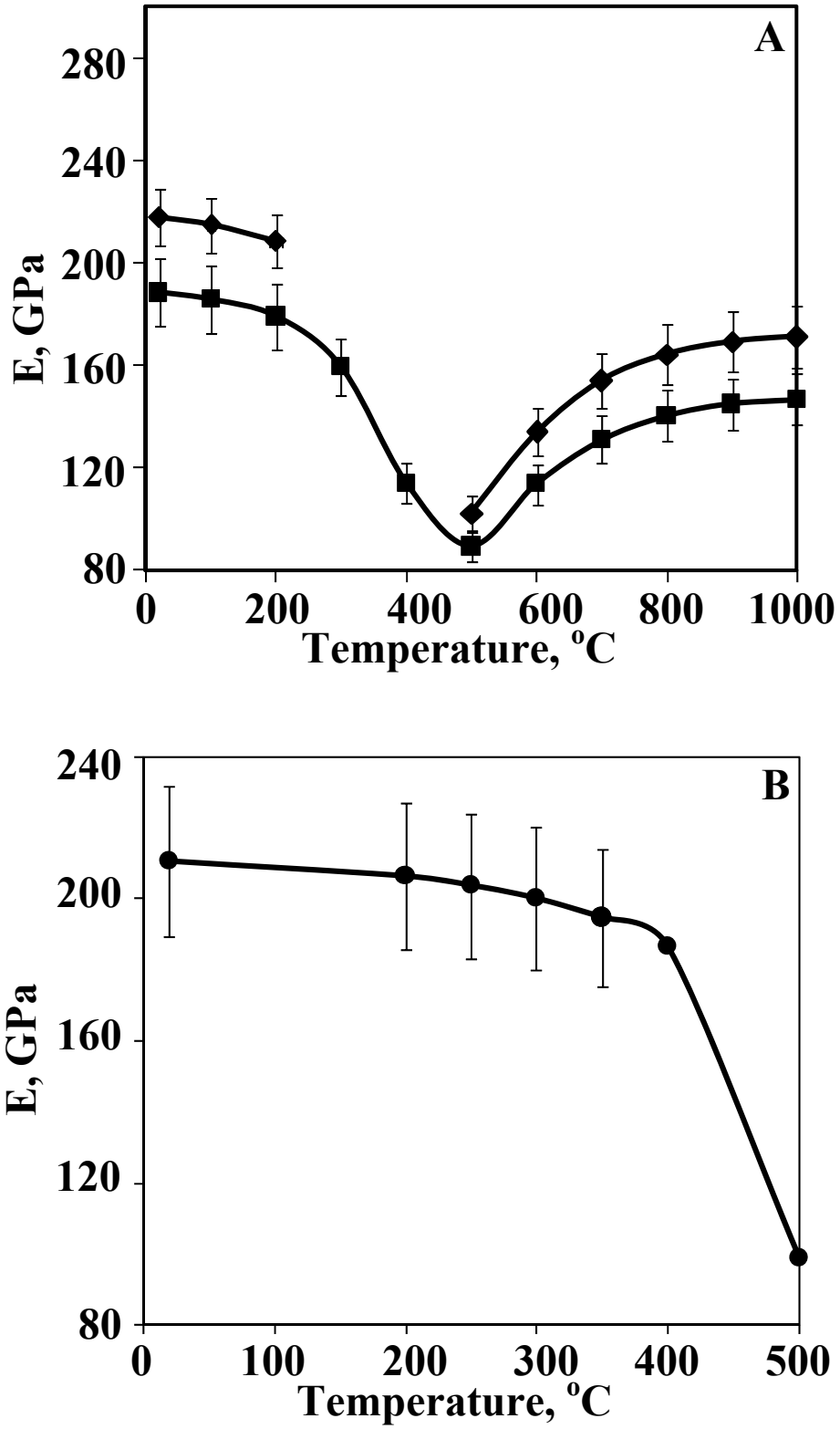

Figure 36: Young's modulus vs. temperature of (A) the cubic phase sintered from Praxair (■) and DKKK (◆) powders, and (B) the rhombohedral DKKK (●) $Sc_{0.1}Ce_{0.01}ZrO_2$ ceramics.

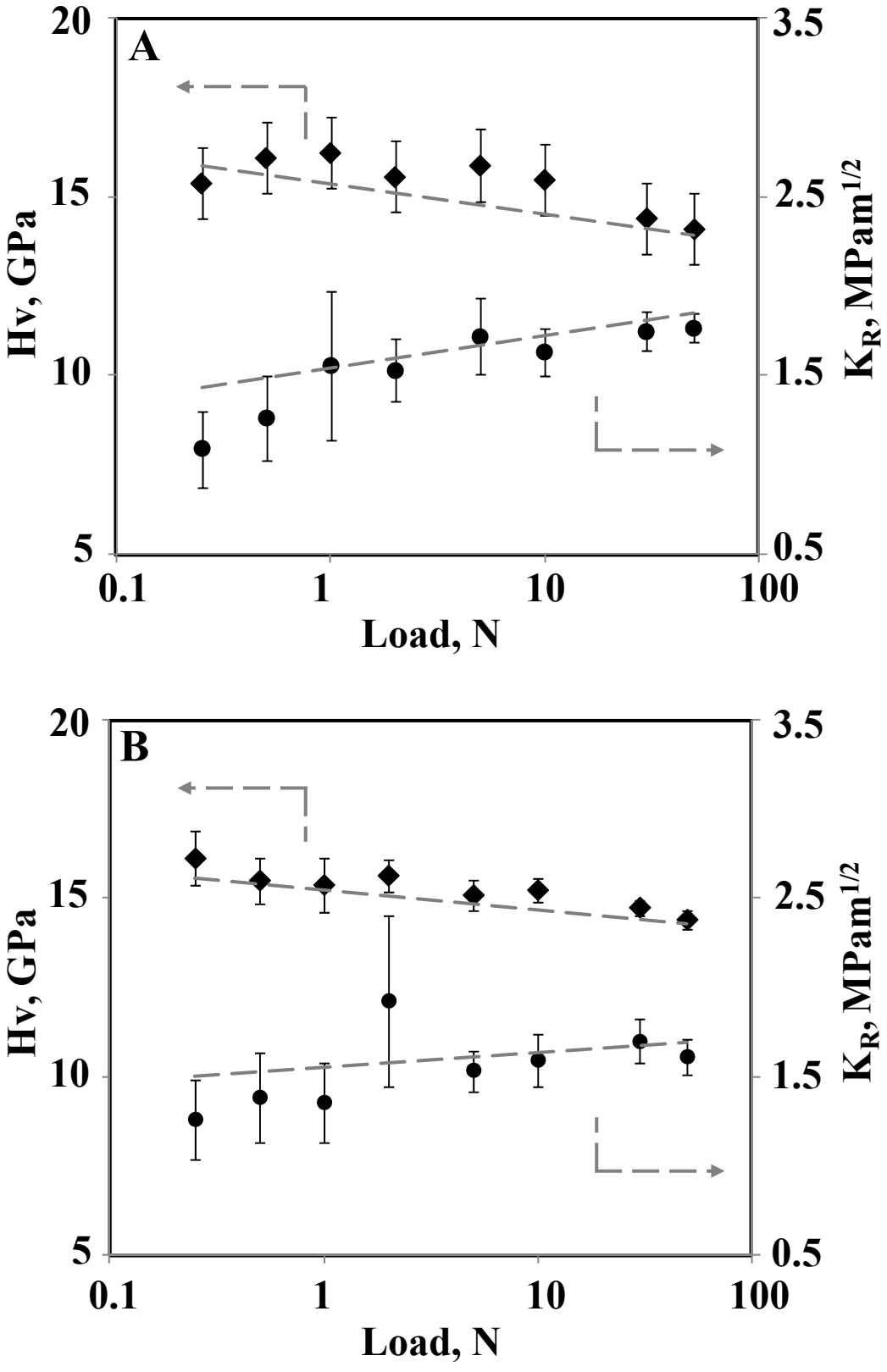

Figure 37: Hardness (—◆—) and indentation fracture resistance (—●—) of cubic (A) and rhombohedral (B) $Sc_{0.1}Ce_{0.01}ZrO_2$.

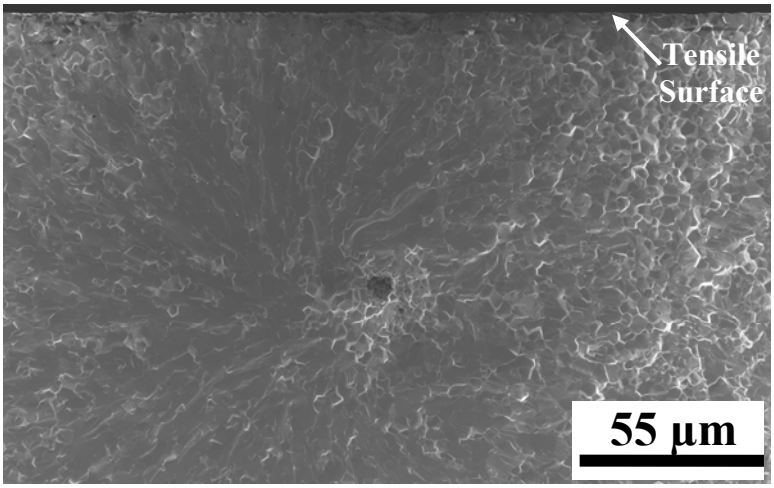

Figure 38: A pore as a fracture origin of DKKK $Sc_{0.1}Ce_{0.01}ZrO_2$ ceramics tested at RT and 800°C

4.2.4. Strength and fracture toughness

EMPA, Swiss Federal Laboratories for Materials Testing and Research, Laboratory for High Performance Ceramics, Switzerland, measured the flexural strength at room and elevated temperatures using the four point test method in accordance with European standard EN 843-1.

The strength measurements of the cubic DKKK $Sc_{0.1}Ce_{0.01}ZrO_2$ ceramics at room temperature resulted in value of 201.29 ± 39.7 MPa , and it decreased to 170.10 ± 10.96 MPa at 1000°C. On another side, Praxair ceramics has RT strength of 78.54 ± 7.53 MPa, which decreases to 59.53 ± 6.77 MPa at 400°C and remains in the 50 – 60 MPa range at higher temperature measurements. Such decrease in strength in comparison with DKKK ceramics could be explained by the presence of very inhomogeneous areas in sintered Praxair ceramics, with some of the areas being very porous and other being more dense. At the same time the significant amount of the exaggerated grains could be also detected giving a bimodal grain size distribution and definitely affecting the strength of $Sc_{0.1}Ce_{0.01}ZrO_2$ Praxair ceramics (Fig. 39).

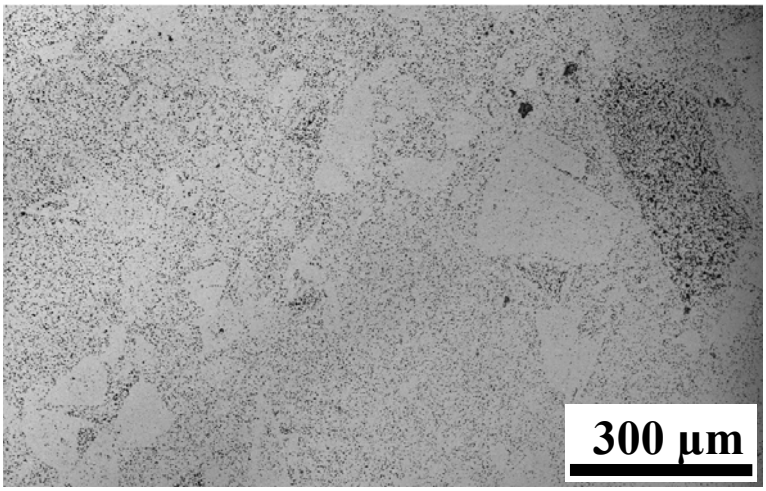

Figure 39: The polished surface of Praxair Sc0.1Ce0.01ZrO2 ceramics sintered at 1600oC showing the presence of the non homogeneous microstructure and porosity.

The fracture toughness of two ceramics as a function of temperature, also have been provided by EMPA, Switzerland. It has been found the room temperature K_{Ic} of cubic DKKK $Sc_{0.1}Ce_{0.01}ZrO_2$ ceramics is equal to 2.09 ± 0.09 MPa·$m^{1/2}$ and it increases at 300°C to 2.44 ± 0.33 MPa·$m^{1/2}$, followed by a decrease to 1.26 ± 0.08 MPa·$m^{1/2}$ at 500°C. The further slight increase to 1.68 ± 0.29 MPa·$m^{1/2}$ occurs as the temperature increases to 1000°C. The increase of the fracture toughness temperature range could be explained by ordering/clustering of oxygen vacancies around the Sc^{3+} dopant cations which were reported to happen at ~ 300°C. This ordering/clustering process causes the appearance of the loss peak, the appearance of which shows that there is energy absorbing process occurring at these temperatures [84,86,87,88]. Since the cubic to rhombohedral phase transition occur at 300 – 400°C during long annealing time up to 12 hours at these temperatures, the reported vacancies ordering phenomenon might be a beginning of the phase transition in $Sc_{0.1}Ce_{0.01}ZrO_2$. The decrease of K_{Ic} at 500°C can be explained by a significant softening of the lattice and decrease of Young's modulus at this

temperature. The second slight increase in K_{Ic} at 900 – 1000°C can be explained by the deviation of the oxygen content from its stoichiometric values because oxygen is leaving the crystal lattice creating more vacancies. Such increase of non-stoichiometry leads to the formation of the repulsive forces between cations in the lattice, which, in turns can contribute to the increase in K_{Ic}. The fracture toughness of $Sc_{0.1}Ce_{0.01}ZrO_2$ Praxair ceramics was measured to be lower than K_{Ic} of ceramics made of DKKK powders, partly due to lower Young's modulus of this ceramics. Small decrease in K_{Ic} of Praxair ceramics from 1.52 ± 0.01 MPa·$m^{1/2}$ at 200°C and 300°C to ~1 MPa·$m^{1/2}$ at 400°C and higher temperatures is reported. The decrease happens in the same temperature range as in case of DKKK ceramics.

According to the EMPA, Switzerland, the strength of rhombohedral $Sc_{0.1}Ce_{0.01}ZrO_2$ was slightly higher than those of cubic phase at room temperature and it increased from 233.08 ± 32.01 MPa at RT to 271.80 ± 91.96 MPa when tested at 400°C. One would expect that fracture toughness of rhombohedral phase would be also higher than those of cubic phase, but in fact K_{Ic} of rhombohedral phase was lower than cubic phase at RT, and it increased from 1.87 ± 0.05 MPa$m^{1/2}$ at RT to 2.47 ± 0.17 MPa$m^{1/2}$ at 400°C. Such low values of fracture toughness of rhombohedral $Sc_{0.1}Ce_{0.01}ZrO_2$ are indicative that no significant toughening mechanism is active during the deformation of this material despite its rather highly defective microstructure [83].

The fracture surfaces of DKKK ceramics after K_{Ic} tests at RT and 1000°C are shown in Fig. 40. While fracture surface shows fully transgranular mode of failure after testing at RT (Fig. 40A), the high percentage (~ 50%) of intergranular fracture appears after tests performed at 1000°C (Fig. 40B).

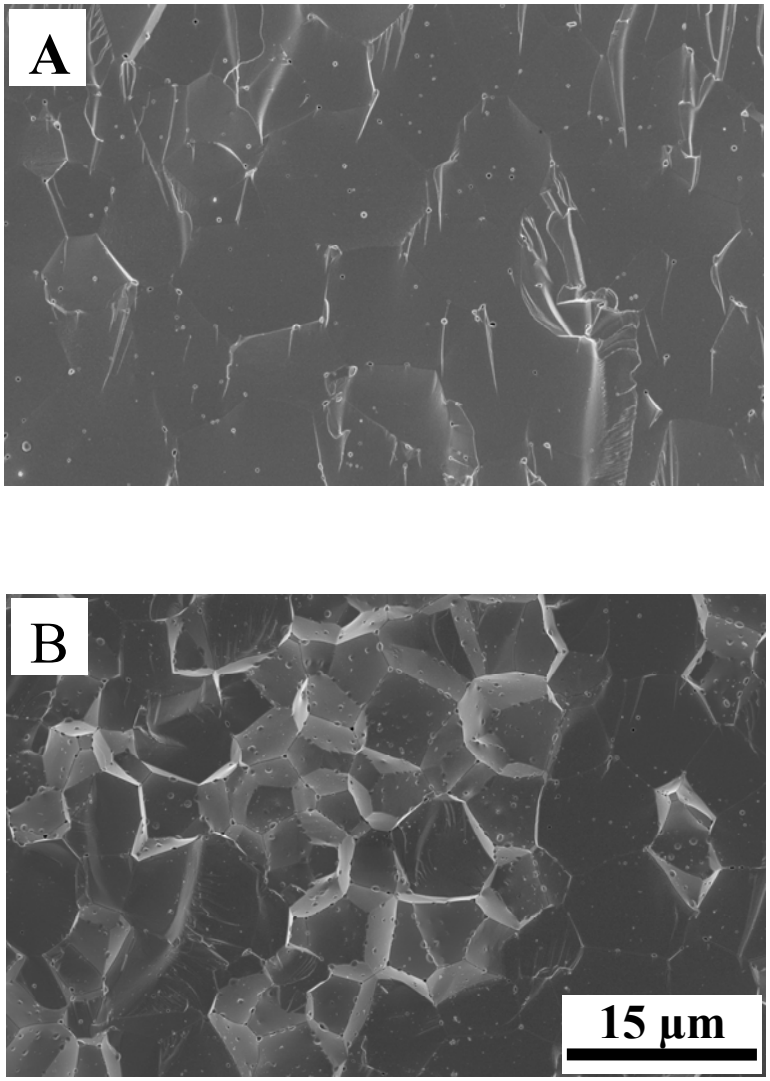

Figure 40: Fracture surface of DKKK $Sc_{0.1}Ce_{0.01}ZrO_2$ ceramics after K_{Ic} measurement at RT (A) and 1000°C (B).

The intergranular fracture also appears for the samples tested at 800°C and 900°C, but percentage of the intergranular fracture decreases as temperature of test decrease. The intergranular fracture cannot be detected in DKKK ceramics tested at 600°C or lower temperatures, when only fully transgranular fracture surfaces are observed. Considering that the vacancies start to appear at 700 – 800°C and their amount significantly increases at 900°C and 1000°C, the vacancies will introduce more and more repulsive forces between cations, which in turn put the grains under

compressive stresses. These stresses are responsible for the increase of the fracture toughness at higher temperature, but at the same time they force a crack to move not across the grains, but choose easier path along the grain boundaries, causing the appearance of the intergranular failure mode.

The fracture surfaces of $Sc_{0.1}Ce_{0.01}ZrO_2$ Praxair ceramics after K_{Ic} tests performed at RT and 1000^{o}C are shown in Fig. 41. The porosity with a pore size of about 1.28 μm is present along almost all grain boundaries and inside the grains. The fracture mode is almost fully intergranular. As it was reported in [83], the Praxair ceramics has higher quantity of SiO_2, which affect the sinterability of the material to the full density. It is also possible that presence of SiO_2 is responsible for smaller formation of oxygen vacancies when temperature increases, thus there is no increase in fracture toughness at 800 – 1000^{o}C region, since $Sc_{0.1}Ce_{0.01}ZrO_2$ Praxair ceramics remain more stoichiometric upon heating.

Fracture origin of the rhombohedral $Sc_{0.1}Ce_{0.01}ZrO_2$ were typical defects, such as pores or cracks, which can be found in ceramics and which are introduced during machining or processing of the samples. An example of a typical fracture origin is shown in Fig. 42A. The fracture surface of rhombohedral phase after strength measurement at RT is shown in Fig. 42B. The relief of the fracture surface of the rhombohedral $Sc_{0.1}Ce_{0.01}ZrO_2$ is much more coarse and complex in comparison with smooth and flat fracture surface of cubic- $Sc_{0.1}Ce_{0.01}ZrO_2$, which indicates that there should be some barriers present for the propagating crack causing it to deviate. Similar fracture surface was observed after tests at 400^{o}C. The appearance of rough path for the propagating crack might be the reason why strength of the rhombohedral phase is higher

than strength of the cubic phase. However, this did not affect the K_{Ic} which remain quite low and was measured to be lower for rhombohedral in comparison with cubic DKKK ceramics.

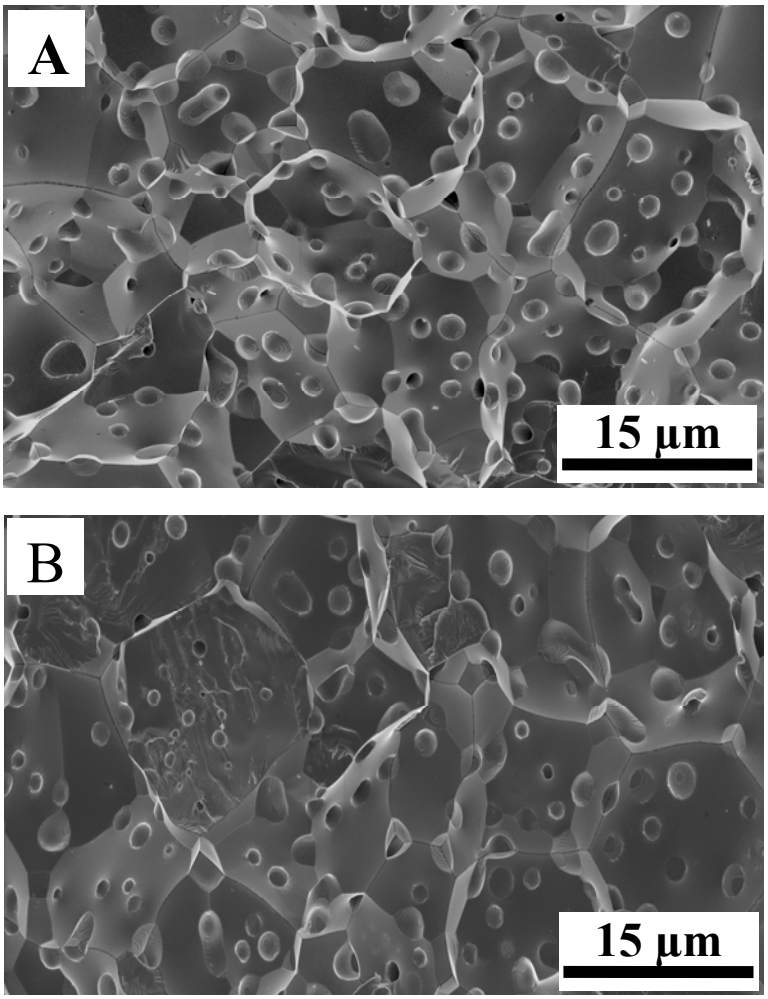

Figure 41: Fracture surface of Praxair $Sc_{0.1}Ce_{0.01}ZrO_2$ ceramics after K_{Ic} measurement at RT (A) and 1000°C (B).

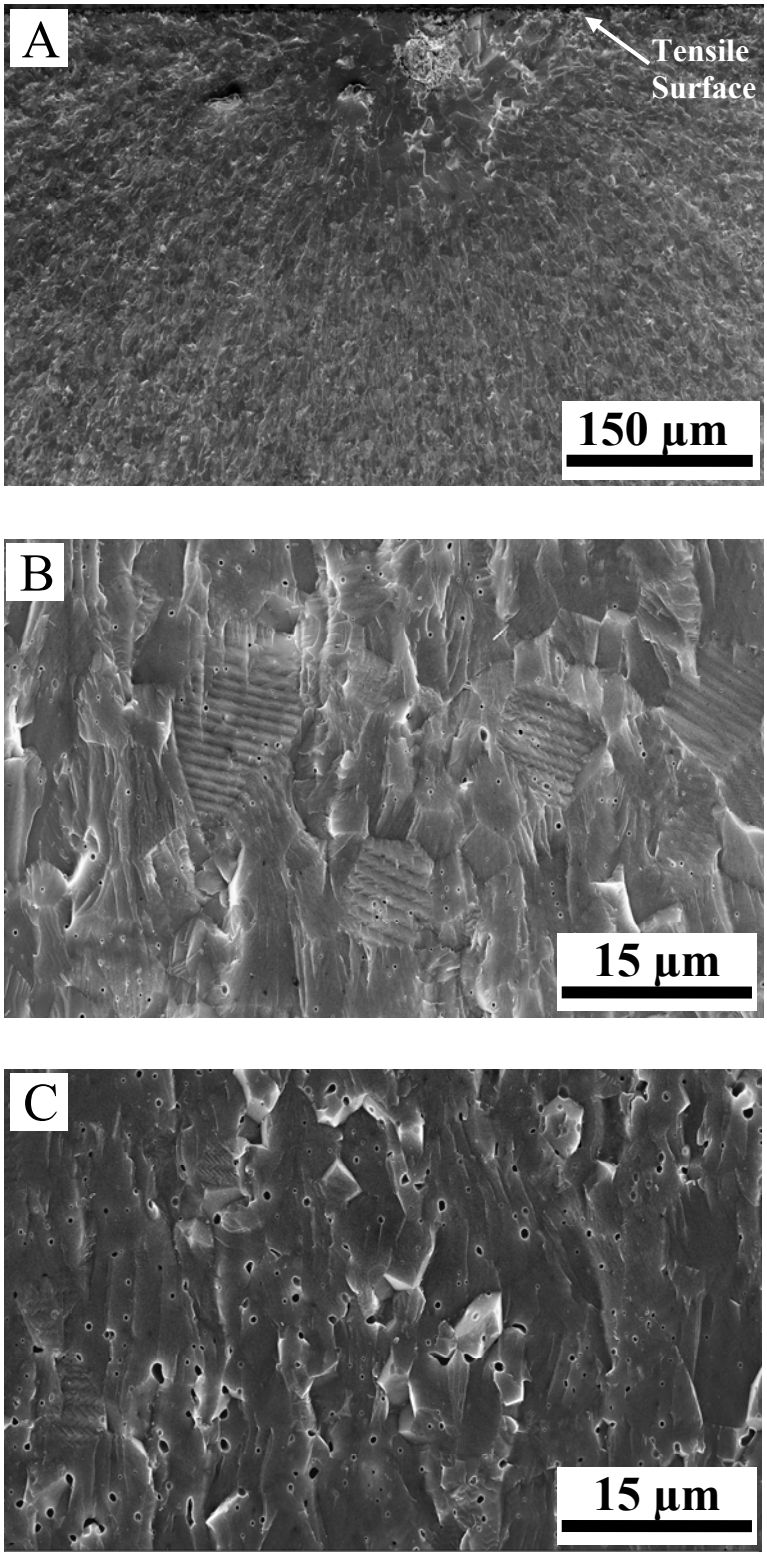

Figure 42: 16 (A) Fracture origin; (B) fracture surface after RT test; and (C) fracture surface after 400oC test of the of rhombohedral $Sc_{0.1}Ce_{0.01}ZrO_2$ ceramics

CHAPTER 5:
CONCLUSION AND FUTURE WORK

This chapter delivers the conclusion of the vibrational and mechanical properties of $Sc_{0.1}Ce_{0.01}ZrO_2$ electrolyte materials for intermediate temperature solid oxide fuel cells (SOFCs). Also, emphasis on the future work is declared here.

5.1 Conclusion

The effect of the temperature and stress on the stability of the cubic and rhombohedral $Sc_{0.1}Ce_{0.01}ZrO_2$ ceramics has been studied by micro – Raman spectroscopy. The whole spectral range of the cubic and rhombohedral $Sc_{0.1}Ce_{0.01}ZrO_2$ collected using 532 nm and 785 nm lasers has been reviewed. The bands located at 239, 480, and 623 cm^{-1} are detected by using two available lasers. However, most of the bands can only be seen by using either 532 nm or 785 nm lasers. Such bands can be tentatively assigned to the appearance of the luminescence peaks related to $Ln3^+$ impurity ions and further photoluminescence study is required to determine the nature of the impurities responsible for the appearance of the bands.

The phase stability of the cubic and rhombohedral phases has been studied by *in – situ* heating experiment. It was found that the cubic phase is stable upon heating up to 1000^oC using fast heating/cooling rates (10^oC/min) in the experiment. The rhombohedral $Sc_{0.1}Ce_{0.01}ZrO_2$ is stable upon heating in 25 – 400^oC temperature range. The cubic to rhombohedral phase transformation can be detected when cubic $Sc_{0.1}Ce_{0.01}ZrO_2$ was deformed by an indentation and then heated up to 400^oC. Upon cooling from 400^oC to room temperature, the cubic phase transformed to the rhombohedral phase if located near to the Vickers impression. Thus, it is not only the

temperature but also the introduced stress which were responsible for facilitating of the cubic to rhombohedral phase transition upon cooling. While it might be difficult to determine the stress distribution around the Vickers impressions in $Sc_{0.1}Ce_{0.01}ZrO_2$, due to complexity of the stress state a uniaxial compression experiments are required to determine the stress sensitivity and piezospectroscopic coefficients of the bands in cubic and rhombohedral phases. However, based on the present finding it is clear that both applied stress and heating of the material within a certain temperature range will promote a cubic to rhombohedral phase transition in $Sc_{0.1}Ce_{0.01}ZrO_2$.

The mapping experiments were performed to collect the preliminary data, such as a shift of the selected peaks, which can be further used to characterize stress states or detect any possible phase transition in the materials indented by Vickers. The stress related shift of peak positions has been detected both in cubic and rhombohedral $Sc_{0.1}Ce_{0.01}ZrO_2$ upon indentation. The peaks under investigation were shifted to the higher wavenumbers in the center of the Vickers impression in the cubic phase; however most of the investigated peaks of the rhombohedral $Sc_{0.1}Ce_{0.01}ZrO_2$ were shifted to the lower wavenumbers in the center of the impression. Further work is required to determine the origin of the bands and establish a dependence of their positions on the applied stress. However, even without quantification of the complex stress state around the impression one can say that in order to promote cubic to rhombohedral phase transition in $Sc_{0.1}Ce_{0.01}ZrO_2$ both temperature and applied stress are required.

The mechanical properties, such as hardness, indentation fracture resistance, Young's modulus, strength, and fracture toughness, of $Sc_{0.1}Ce_{0.01}ZrO_2$ have been measured. The ceramics were sintered from the powders produced by two manufactures – DKKK and Praxair. Both DKKK and Praxair ceramics were found to exist in the cubic structure upon cooling of the samples from sintering temperature, however it was found that DKKK cubic phase could be transformed to the rhombohedral phase by dwelling at 375 - 400^{o}C for 12 hours. Young's moduli of the cubic and rhombohedral phases of DKKK ceramics are reported to be 217.67 ± 0.61 GPa and 188.23 ± 2.81 GPa, respectively. The softening of both cubic DKKK and Praxair and rhomboheral DKKK phases has been observed when the temperature of the tests increased up to 500^{o}C, but stiffening of the cubic phases occurred when temperature was increased from 500^{o}C to 1000^{o}C. Hardness of the DKKK and Praxair ceramics increased as sintering temperature and density of the materials were increased, but fracture toughness remains almost the same, with some slight increase for the ceramics sintered at lower temperature which have higher amount of the porosity. No significant indentation size effect has been observed for cubic $Sc_{0.1}Ce_{0.01}ZrO_2$, but non significant decrease in ~ 2 GPa in hardness was detected in rhombohedral $Sc_{0.1}Ce_{0.01}ZrO_2$ when the indentation load was increased from 0.25 N to 50 N load. Four point bending strength of the cubic and rhombohedral DKKK ceramics is on the order of 200 – 230 MPa at room temperature. Strenght decreases to 150 – 170 MPa at higher temperatures for cubic phase, but increases to 270 MPa at 400^{o}C for the rhombohedral phase. The Praxair $Sc_{0.1}Ce_{0.01}ZrO_2$ exhibits the lower strength values in the range of 80 MPa at room temperature to 60 MPa at high temperatures. Fracture toughness measured in bending using V notched samples was also higher for DKKK $Sc_{0.1}Ce_{0.01}ZrO_2$ ceramics than for Praxair ceramics both at room and high

temperatures. The microstructural characterization revealed that Praxair ceramics has very inhomogeneous grain and porosity distribution where selected areas could have a significant amount of porosity while the majority of the grains still have intra-and intergranulated porosity. DKKK ceramics exhibited intergranular fracture for tests performed at room temperature, but at high temperature the mixed fracture occur and both intergranular and transgranular fracture modes could be found. The rhombohedral $Sc_{0.1}Ce_{0.01}ZrO_2$ ceramics exhibit the complex relief on the fracture surface with the surface structure that required special detailed studies. The compression of the cubic and rhombohedral phases revealed that both phases behave in the elastic way and no hysteresis is observed upon loading / unloading.

5.2 Future work

Recommendation for future work:

- Further photoluminescence study is required to determine the nature of the impurities responsible for the appearance of the bands.
- Determination of the origin of the bands and establish a dependence of their positions on the applied stress.
- The rhombohedral $Sc_{0.1}Ce_{0.01}ZrO_2$ ceramics exhibit the complex relief on the fracture surface with the surface structure that required special detailed studies.
- The further calibration experiments are required to quantify the stresses induced in the cubic and rhombohedral $Sc_{0.1}Ce_{0.01}ZrO_2$ during the indentation.

APENDIX:
SHORT BIOGRAPHY

Svetlana Lukich was born in Bosnia, former Yugoslavia and emigrated to the United States of America in month of August 2000. In 2004 she attained Associate Degree in General Education at Seminole Community College, Sanford, Florida. In spring 2005 she arrived at University of Central Florida as an engineering student. By the end of 2007 Svetlana graduated from University of Central Florida with an undergraduate degree in Mechanical Engineering-Mechanical System Options. She is a candidate for the Master of Science degree in Material Science and Engineering at University of Central Florida. Svetlana has done research on electrolyte materials for Solid Oxide fuel Cells (SOFCs).

LIST OF REFERENCES

[1] Stöver, D. (2004). Processing and properties of the ceramic conductive multilayer device solid oxide fuel cell (SOFC). *Ceramics International*, 30, 1107-1113.

[2] Singh, P., Minh, N.Q. (2004). Solid Oxide Fuel Cells: Technology Status. *International Journal of Applied Ceramic Technology*, 1 (1), 5–15.

[3] Basu, R. N. (2007). Materials for Solid Oxide Fuel cells. In S. Basu (Ed.) Recent Trends in Fuel Cell Science and Technology (pp. 286-331). New Delhi, India: Anamaya.

[4] Haile, S. M. (2003). Fuel cell materials and components. A*cta Materialia*, 51, 5981-6000.

[5] O'Hayre, R., Cha, S-W, Colella, W, Prinz, F..B. (2006). Fuel cell types. In Fuel Cell Fundamentals, Chapter 1 (pp.10). New York, John Wiley & Sons.

[6] EG & G Technical Service, Inc. (2004). Fuel Cell Types. In Fuel Cell Handbook (pp.26-27). West Virginia: U.S. Department of Energy Press.

[7] Singhal, S. C. (2000). Advances in solid oxide fuel cells. *Solid State Ionics*, 135, 305-313.

[8] Yamamoto, O. (2000). Solid oxide fuel cells: fundamental aspects and prospects. *Elecrtochimica Acta*, 45 (15-16), 2423-2435.

[9] Steele, B. C. H. (2001). Material science and engineering: The enabling technology for the commercialization of fuel cell systems. *Journal of Materials Science*, 36, 1053-1068.

[10] Anderson, H. U., & Tietz, F. (2003). Interconnects, Charter 7. In S. C. Singhal & K. Kandall (Ed.), Interconects. High Temperature Solid Oxide Fuel Cells:Fundamentals design and Applications (pp. 173-195). UK: Elsevier.

[11] Gauckler, L. J., Beckel, D., Buergler B. E., Jud E., Mueche U. P., Prestat M., Rupp J. L. M., Richter J. (2004). Solid Oxide Fuel Cells: Systems and Materials. *Chima*, 58, 837.

[12] Steele, B. C. H., (1992). Oxygen Ion Conductors and Their Technological Applications. *Materials Science and Engineering*, B13, 79-87.

[13] Mench, M. M., (2008). Solid Oxide Fuel Cells: Operation and Configuration. In Fuel Cell Engines (pp. 381-382). New Jersey: John Wiley & Sons, Inc., Hoboken.

[14] Rayment C., Sherwin S. (2003). Solid Oxide Fuel Cells: Configurations. In Introduction to Fuel Cell Technology (pp. 70-72). Indiana: University of Norte Dame Press.

[15] Barclay, F. J. (2007). Siemens Westinghouse. In Fuel cells, Engines and Hydrogen: an Energy Approach (pp. 75-76). England: John Wiley & Sons Ltd.

[16] Allen J., Doyon J. (1996). Carbonate Fuel Cell monolith design for high power density and low cost. Fuel Cells '96 Conference. Morgantown, West Virginia.

[17] Lilner, J.A. (2000). Fast Oxygen Transport in Acceptor Doped Oxides. *Solid State Ionics*, 129 (1-4), 13-23.

[18] Steel, B. C. H. (1989). Experimental Techniques. In T. Takahashi (Ed.) High Conductivity Solid Ionic Conductors: Recent Trends and Applications (pp402-446). Singapore: World Scientific.

[19] Ogaji, S. T. O., Singh, R., Pilidis, P., Diacakis, M. (2005). Modeling fuel cell performance using intelligence. *Journal of Power Sources*, 154, 192-197.

[20] Kharton, V. V., Marques, F. M. B., Atkinson, A. (2004) Transport properties of solid oxide electrolyte ceramics: a brief review. *Solid State Ionics*, 174, 135-149.

[21] Yarmolenko, S., Sankar, J., Bernier, N., Klimov, M., Kapat, J., Orlovskaya, N. (2009). Phase stability and Sintering Behavior of 10 mol % Sc_2O_3-1 mol % CeO_2-ZrO_2 Ceramics. *Journal of Fuel Cell Science and Technology*, 6, 021007-1.

[22] Subbarao, E. C. (1981). Zirconia- an overview. *Science and Technology of Zirconia*, 3, 1-23.

[23] Strubican, V. S., Hink, R. C., Ray, S. P. (1978). Phase Equilibria and Ordering in the System ZrO_2–Y_2O_3. *Journal of Aamerican Ceramic Society*, 61 (1-2), 17-21.

[24] Boivin, J. C., Mairesse, G. (1998) Recent Material Developments in Fast Oxide ion Conductors. *Chemistry of Materials*, 10, 2870-2888.

[25] Takahashi, T. (1972). Physics of Electrolytes, Vol. 2 (pp. 980-1049). London: Academic Press.

[26] Politova, T. I, Irvine, J. T. S. (2004). Investigation of scandia-yttria-zirconia system as an electrolyte material for intermidiate temperature fuel cells: influence of yttria content in system $(Y2O3)_x(Sc2O3)_{(11-x)}(ZrO2)_{89}$. *Solid State Ionics*, 168 (1-2), 153-165.

[27] De Ridder, M., Van Weizenis, R. G., Brongersma, H. H., Kreissing, U. (2003). Oxygen exchange and diffusion in the near surface of pure and modified yttria-stabilized zirconia, *Solid Stat Ionics*, 158 (1-2), 67-77.

[28] Badwal, S. P. S., Ciacchi, F. T., Rajendran, S., Drennan, J. (1998). An investigation of conductivity, microstructure and stability of electrolyte compositions in the system 9 mol% (Sc2O4-Y2O3)-ZrO2(Al2O3). *Solid State Ionics,* 109 (1-3), 167-186.

[29] Butler, V., Catlow, C. R. A., Fender, B. E. E. (1981). The defect structure of anion deficient ZrO2. *Solid State Ionic*, 5, 539-542.

[30] Hearing, C., Roosen, A., Schichl, H., Schnöller, M. (2005). Degradation of the electrical conductivity in stabilized zirconia system Part II: Scandia-stabilized zirconia. *Solid State Ionics*, 176, 261-268.

[31] Ruh, R., Gerrett, H. J., Domagala, R. F., Patel, V. A. (1997). The system zirconia-scandia. *Journal of American Ceramic Societi,* 60 (9-10), 399-403.

[32] Chiba, R., Yoshimura, F., Yamaki, J., Ishii, T., Yonshimura, T, Endou, K. (1997). Ionic conductivity and morphology in Sc_2O_3 and al_2O_3 doped ZrO_2 films prepared by the sol-gel method. *Solid State Ionics*, 104, 259-266.

[33] Nomura, K., Mizutani, Y., Kawai, M., Nakamura, Y.,Yamamoto, O. (2000). Aging and Raman scattering study of scandia and yttria doped zirconia. *Solid State Ionics*, 132, 235

[34] Yamamoto, O., Arati, Y., Takeda, Y., Imanishi, N., Mizutani, Y., Kawai, M., Nakamura, Y. (1995). Electrical conductivity of stabilized zirconia with ytterbia and scandia. *Solid State Ionics*. 79, 137.

[35] Arachi, Y., Asai, T., Yamamoto, O., Takeda, Y., Imanishi, N., Kawate, K., Tamakoshi, C. (2001). Electrical Conductivity of ZrO_2-Sc_2O_3 Doped with HfO_2, CeO_2, and Ga_2O_3. *Journal of Electrochemical Science*, 148 (5), A520-A523.

[36] Yashima, M., Kakihana, M., Yoshimura, M. (1996). Metastable-stable phase diagrams in the zirconia-containing systems utilized in solid oxide fuell cell application. *Solid State Ionic*s, 86-88, 1131-1149.

[37] Lee, D.-S., Kim, W. S., Choi, S. H., Kim, J., Lee, H.-W., Lee, J.-H. (2005). Characterization of ZrO_2 co-doped with Sc_2O_3 and CeO_2 electrolyte for the application of intermediate temperature SOFCs. *Solid State Ionics*, 176, 33-39.

[38] Samuel, V., Gaikwad, A. B., Ravi, V. (2006). A coprecipitation technique to prepare $NaNbO_3$ and $NaTaO_3$. *Bulletin of Material Science*, 29 (2), 123-125.

[39] Dhage, S. R., Ravi, V., Date, S. K. (2003). Preparation of microwave dielectric, $Sn_{0.2}Zr_{0.8}TiO_4$. *Bulletin of Mateial Sciience*, 26, 215.

[40] Gaikwad, S. P., Dhesphande, S. B., Khollam, Y. B., Samuel, V., Ravi V. (2004). Coprecipitation method for the preparation of nonocrystalline ferroelectric $CaBi_2Ta_2O_9$. *Materials Letters*, 58 (27-28), 3474-3476.

[41] Rocha, R. A., Muccillo, E. N. S., Djurado, E, Muccillo, R. (2009). An experimental setup to synthesiz ceramic nanoparticles by the spray pyrolysis technique for electrolyte in solid oxide fuel cells. 11th International Conference on Advanced Materials. Brazil.

[42] Djurado, E., Meunier, E. (1998). Synthesis of Doped and Undoped Nanopowders of Tetragonal Polycrystalline Zirconia (TPZ) by Spray-Pyrolysis. (1998). *Journal of Solid State Chemistry*, 141, 191-198.

[43] Janackovic, D. J, Jokanovic, V., Kostic-Gvozdenovic, L. J., Zec, S., Uskokovic, D. (1997). Syntheses and formation mechanism of submicrometre spherical cordierite powders by ultrasonic spray pyrolysis. *Journal of Materials Science*, 22, 163-168.

[44] Takeuchi, T., Kondoh, I., Tamari, N., Balakrishnan, N., Nomura, K., Kageyama, H., Takeda, Y. (2002). Improvement of mechanical strength of 8 mol % yttria-stabilized zirconia ceramics by spark-plazma sintering. *Journal of Electrochemical Society*, 149 (4), A455-A461.

[45] Gibson, I. R., Dransfield, G. P., Irvine, J. T. (1998). Influence of Yttria Concentration upon Electrical Properties and Susceptibility to Ageing of Yttria-stabilized Zirconia. *Journal of European Ceramic Society*, 18, 661-667.

[46] Ze, Z., Zhu, Q. (2005). Low temperature processing of dense nanocrystalline Scandia-doped zirconia (ScSZ) ceramics. *Solid State Ionics*, 176, 2791-2797.

[47] Kosacki, I., Anderson, H. U., Mizutani, Y., Ukai, K. (2002). Nonstoichiometry and electrical transport in Sc-doped zirconia." *Solid State Ionics*, 152-153, 432-438.

[48] Kharton, V. V., Marques, F. M. B., Atkinson, A. (2003). Transport properties of solid oxide electrolyte ceramics: a brief review. *Solid State Ionics*, 174, 135-149.

[49] Arachi, Y., Sakai, Y. M., Yamamoto, Y., Takeda, Y., Imaniski, N. (1999). Electrical conductivity of the ZrO_2-Ln_2O_3 (Ln=lanthanides) system. *Solid State Ionics*, 121, 133 – 139.

[50] Yananura, H., Utsunomiya, N., Mori, T., Ataka, T. (1998). Electrical conductivity in the ZrO_2-Y_2O_3-Sc_2O_3." *Solid State Ionics*, 107, 185-189.

[51] Yashima, M., Kakihana, M, Yoshimura, M. (1996). Metastable-stable phase diagrams in zirconia-containing systems utilized in sold-oxide fuel cell application. *Solid State Ionics*, 86-88, 1131-1149.

[52] Fuijimori, H., Yashima, M., Kakihana, M., Yoshimura, M. (2002). β-cubic phase transition of Scandia-doped zirconia solid solution: Calorimetry, x-ray diffraction, and Raman scattering. *Journal of Applied Physics*, 91, 6493-6498.

[53] Wang, Z., Chang, N., Bi, Z., Dong, Y., Zhang, H., Zhang, J., Feng, Z., Li, C. (2005). Structure and Impedance Behavior of 10mol% Sc_2O_3-1mol% CeO_2-ZrO_2 Ceramics. *Journal of Materials Letters*, 59, 2579-2582.

[54] Hirano, M., Watanabe, S., Kato, E., Mizutani, Y., Kawai, M., Nakamura, Y. (1998). Fabrication, electrical conductivity and mechanical properties of Sc_2O_3-doped tetragonal zirkonia ceramics. *Solid State Ionics*, 111, 161-169.

[55] Mizutani, Y., Tamura, M., Kawai, M, Yamamoto, O. (1994). Development of high-performance electrolyte in SOFC. *Solid State Ionics*, 72, 271-275.

[56] Zevalkink, A., Hunter, A., Swanson, M., Johnson, C., Kapat, J., Orlovskaya, N. (2007). Processing and Characterization of Sc_2O_3-CeO_2-ZtO_2Electrolyte Based Intermediate Tempertaure Solid Oxide Fuel Cells. *Materials Research Society*: Symposium Proceedings. 972, AA03-04.

[57] Lukich, S., Carpenter, C., Orlovskaya, N. (2009). Assessment of Temperature and Pressure Assisted Cubic to Rhombohedral Phase Transition in $Sc_{0.1}Ce_{0.01}ZrO_2$ by micro-Raman. *Proceidings of the 33th International Conference on Advanced Ceramic and Composites*. Daytona Beach, Florida: WILEY. 4-14.

[58] Orlovskaya, N., Lukich, S., Subhash, G.,., Graule, T., Kuebler, J. (2009). Mechanical Properies of $Sc_{0.1}Ce_{0.01}ZrO_2$ Electrolyte Ceramics. submitted to *Journal of Power sources.*

[59] ASM International. (2004). Microelectronics Failure Analysis. Ohio: ASM International the Material Information society.

[60] Perez, N. (2004). Indentation-Induced Cracking: Chapter 10. In Fracture Mechanics (pp. 244-248). New York: Kluwer Academics.

[61] Dieter, G. E. (1988). Vickers Hardness: Chapter 11. In D. Bacon (Ed.), Mechanical Metallurgy (pp. 331-332). London, UK: Mc-Graw-Hill Brook Company.

[62] Anstis, G. R., Chantikul, P., Lawn, B.R., Marshall, D. B. (1981). A Critical Evolution of Indentation Techniques for Measuring Fracture Toughness: I, Direct Crack Measurements. *Journal of American Ceramic Society*, 64 (9), 533-538.

[63] Morris, D. J., Cook, R. K. (2004). *In Situ* Cube-Corrner Indentation of Soda-Lime Glass and Fused Silica. *Journal of American Ceramic Society*, 87 (8), 1494-1501.

[64] E 1876-99 ASTM "Standard Test Method for Dynamic Young's Modulus, Shear Modulus, and Poisson's Ratio by Impulse Excitation of Vibration".

[65] Kübler J. (1999). Fracture Toughness of Ceramics using the SEVNB Method: First Results of a Joint VAMAS / ESIS Round Robin. *Ceramic Engineering and Science Proceedings*, 20, 495-502.

[66] Otake, T., Yugami, H., Naito, H., Kawanmra, K., Kawada, T., Mizusaki, J. (2000). Ce^{3+} concentration in ZrO_2-CeO_2-Y_2O_3 system studied by electronic Raman scattering. *Solid State Ionics*, 135, 663-667.

[67] Orera, V. M., Merino, R. I., Pena F. (1994). $Ce^{3+} \leftrightarrow Ce^{4+}$ conversion in ceria-doped zirconia single crystals induced by oxido-reduction treatments. *Solid State Ionics*, 72, 224-231.

[68] Kaspar, J., Fornasiero, P., Baldueci, G., Di Monte, R., Hickey, N., Sergo, V. (2003). Effect of ZrO2 content on textual and structural properties of CeO_2-ZrO_2 solid solutions made by citrate complexation route. *Inorganica Chimica Acta*, 349, 217-226.

[69] Maczka, N., Lutz, E. T. G., Verbuk, H. J., Oskam, K., Meijerink, A., Hanuza, J., Stuivinga, N. (1999). Spectroscopic studies of dynamically compacted monolitic ZrO_2. *Journal of Physics and Chemistry of Solids*, 60, 1909-1914.

[70] Asher, I. N., Papanicolaou, B., Anastassakis E. (1976). Laser excited lumencence spectra of zirconia. *Journal of Physics and Chemistry of Solids*, 37, 221-225.

[71] Fornasicro, P., Spghini, A., Di Monte, R., Bettinelli, M., Kaspar, J., Bigotto, A., Sergo, V., Graziani, M. (2004). Laser-Excited Luminescence of Trvalent Lanthanaide Impurities and Local Structure in CeO_2-ZrO_2 Mixed oxides. *Chemistry of Materials*. 16, 1938 – 1944.

[72] Kishimoto, H., Sakai, N., Horita, T., Yamaji, K., Xiong, Y. P., Brito, M. E., Yokokawa, H. (2008). Rapid Phase Transformation of Zirconia, in the Ni-SeS Z Current Anode under Reducing Condition. *Solid State Ionics*, 179, 2037-2041.

[73] Vlaic, G. G., Di Monte, R, Fornasiero, P, Fonda, E., Kaspar, J., Graziani, M. (1999). Redox property-local structure relationship in the Rh-loaded CeO_2-ZrO_2 mixed oxides. *Journal of Catalysis*. 182, 378-389.

[74] Yashima M., Arashi H., Kakihana N., Yoshimura M. (1994). Raman scattering study of cubic-tetragonal phase transition in $Zr_{1-x}Ce_xO_2$ solid solution. *Journal of American Ceramic Society*. 77, 1067-1071.

[75] Philippi, C. M., Mazgiyasni, K. S. (1971). Infrared and Raman spectra of zirconia polymorphs. *Journal of American Ceramic Society*, 54, 254-258.

[76] Feinberg, A., Perry, C. H. (1981). Structural disorder and phase transitions in ZrO_2-Y_2O_3 system. *Journal of Physics and Chemistry of Solids*, 42, 513-518.

[77] Kosacki,.I., Petrovsky, V., Anderson, H., Colomban, P. (2002). Raman Spectroscopy of Nanocrystalline Ceria and Zirconia Tin Films. *Journal of American Ceramic Society*, 85, 2646-2650.

[78] Limarga, A., Clarke, D., (2007). Piezo-spectroscopic coefficient of tetragonal-prime yttria-stabilized zirconia. *Journal of American Ceramic Society*, 90, 1272 – 1275.

[79] Wallis, R. F., Maradudin, A. A. (1962). Lattice anharmonicity and optical absorption in polar crystals. III. Quantum mechanical treatment in the linear approximation. *Physical. Review Letters*, 125, 1277-1282.

[80] Raghavan, S., Imbrie, P. K., Crossley, W. (2008). Spectral analysis of R lines and vibronic sidebands in the emission spectrum of ruby using genetic algorithms. *Applied Spectroscopy*. 62, 765-765.

[81] Raghavan, S., Imbrie, P. K. (2009). Ex-situ stress measurements in polycrystalline ceramics using photo-stimulated luminescence spectroscopy and high-energy x-rays. *Journal of American Ceramic Society*, 92, 1567-1573.

[82] Chiba, R., Ishii, T., Yoshimura, F. (1996). Temperature dependence of ionic conductivity in $(1-x)ZrO_2$-$(x-y)Sc_2O_3$-yYb_2O_3 electrolyte material. *Solid State Ionics*, 91 (3-4), 249-256.

[83] Barsoum, M. B. (2003). Diffusion and Electrical Conductivity. In Fundamentals of Ceramics (pp. 188). New York: Taylor & Francis Group.

[84] Wachtmann, J. B. (1963). Mechanical and Electrical Relaxation in ThO_2 Containing CaO. *Physical. Review Letters*, B131 (2), 517-527.

[85] Taneja, M., Radovic, M., Orlovskaya, N. (2009). Thermal expansion and elastic moduli of electrolyte materials for high and intermediate temperature Solid Oxide Fuel Cells. submitted to *Solid State Ionics*.

[86] Weller, M. (2001). Mechanical Spectroscopy Q^{-1} with application to materials science (pp. 95-137). Switzerland: Trans Tech Publications.

[87] Weller, M. (1994). Mechanical loss measurements on yttria-and calcia-stabilized zirconia. *Journal of Alloys and Compounds*, 211/212, 66.

[88] Weller, M., Damson, B., Lakki, A. (2000). Mechanical loss of cubic zirconia. *Journal of Alloys and Compounds*. 310, 47-53.